

# INNOVATIVE EXPERIMENTAL CONCEPTS FOR OPTICAL COHERENCE TOMOGRAPHY

THÈSE N° 2954 (2004)

PRÉSENTÉE À LA FACULTÉ SCIENCES ET TECHNIQUES DE L'INGÉNIEUR

Institut d'imagerie et optique appliquée

SECTION DE MICROTECHNIQUE

ÉCOLE POLYTECHNIQUE FÉDÉRALE DE LAUSANNE

POUR L'OBTENTION DU GRADE DE DOCTEUR ÈS SCIENCES

PAR

**Markus LAUBSCHER**

Diplom-Physiker, Universität Karlsruhe, Allemagne  
ingénieur physicien diplômé de l'ENSP Grenoble, France  
et de nationalité allemande

acceptée sur proposition du jury:

Prof. T. Lasser, directeur de thèse  
Prof. A.F. Fercher, rapporteur  
Prof. P. Jacquot, rapporteur  
Dr A.G.H. Podoleanu, rapporteur  
Prof. R.P. Salathé, rapporteur

Lausanne, EPFL  
2004



# Abstract

Optical Coherence Tomography (OCT) is a recent biomedical imaging technique based on low-coherence interferometry that is capable of acquiring depth-resolved reflectivity maps of scattering tissues with high sensitivity. The conventionally employed imaging mode is to build up a cross sectional image by scanning the sample surface with a point illumination. In order to increase imaging speed, the concept of parallel detection has been introduced to OCT. Here, a whole sample line or even surface is imaged directly onto an array of photodetectors, making the lateral scanning motion obsolete. A customized detector array has been developed in our institute for parallel OCT imaging based on complimentary metal-oxide-semiconductor (CMOS) technology. It associates a signal processing circuit to each photo-sensitive area of the array, capable of demodulating the interferometric signal on-chip. In this manner, only the signal envelop has to be read out, allowing for a high dynamic range and high frame rates.

At the beginning of the thesis, this device had only been tested for topographic measurements on reflective surfaces. As a direct continuation of this previous work, the initial objective of this thesis has been to extend its application to parallel OCT in scattering samples and to identify other uses of this technology in the field of OCT. Accordingly, the first part of this work is dedicated to parallel detection in OCT, using this customized CMOS detector array. The feasibility of the approach is shown experimentally on scattering samples. Reflective surfaces covered with scattering solutions of varying concentration and onion samples are studied. Furthermore, the initial goal of fast OCT imaging is pursued by using the detector at its technological limits and realizing video-rate, three-dimensional OCT acquisitions of a dynamically changing sample. The thermal deformations induced by the probing beam on a dark strand of human hair are imaged at 25 volume acquisitions per second.

Identified as a possible new application for the CMOS detector array, the concept of wavelength de-multiplexing for spectroscopic OCT is investigated in the second part of this thesis. Wavelength de-multiplexing is an experimental method for realizing spectroscopically resolved, time-domain OCT measurements. In contrast to the currently employed numerical post-processing methods for extracting spectroscopic information, wavelength de-multiplexing relies on optical wavelength separation in the interferometer detection arm and acquisition of independent wavelength channels using a detector array. The method itself is first studied using a laterally translated photodiode for detection, in order to compare it to the conventional spectroscopic OCT approach. The absorption characteristics of a glass filter and a Nd-doped crystal are measured in this manner. Then, associated to the CMOS detector array in a proof-of-principle experiment, the dynamically changing, spatially resolved absorption of a dye mixing process is measured online.

The experimental setup used for wavelength de-multiplexing has lead to an innovative technique that is of interest to low coherence interferometry in general. The axial depth scan employed in all time-domain low coherence interferometry setups should ideally introduce a linear change with time of optical path difference between the interferometer's sample and reference arms. However, depending on the scan method used, the path difference variation is only approximatively linear and can even vary randomly from scan to scan. For precise, phase-sensitive and repetitive measurements the scans have to be calibrated. By increasing the coherence length of part of the detected radiation in the detection

arm of the interferometer through narrow spectral filtering, a calibration signal is created that permits the precise measurement of the optical path difference variation and thus its calibration without the need for a secondary interferometer. The usefulness of the approach is demonstrated by combining it with a recently published spectral shaping technique for sidelobe suppression in OCT when using non-Gaussian source spectra. In order to be beneficial, such a technique requires highly repetitive measurements that can only be obtained with particularly stable scanning devices or well calibrated ones.

In summary, this thesis studies three innovative experimental concepts that aim to improve OCT imaging speed and imaging quality and proposes them as interesting new tools to the OCT community.

# Résumé

La Tomographie par Cohérence Optique (OCT) est une méthode d'imagerie biomédicale récente qui est basée sur l'interférométrie à basse cohérence. Elle permet de localiser et de mesurer les discontinuités de l'indice de réfraction à l'intérieur de tissus diffusants. Le mode d'imagerie couramment employé consiste à construire une image tomographique en balayant la surface de l'échantillon avec une illumination ponctuelle. Afin d'augmenter la vitesse d'acquisition des images, la méthode de la détection parallèle a été introduite en OCT. Cette dernière permet de former l'image de toute une ligne ou même d'une surface de l'échantillon directement sur une matrice de photodétecteurs, ce qui rend le balayage latéral inutile. Un tel capteur spécialisé fut développé dans notre institut pour la détection parallèle en OCT, basé sur la technologie CMOS. Il associe un circuit électronique de traitement de signal à chaque photodiode de la matrice pour réaliser une démodulation du signal interférométrique directement sur le capteur. De cette manière, seule l'enveloppe du signal est détectée, permettant d'obtenir une dynamique importante et une lecture d'images rapide.

Au commencement du présent travail, ce capteur n'avait été testé que pour la mesure topographique de surfaces réfléchissantes. Cette thèse, étant la continuation directe du travail antérieur, avait comme objectif initial d'étendre son champ d'application aux milieux diffusants et d'identifier d'autres utilisations possibles d'une telle technologie dans le domaine de l'OCT. Par conséquent, une première partie de cette recherche est consacrée à la détection parallèle en OCT avec ce capteur spécialisé CMOS. La faisabilité d'une telle approche est démontrée expérimentalement dans des milieux diffusants. Nous avons étudié des images de surfaces réfléchissantes derrière des solutions diffusantes de différentes concentrations et des images d'oignons. De plus, le but initial d'imagerie OCT à haute vitesse a été poursuivi en utilisant le capteur à sa limite de performance pour réaliser des mesures tri-dimensionnelles d'un échantillon dynamique à vitesse vidéo. La déformation induite par le faisceau lumineux sur un cheveu humain a été imagée à 25 acquisitions de volume par seconde.

La méthode du dé-multiplexage en longueur d'onde est identifiée comme une nouvelle application possible du capteur CMOS pour réaliser de l'OCT fonctionnelle. Cette approche expérimentale qui permet de réaliser des mesures spectroscopiquement résolues en OCT est étudiée dans une deuxième partie de la thèse. Contrairement aux méthodes actuellement utilisées qui se basent sur un traitement numérique du signal OCT conventionnel après la mesure, le dé-multiplexage en longueur d'onde s'appuie sur la séparation expérimentale de la lumière en canaux spectraux indépendants dans le bras de détection de l'interféromètre ainsi que sur leur détection parallèle sur une matrice de photodétecteurs. Afin d'étudier la méthode elle-même ainsi que pour la comparer à l'approche conventionnelle, nous utilisons d'abord une simple photodiode qui est latéralement déplacée pour la mesure séquentielle des canaux spectraux à la place du détecteur parallèle. Les caractéristiques d'absorption d'un filtre en verre et d'un cristal dopé Nd sont obtenues de cette manière. Ensuite, l'utilisation du capteur CMOS permet de mesurer un phénomène dynamique d'absorption, le processus de mélange d'un colorant absorbant dans une solution transparente.

Le dispositif expérimental utilisé pour le dé-multiplexage en longueur d'onde nous a amené à proposer une technique innovante - d'intérêt général pour l'interférométrie à basse cohérence. Le balayage

axial employé dans tous les dispositifs d'interférométrie à basse cohérence dans le domaine temporel devrait idéalement introduire un changement linéaire de la différence de chemin optique entre les bras de référence et d'échantillon de l'interféromètre. Cependant, selon la méthode de balayage utilisée, la variation du chemin optique n'est qu'approximativement linéaire et peut même changer de façon aléatoire d'un balayage à l'autre. Afin de réaliser des mesures précises et reproductibles, le balayage doit être calibré en continu. Un signal de calibration de haute cohérence peut être généré par un filtrage spectral fin d'une partie de la lumière détectée dans le bras de détection de l'interféromètre. Il permet la mesure précise de la variation du chemin optique et donc sa calibration, sans avoir recours à un interféromètre secondaire. L'approche est démontrée en la combinant avec une technique récemment publiée qui permet d'atténuer le bruit cohérent généré par des sources lumineuses de spectre non-Gaussien en introduisant une correction numérique du spectre. Une telle méthode dépend fortement de la reproductibilité des mesures, ce qui requiert des moyens de balayage particulièrement stables ou bien calibrés.

En résumé, cette thèse étudie trois approches expérimentales innovantes qui cherchent à améliorer la vitesse et la qualité en imagerie OCT. Elle propose ces nouveaux outils à la communauté OCT.

# Contents

<b>Abstract</b>	<b>i</b>
<b>Résumé</b>	<b>iii</b>
<b>Contents</b>	<b>v</b>
<b>List of Figures</b>	<b>vii</b>
<b>Acknowledgements</b>	<b>ix</b>
<b>Introduction</b>	<b>xi</b>
<b>1 OCT: history, principle and current research</b>	<b>1</b>
1.1 OCT: evolution of a new imaging technique . . . . .	1
1.1.1 Widespread medical imaging techniques . . . . .	1
1.1.2 OCT as new medical imaging technique . . . . .	2
1.2 Major current research topics in OCT . . . . .	4
1.2.1 Medical research . . . . .	4
1.2.2 Improvement of imaging performance . . . . .	4
1.2.3 New imaging modes: Functional OCT . . . . .	5
1.3 References . . . . .	7
<b>2 Parallel detection</b>	<b>13</b>
2.1 Concept of and approaches to parallel OCT . . . . .	13
2.1.1 Parallel detection: advantages and disadvantages . . . . .	13
2.1.2 CCD-based approaches to parallel detection . . . . .	15
2.1.3 CMOS-based approach to parallel detection . . . . .	16
2.2 Smart pixel detector array . . . . .	18
2.2.1 Working principle and characteristics . . . . .	18
2.2.2 Current SPDA applications . . . . .	19
2.3 Parallel OCT in scattering samples . . . . .	22
2.3.1 Introduction . . . . .	22
2.3.2 Method . . . . .	22
2.3.3 Results and discussion . . . . .	24
2.3.4 Conclusion and outlook . . . . .	28
2.4 Video-rate three-dimensional OCT . . . . .	29
2.4.1 Introduction . . . . .	29
2.4.2 Method . . . . .	30
2.4.3 Results . . . . .	31

2.4.4	Conclusion . . . . .	34
2.5	Conclusion . . . . .	36
2.6	References . . . . .	37
<b>3</b>	<b>Wavelength de-multiplexing</b>	<b>41</b>
3.1	Methods for spectroscopic OCT . . . . .	41
3.1.1	Joint time-frequency analysis . . . . .	41
3.1.2	Multiple source approach . . . . .	44
3.1.3	Wavelength de-multiplexing . . . . .	44
3.2	Comparison of JTFA and wavelength de-multiplexing . . . . .	48
3.2.1	General considerations . . . . .	48
3.2.2	Experimental comparison . . . . .	50
3.3	SOCT based on wavelength de-multiplexing and SPDA detection . . . . .	55
3.3.1	Introduction . . . . .	55
3.3.2	Method and optical setup . . . . .	55
3.3.3	Measurements . . . . .	57
3.3.4	Discussion . . . . .	58
3.3.5	Conclusion . . . . .	61
3.4	Possible extension: multi-resolution spectroscopic OCT . . . . .	63
3.5	Conclusion . . . . .	64
3.6	References . . . . .	65
<b>4</b>	<b>Depth scan calibration</b>	<b>67</b>
4.1	The need for scan calibration . . . . .	67
4.2	Double interferometer calibration method . . . . .	70
4.3	Self-referenced scan calibration method . . . . .	73
4.4	Details on calibration and spectral shaping algorithms . . . . .	78
4.4.1	Calibration algorithm . . . . .	78
4.4.2	Spectral shaping algorithm . . . . .	80
4.4.3	Phase correction and dispersion correction . . . . .	81
4.5	Possible extensions of the self-referenced calibration method . . . . .	84
4.5.1	Fiber-based implementation . . . . .	84
4.5.2	Optical amplification of calibration channel . . . . .	84
4.5.3	Real-time implementation . . . . .	85
4.6	Conclusion . . . . .	87
4.7	References . . . . .	88
	<b>Conclusion</b>	<b>89</b>
	<b>Curriculum Vitae</b>	<b>91</b>



# List of Figures

2.1	SPDA pixel functionality . . . . .	18
2.2	SPDA sequential readout principle . . . . .	19
2.3	Pictures of SPDA . . . . .	20
2.4	Optical setup schematic parallel OCT . . . . .	23
2.5	Schematic of reflective sample behind scattering solution . . . . .	24
2.6	Parallel OCT images of USAF . . . . .	26
2.7	Signal to noise ratio as function of optical depth in parallel OCT experiment . . . . .	26
2.8	Parallel OCT image of onion . . . . .	28
2.9	Three-dimensional, video-rate OCT optical setup schematic . . . . .	31
2.10	Schematic of imaged volume compared to hair sample . . . . .	32
2.11	Series of tomographic images of video-rate OCT acquisition on hair sample . . . . .	33
2.12	3D rendering of acquired volume images of hair sample . . . . .	35
3.1	JTFA with varying window size of an air-glass interface . . . . .	43
3.2	Optical setup for wavelength de-multiplexing . . . . .	45
3.3	Interferometric signals in zero and first diffraction order . . . . .	45
3.4	Spectroscopic OCT result of RG780 filter . . . . .	46
3.5	Spectra of back reflections of BK7 and RG780 filter . . . . .	47
3.6	Schematic of reflected intensities from front and rear interfaces . . . . .	47
3.7	Comparison of JTFA and wavelength de-multiplexing . . . . .	48
3.8	Spectroscopic OCT measurement of Nd-doped crystal . . . . .	51
3.9	Axial cuts of Nd-doped crystal measurement . . . . .	52
3.10	Spectral cuts of Nd-doped crystal measurement . . . . .	52
3.11	Spectral transmission curve of Nd-doped crystal . . . . .	53
3.12	Axial cuts of Nd-crystal measurement, log-scale . . . . .	53
3.13	Optical setup for wavelength de-multiplexing and SPDA . . . . .	56
3.14	ICG sample schematic . . . . .	57
3.15	Snapshot of online spectroscopic OCT display . . . . .	58
3.16	Temporal evolution of spatially resolved spectral transmission measurements . . . . .	59
3.17	Multi-resolution spectroscopic OCT setup . . . . .	63
4.1	Voice coil displacement curve . . . . .	68
4.2	Glass cube scanner principle . . . . .	68
4.3	Glass cube OPD variation . . . . .	69
4.4	Grating-based rapid-scanning optical delay line . . . . .	69
4.5	Optical setup double interferometer calibration . . . . .	70
4.6	Scanner calibration example, laser cw mode . . . . .	71
4.7	Scanner calibration example, identical measurements at different times . . . . .	72

4.8	Scanner calibration example, two different positions of optical contact . . . . .	72
4.9	Optical setup OPD calibration . . . . .	75
4.10	Calculated spectra of light source with and without scan correction . . . . .	76
4.11	Spectral shaping results . . . . .	77
4.12	Illustration of phase extraction procedure . . . . .	79
4.13	Illustration of resampling and interpolation procedure . . . . .	79
4.14	Illustration of spectral shaping . . . . .	81
4.15	Phase correction for numerical dispersion balancing . . . . .	82
4.16	Fiber-based realization of calibration method . . . . .	84
4.17	Amplification schemes for optical amplification of calibration signal . . . . .	84
4.18	Data treatment for real-time implementation of calibration method . . . . .	85

# Acknowledgements

I would like to express my gratitude towards the following colleagues who have helped me realize this work:

Theo Lasser, for accepting me in his group and providing me with the means for carrying out my research. René Salathé, for the fruitful scientific discussions and together with Adolf Fercher, Adrian Podoleanu and Pierre Jacquot for the critical evaluation of my work. Thomas Sidler, for his knowledgeable advice and the many pieces of equipment he lent me. Markus Pollnau, for the crystal samples he let me use for my measurements. Philippe Thévenaz, for his enormous help related to data treatment and image rendering and his ever so sharp questions. Thierry Blu, for his mathematical insights, availability for discussions, good humor and interest in my work. Michel Saint-Ghislain, for the numerous times he helped me out with fiber polishing and other delicate experimental questions - and for his particular kind of humor. Ronald Gianotti and Claude Amendola for their help and advice concerning electronic and mechanical problems. Judith Chaubert, Yvette Bernhard and Manuelle Borruat, for their administrative help. Sébastien Favre, for his enormous modesty and good humor. Rajesh Langoju and Adrian Bachmann for their interest in my work and for hopefully carrying it much further. Antonio Lopez, for his help with mechanics and logistics, good music in the lab and lots of jokes. Karsten Plamann, for many discussions and insights on scientific matters and numerous evenings with good food and good music. Stéphane Bourquin, for his calm and methodical analysis of problems and his tremendous help with questions related to the detector - and for the detector itself, of course. Tristan Bret, for his good questions and ideas, his keen interest and motivation and the detailed comments and corrections that have been incorporated in the present manuscript. Paolo Umari, Michele Merano and Ramachandra Rao, for the good times we had together on and off campus. Marcel Zeller, Tiemo Anhut, Alexander Serov, Kai Hassler, Marcel Leutenegger and Michael Goesch, for sharing the group's many fruitful and efficient meetings and coffee sessions.

My very special thanks go to the following people:

Mathieu Ducros, for the guidance he gave me in the first year of my Ph.D. and the many joyful moments we spent together in and outside the lab. I will always strive to reach his level of motivation and scientific rigor. Boris Karamata, for the close collaboration and the mutual psychological assistance in this difficult, but shared adventure. We have had countless scientific and personal discussions about everything from photons to professors over the years, which will leave a long lasting memory of complicity. I have never seen a person of more experimental perfection and more dislike for computers. Luc Froehly, for his impulse-response vision of optics, the constant availability for questions and discussions, for being a source of many questions and ideas, an enthusiastic scientist who really merits to be called one. Jelena Mitic, for sticking it out with me and Boris without losing hope and for the many good times we spent together outside the lab. Most of all, Varvara Valtchanova, for her encouragement and patience.



# Introduction

The principal medical imaging techniques that are found in today's hospitals are X-ray imaging, magnetic resonance imaging and ultrasound imaging. Scientific research aiming for the improvement of these methods and the discovery of new ones has been very active in recent time. As a result, a new optical imaging technique, called Optical Coherence Tomography (OCT) has been proposed in the early 1990s. Its principle is comparable to that of ultrasound imaging, with the fundamental difference that OCT uses light instead of sound for realizing echographic measurements. The resulting tomographic images are of micron-level resolution, but the method is limited to penetration depths of a few millimeters in scattering tissues. A short introduction to the technique's history, principle and uses is proposed to the non-specialist reader in chapter 1.

A major concern in OCT is imaging speed. For many medical applications the physician needs real-time image acquisition and display. Involuntary patient movements risk to distort the acquired images if imaging speed is not high enough. In order to take a tomographic, two-dimensional image, conventional OCT relies on two scan mechanisms to probe the sample: an axial depth scan that samples the light returning from different depth positions and a lateral scan that moves the point of investigation laterally in the second dimension. The achievable imaging speed is mainly determined by the maximum speed with which these scanning motions can be realized. Our institute has been working on the question of imaging speed for several years, notably developing an innovative, high speed depth scanning device that is based on the rotary movement of a glass cube. A more recent approach to the problem has been to eliminate the need of lateral scanning altogether by applying parallel detection to OCT. Instead of using a single photodetector and scanning a point illumination across the sample, parallel detection employs a detector array and direct wide-field imaging. Since OCT signals are composed of a weak modulated signal that contains the desired information on top of a strong static background, parallel OCT could benefit from a detector array capable of AC-coupled detection. Such a customized detector array for OCT has been developed within our institute. It makes use of the possibilities offered by CMOS technology to associate signal processing circuitry to each pixel in order to realize an AC demodulation on-chip. It has accordingly been named Smart Pixel Detector Array (SPDA).

At the beginning of my thesis, this device had only been tested on reflective surfaces and my initial objective was to extend its use to scattering objects, and further on, to identify other possible applications of this technology in the field of OCT. Chapter 2 is dedicated to the investigation of the SPDA's application to wide-field OCT in scattering and biological samples. The goal of this research is to demonstrate the feasibility of parallel detection and to show the detector's limitations in terms of sensitivity and imaging speed.

A currently very active research subject in the field of OCT is the technique's extension from purely morphological imaging to functional imaging. The goal is to find new ways to enhance contrast and extract more information from a sample. Polarization-sensitive OCT, used for imaging localized sample birefringence and Doppler OCT, capable of measuring spatially resolved flow velocities inside a sample, have been the first functional OCT modes. A more recent one is spectroscopic OCT, a promising concept capable of introducing new ways of image contrast and differentiating pathologies through the

measurement of localized spectroscopic properties. The currently employed methods for spectroscopic OCT rely on numerical post-processing for extracting spectroscopic information from conventional OCT signals. A completely experimental approach to this question is to optically divide the light into multiple wavelength channels and to use a detector array for parallel detection of the time-varying signals in the spectral domain. Such a wavelength de-multiplexing approach has been identified as an innovative application of the SPDA and is discussed in chapter 3. It allows for spectroscopic OCT imaging without the need for post-processing, which results in faster imaging speeds.

The experimental setup used for wavelength de-multiplexing has been the subject of many scientific discussions, resulting in an idea that could be of interest to low coherence interferometry in general. A well-known problem when striving for precise and repetitive measurements in time-domain low coherence interferometry is the non-linear movement and the random variations of the employed depth scan mechanism that introduce errors and noise. Research on scanning devices addresses this problem to the best of its ability, but for many applications it is necessary to monitor the exact optical path difference introduced by the scanner. This is commonly realized using a secondary interferometer with a high coherence source that shares with one of its arms the main interferometer's scanning device. Chapter 4 presents a method for measuring optical path difference variations that does not rely on a secondary interferometer and a secondary light source. It makes use of the fact that the temporal coherence of the principal light source can be increased by narrow spectral filtering, which creates a long coherence calibration signal that allows for the interferometric measurement of optical path difference variations over a whole scan.

The investigation of the described experimental concepts has given rise to four scientific publications that are integrated into the various chapters, forming the main body of this thesis. They are enriched by more detailed discussions that could not find a place in these concise publications, providing the reader with additional information and ideas for further research.

# Chapter 1

## Optical Coherence Tomography: history, principle and current research

A short introduction to the field of OCT is given in this chapter. It is mainly addressed to the non-specialist who is not yet familiar with OCT and who would like to get a concise overview of its history, principle and uses in order to better situate the work presented in this thesis. It is naturally beyond the scope and intention of this introduction to provide an exhaustive description of OCT. Very good reviews and books have been published on the subject, notably the recent review by Fercher *et al.* [1], a somewhat older one by Schmitt [2] and especially the new "Handbook of OCT" [3]. The interested reader should consult them for a more detailed and complete discussion on the subject.

### 1.1 OCT: evolution of a new imaging technique

#### 1.1.1 Widespread medical imaging techniques

The search for imaging techniques capable of looking non-invasively inside the living human body has a long history. A major break-through in this quest was the discovery of X-rays in 1895. Their omnipresence in today's hospitals testifies of the immense usefulness of X-ray based imaging. However, both the plane radiographic film implementation and Computerized Tomography (CT) are potentially harmful to living organisms. The ionizing radiation can cause cell nucleus modifications and destruction, leading to a host of ailments, notably cancer. The current strategy is to control the number of a patient's exposures and limit the employed doses, so as to respect a maximum annual radiation dose. Very sensitive X-ray detectors have now been developed that allow to reduce a patient's radiation dose to levels comparable to those experienced naturally during activities at high altitude, such as mountaineering or flight.

In the mid-1970s, a new tool, Magnetic Resonance Imaging (MRI), was invented. MRI is based on the detection of hydrogen nuclear spin relaxation and allows localisation and differentiation of most bodily tissues. The spins are lined up in a strong magnetic field and excited with radio frequency radiation. Upon relaxation they re-emit an electromagnetic pulse whose frequency depends on the local magnetic field strength. Choosing a gradient field permits to localize and image the hydrogen spins and thus the water and fat concentrations inside the body. MRI has been developed into a very precise and sensitive imaging tool that has so far not shown any adverse effects on patients' health.

Both CT and MRI are popular imaging modalities, but they represent large, complicated and expensive systems, requiring massive maintenance and specially trained operators. For many localized imaging needs, a smaller and more versatile tool is being used: ultrasound imaging. Here, acoustic waves with frequencies between 1.5 and 300 MHz are being employed to probe the body locally and measure the time delay of subsurface sound reflections induced by discontinuities in acoustic impedance. Ultrasound was

understood to be of potential imaging utility since the 1940s, borrowed from radar and sonar technology used during World War II. It has been applied for various medical purposes and has gained wide-spread acceptance in the 1970s. Today, two common uses of medical ultrasound devices are the imaging of the fetus during pregnancy and the detection of heart diseases. The technique has the disadvantage of requiring physical contact to the body in order to work.

### 1.1.2 OCT as new medical imaging technique

Optical coherence tomography is a more recent imaging modality that has been developed since the early 1990s. It is conceptually very similar to ultrasound, but works with light instead of sound. A light beam is focused locally onto the sample and the echo time delay and intensity of backscattered or back-reflected light is measured. The reconstructed images are essentially a map of changes in the index of refraction that occur at internal interfaces. OCT images these discontinuities in the index of refraction, or optical impedance, just as ultrasound images discontinuities in acoustic impedance. Because of the similarities between ultrasound and OCT, the terms A-scan and B-scan have the same meaning in both techniques. An A-scan is a one-dimensional, axial profile obtained at a point location and a B-scan is a two-dimensional, cross-sectional image of the sample that is built up from a series of laterally displaced A-scans.

Light and sound travel at very different speeds and the time scales associated to echo time delays in ultrasound and OCT are therefore quite different, too. The speed of sound in water is approximately 1500 m/s, that of light in water  $2.26 \times 10^8$  m/s. Measuring time delays in ultrasound requires a detection system with a temporal resolution of approximately 100 ns, which can easily be realized with modern electronic detectors. In the case of OCT, however, the temporal resolution of the detection system would have to be of the order of 30 fs, which is well beyond the limits of currently possible direct electronic detection. This is why in OCT the light echo coming back from the sample is not directly detected and evaluated for its time delay, but compared to a reference light signal that has previously been generated and that has traveled the same distance. This optical correlation technique is part of the field of optical interferometry and it is in low coherence interferometry and optical low coherence reflectometry where OCT has its origins.

Optical Low Coherence Reflectometry (OLCR) is an interferometric technique dating from the late 1980s that has been developed for one-dimensional ranging and fault detection in optical waveguides [4–6]. It uses light of low temporal coherence to discriminate between reflections originating from different axial positions inside the sample. An interferometric signal is only generated if the light echo coming back from the sample and the reference light beam have travelled the same distance to within the coherence length of the system's light source. This length determines the axial resolution of the measurement and depends on the degree of temporal coherence of the employed light source. The lower the temporal coherence, the better the achievable resolution. The amplitude of the interferometric signal is a measure of the reflectivity of discontinuities along the waveguide. In order to build up a depth-resolved reflectivity map, the path length travelled by the reference light has to be varied, thus achieving a so-called depth scan. The first application of low coherence interferometry in medicine was for eye length measurements [7]. Similar biometric studies using low coherence reflectometry were carried out in the following years [8–10]. In these ranging applications the acquisition of a one-dimensional signal was still sufficient. In 1991, the method was extended from one-dimensional, axial ranging to two-dimensional, cross-sectional (tomographic) imaging and given a new name: OCT [11]. The step from A-scan to B-scan is done by laterally translating the probing beam and acquiring a series of A-scans, to be displayed as a two-dimensional image.

The main advantage of OCT over other medical imaging methods is its high, micron-level resolution [12]. Neither CT, MRI nor ultrasound can offer the resolution of OCT. The downside is a lower



penetration depth than for the other methods due to light scattering in the sample. OCT probing depths in transparent tissues such as the eye exceed 2 cm, but are limited to approximately 2 mm in scattering tissues [13, 14]. However, with the conventionally used fiber-based light delivery and collection, OCT can easily be introduced into endoscopes and catheters and has even been demonstrated for intraluminal imaging [15]. Further advantages of OCT are its use of non-ionizing radiation, the problematic point of CT and its contact-free interaction with the sample, contrary to ultrasound imaging. Finally, OCT can be realized with a relatively simple, compact and flexible setup that is much cheaper than that of the other imaging methods.

method	avg resolution	max imaging depth	cost	comments
CT	1 mm	> 50 cm	high	ionizing radiation
MRI	1 mm	> 50 cm	high	slow
ultrasound	150 $\mu\text{m}$	15 cm	low	requires contact
OCT	1-10 $\mu\text{m}$	2 mm	low	non-contact

Table 1.1: Typical performances of principal medical imaging techniques

## 1.2 Major current research topics in OCT

### 1.2.1 Medical research

OCT is a very young imaging method that is still in the process of identifying the role it can play in the medical field and of establishing itself as a recognized and accepted technique. The most important medical applications that have so far been identified and developed are in the field of ophthalmology. With its high-resolution, depth-resolved imaging capabilities, OCT can detect and diagnose early stages of disease before irreversible loss of vision occurs. It enables the non-invasive, non-contact imaging of the anterior eye [16] and the retina [17, 18], thus helping notably with the diagnosis of various macular diseases [19] and glaucoma [20]. The first commercial OCT systems were introduced in ophthalmology in 1996 and many thousand patients have been examined with the technique so far.

Another important application of OCT is to assist and ideally replace excisional biopsy. Indeed, OCT images are sometimes referred to as "optical biopsies". For certain tissue pathologies excisional biopsy is dangerous for the patient or even impossible. In the case of atherosclerotic plaque, for example, OCT is being used to study its morphology *in situ* [21]. Conventional biopsy relies on taking samples of suspected tissue sites for analysis, but the diseased tissue can easily be missed, causing a high rate of false negative diagnoses. Sampling the tissue optically with OCT can guide conventional biopsy and reduce the false negative rates that are due to sampling errors. OCT can also help in detecting early neoplastic changes, the first stage of cancer. Studies are currently underway to use the technique for the diagnosis of early neoplasia in the gastrointestinal [22], female reproductive [23], pulmonary [24] and biliary tracts [25] and on skin [26].

The real-time imaging capacity of modern OCT systems makes it an interesting tool for guiding surgical or microsurgical intervention near or on sensitive structures like vessels or nerves [27]. It is also being used in dentistry, where the monitoring of the enamel de-mineralization permits early caries detection [28]. Ultra-high resolution OCT systems are starting to become interesting for developmental biology, being able to visualize mitotic activity, cell migration and even subcellular processes [29].

### 1.2.2 Improvement of imaging performance

Although already being applied to a number of medical problems, the technique itself is still evolving. Research and development concerned with the improvement of the method's imaging performance are very active. All the constituting elements of an OCT system have been reviewed and optimized and new imaging concepts have been studied in order to yield an ever higher imaging resolution, sensitivity and speed.

An important characteristic of OCT is the decoupling of axial and lateral resolutions. The latter is determined by the numerical aperture of the imaging optics, whereas the former is given by the temporal coherence of the employed light source. Improving the axial resolution in OCT has been a topic of research since its invention. Suitable light sources need to have a broad emission spectrum for high axial resolution, but also a high irradiance in order to achieve a high detection sensitivity. Broadband light sources such as ultra-short pulsed lasers [12], supercontinuum [30–32] and white light sources [33, 34] are being studied for use in OCT. Combining the outputs of several sources with different central wavelengths is another way for increasing the source bandwidth and thus the axial resolution [35]. The spectral form of the light source is also an important parameter. Ideally, it should be smooth and Gaussian-shaped in order to limit sidelobes and ringing noise effects in the OCT images. Experimental and numerical spectral shaping techniques have been developed to adapt the available light sources to this requirement [36, 37]. Numerical post-processing methods for resolution improvement are also being studied [38, 39]. In order to fully benefit from the potentially high axial resolution gained with broadband light sources, the optical

dispersion mismatch between the reference and sample arms has to be compensated for. For this purpose a number of experimental as well as numerical methods are being considered [40, 41].

Besides resolution, other important system parameters are sensitivity and imaging speed. The sensitivity of an OCT imaging system determines the maximum achievable penetration depth in scattering tissue. It depends on the illumination power and is inversely proportional to the imaging speed [9]. The study and elimination of noise sources is a constant preoccupation in order to optimize sensitivity [42]. Imaging speeds have mostly been limited by the available axial and lateral scanners. Improving their performance in terms of speed, stability and ease of use is a research topic by itself [43–45]. Novel approaches such as Fourier domain OCT or wide-field OCT are being investigated for their potential advantages in imaging speed, sensitivity and ease of implementation. In Fourier domain OCT the axial depth scan is replaced by a spectroscopic signal analysis that yields a whole A-scan trace without scanning. It is shown that this approach offers a sensitivity advantage over the traditional time domain OCT implementation [46, 47]. Wide-field or parallel OCT replaces the lateral scanning motions by imaging a whole sample surface onto a detector array instead of realizing point by point acquisitions with a single detector. The principal motivation for this approach is to increase the imaging speed and to simplify the optical setup. In order to yield satisfying results, parallel OCT depends on special detector systems or particular experimental techniques [48, 49].

Many OCT systems use spatially coherent laser sources and are subject to image degrading speckle effects. Speckle is generated by interference of waves with random phases that are due to the random depth and lateral distributions of scattering sites in the sample. Reducing the deleterious effects of speckle on OCT imaging is the subject of several studies [50, 51]. Speckle contrast can be reduced by averaging several uncorrelated speckle patterns. Various methods have been proposed that are able to generate uncorrelated speckle, such as polarization diversity, frequency diversity, spatial diversity or image post-processing [52–54].

### 1.2.3 New imaging modes: Functional OCT

Besides acquiring purely morphological images based on the spatial distribution of backscatterers or index discontinuities, OCT is able of imaging any other physical sample property that alters the amplitude, phase or polarization of the probing light beam. Extracting functional information about the sample by exploiting new contrast mechanisms is among the most interesting research topics in OCT today. The currently most developed imaging modes are polarization sensitive OCT, Doppler OCT and spectroscopic OCT.

Depth-profiling of tissue birefringence based on polarization-sensitive detection in an OCT system has already been investigated relatively early in the development of OCT [55]. Many tissue types such as muscle and tendons contain collagen and elastin fibers that exhibit birefringence when naturally aligned. Using polarization-sensitive OCT, this birefringence enhances contrast between different tissue types [56, 57]. Thermal damage destroys the alignment of fibers in tissue and imaging of thermal damage is therefore an important application of the polarization imaging mode [58].

Laser Doppler velocimetry is a method for the optical measurement of flow velocities based on the analysis of the Doppler-shifted frequency of light backscattered from a moving sample. It has been applied in the medical field for nearly three decades, notably on skin and in the eye [59, 60]. However, the size and the location of the probed sample volume can only coarsely be adjusted by the choice of the experimental geometry. Taking advantage of the precise localization capabilities of OCT, Doppler OCT can realize localized Doppler velocimetry inside a sample [61, 62]. This functional OCT mode has been demonstrated on a number of different phantoms, embryos and small animals [63] and important advances have been made concerning the accuracy, speed and sensitivity of the method in recent years.

Tissue spectroscopy is a field of biomedical optics trying to diagnose pathologies by the spectroscopic changes they induce in tissue. Back-reflected or backscattered light is analyzed for its spectral content and deviations from the original illumination spectrum are linked to pathological changes. However, the methods generally employed consider light coming back from everywhere inside the tissue. They are insensitive to spectroscopic variations with depth. Spectroscopic OCT is a combination of tissue spectroscopy and OCT [64, 65]. It aims to provide information on spectroscopic tissue properties localized in depth. The large spectral bandwidth of low coherence light needed for high axial resolution in OCT imaging allows for a spectrally extended analysis of tissue spectroscopy.

### 1.3 References

- [1] A. F. Fercher, W. Drexler, C. K. Hitzenberger, and T. Lasser. Optical coherence tomography - principles and applications. *Rep. Prog. Phys*, 66:239–303, 2003.
- [2] J. M. Schmitt. Optical Coherence Tomography (OCT): A Review. *IEEE Journal of selected topics in quantum electronics*, 5(4):1205–1215, 1999.
- [3] B. E. Bouma and G. J. Tearney, editors. *Handbook of Optical Coherence Tomography*. Marcel Dekker, Inc., 2003.
- [4] B. L. Danielson and C. D. Whittenberg. Guided wave reflectometry with micrometer resolution. *Applied Optics*, 26:2836–2842, 1987.
- [5] K. Takada, I. Yokohama, K. Chida, and J. Noda. New measurement system for fault location in optical waveguide devices based on an interferometric-technique. *Applied Optics*, 26(9):1603–1606, 1987.
- [6] R. C. Youngquist, S. Carr, and D. E. N. Davies. Optical coherence-domain reflectometry - a new optical evaluation technique. *Optics Letters*, 12(3):158–160, 1987.
- [7] A. F. Fercher, K. Menfedoht, and W. Werner. Eye length measurement by interferometry with partially coherent light. *Optics Letters*, 13:186–188, 1988.
- [8] X. Clivaz, F. Marquis-Weible, R. P. Salathé, Novak R. P., and H. H. Gilgen. High resolution reflectometry in biological tissues. *Optics Letters*, 17:4–6, 1992.
- [9] E. A. Swanson, D. Huang, M. R. Hee, J. G. Fujimoto, C. P. Lin, and C. A. Puliafito. High-speed optical coherence domain reflectometry. *Optics Letters*, 17(2):151–3, 1992.
- [10] J. M. Schmitt, A. Knüttel, and R. F. Bonner. Measurement of optical properties of biological tissues by low-coherence reflectometry. *Applied Optics*, 32(30):6032–6042, 1993.
- [11] D. Huang, E. A. Swanson, C. P. Lin, J. S. Schuman, W. G. Stinson, W. Chang, M. R. Hee, T. Flotte, K. Gregory, C. A. Pufialito, and J. G. Fujimoto. Optical coherence tomography. *Science*, 254:1178–1181, 1991.
- [12] W. Drexler, U. Morgner, F. X. Kartner, C. Pitris, S. A. Boppart, X. D. Li, E. P. Ippen, and J. G. Fujimoto. *In vivo* ultrahigh-resolution optical coherence tomography. *Optics Letters*, 24:1221–3, 1999.
- [13] Y. Pan, E. Lankenau, J. Welzel, R. Birngruber, and R. Engelhardt. Optical coherence-gated imaging of biological tissues. *IEEE Journal of Selected Topics in Quantum Electronics*, 2:1029–1034, 1996.
- [14] Y. Pan and D. Farkas. Non-invasive imaging of living human skin with dual-wavelength optical coherence tomography in two and three dimensions. *Journal of Biomedical Optics*, 3:446–455, 1998.
- [15] X. D. Li, T. H. Ko, and J. G. Fujimoto. Intraluminal fiber-optic Doppler imaging catheter for structural and functional coherence tomography. *Optics Letters*, 26(23):1906–1908, 2001.
- [16] J. A. Izatt, M. R. Hee, E. A. Swanson, C. P. Lin, D. Huang, J. S. Schuman, C. A. Puliafito, and J. G. Fujimoto. Micrometer-scale resolution imaging of the anterior eye *in vivo* with optical coherence tomography. *Archives of Ophthalmology*, 112:1584–1589, 1994.

- [17] E. A. Swanson, J. A. Izatt, M. R. Hee, D. Huang, C. P. Lin, J. S. Schuman, C. A. Puliafito, and J. G. Fujimoto. *In vivo* retinal imaging by optical coherence tomography. *Optics Letters*, 18:1864–1866, 1993.
- [18] A. F. Fercher, C. K. Hitzenberger, W. Drexler, G. Kamp, and H. Sattmann. *In vivo* optical coherence tomography. *American Journal of Ophthalmology*, 116:113–114, 1993.
- [19] C. A. Puliafito, M. R. Hee, C. P. Lin, E. Reichel, J. S. Schuman, J. S. Duker, J. A. Izatt, E. A. Swanson, and J. G. Fujimoto. Imaging of macular diseases with optical coherence tomography. *Ophthalmology*, 102:217–229, 1995.
- [20] J. S. Schuman, M. R. Hee, A. V. Arya, P. Pedut-Kloizman, C. A. Puliafito, J. G. Fujimoto, and E. A. Swanson. Optical coherence tomography: A new tool for glaucoma diagnosis. *Current Opinions in Ophthalmology*, 6:89–95, 1995.
- [21] M. E. Brezinski, G. J. Tearney, B. E. Bouma, J. A. Izatt, M. R. Hee, E. A. Swanson, J. F. Southern, and J. G. Fujimoto. Optical coherence tomography for optical biopsy: Properties and demonstration of vascular pathology. *Circulation*, 93:1206–1213, 1996.
- [22] J. A. Izatt, M. D. Kulkarni, H. W. Wang, K. Kobayashi, and M. V. Sivak. Optical coherence tomography and microscopy in gastrointestinal tissues. *IEEE Journal of Selected Topics in Quantum Electronics*, 2(4):1017–1028, 1996.
- [23] C. Pitris, A. Goodman, S. A. Boppart, J. J. Libus, J. G. Fujimoto, and M. E. Brezinski. High-resolution imaging of gynecologic neoplasms using optical coherence tomography. *Obstetrics and Gynecology*, 93:135–139, 1999.
- [24] C. Pitris, M. E. Brezinski, B. E. Bouma, G. J. Tearney, J. F. Southern, and J. G. Fujimoto. High-resolution imaging of the upper respiratory tract with optical coherence tomography: A feasibility study. *American Journal of Respiratory and Critical Care Medicine*, 157:1640–1644, 1998.
- [25] G. J. Tearney, M. E. Brezinski, J. F. Southern, B. E. Bouma, S. A. Boppart, and J. G. Fujimoto. Optical biopsy in human pancreatobiliary tissue using optical coherence tomography. *Digestive Diseases and Sciences*, 43:1193–1199, 1998.
- [26] J. Welzel. Optical coherence tomography in dermatology: a review. *Skin Research and Technology*, 7:1–9, 2001.
- [27] S. A. Boppart, B. E. Bouma, C. Pitris, J. F. Southern, M. E. Brezinski, and J. G. Fujimoto. Intraoperative assessment of microsurgery with three-dimensional optical coherence tomography. *Radiology*, 208:81–86, 1998.
- [28] B. T. Amaechi, A. G. Podoleanu, G. N. Kornarov, J. A. Rogers, S. M. Higham, and D. A. Jacksow. Application of optical coherence tomography for imaging and assessment of early dental caries lesions. *Laser Physics*, 13:703–710, 2003.
- [29] S. A. Boppart, B. E. Bouma, C. Pitris, J. F. Southern, M. E. Brezinski, and J. G. Fujimoto. *In vivo* cellular optical coherence tomography imaging. *Nature Medicine*, 4:861–865, 1998.
- [30] Y. M. Wang, Y. H. Zhao, J. S. Nelson, Z. P. Chen, and R. S. Windeler. Ultrahigh-resolution optical coherence tomography by broadband continuum generation from a photonic crystal fiber. *Optics Letters*, 28(3):182–184, 2003.

- [31] B. Povazay, K. Bizheva, A. Unterhuber, B. Hermann, H. Sattmann, A. F. Fercher, W. Drexler, A. Apolonski, W. J. Wadsworth, J. C. Knight, P. S. J. Russell, M. Vetterlein, and E. Scherzer. Submicrometer axial resolution optical coherence tomography. *Optics Letters*, 27(20):1800–1802, 2002.
- [32] I. Hartl, X. D. Li, C. Chudoba, R. K. Ghanta, T. H. Ko, J. G. Fujimoto, J. K. Ranka, and R. S. Windeler. Ultrahigh-resolution optical coherence tomography using continuum generation in an air-silica microstructure optical fiber. *Optics Letters*, 26(9):608–610, 2001.
- [33] E. Beaurepaire, A. C. Boccara, M. Lebec, L. Blanchot, and H. Saint-Jalmes. Full-field optical coherence microscopy. *Optics Letters*, 23(4):244–246, 1998.
- [34] A. F. Fercher, C. K. Hitzenberger, M. Sticker, E. Moreno Barriuso, R. Leitgeb, W. Drexler, and H. Sattmann. A thermal light source technique for optical coherence tomography. *Optics Communications*, 185:57–64, 2000.
- [35] Y. Zhang, M. Sato, and N. Tanno. Resolution improvement in optical coherence tomography by optimal synthesis of light-emitting diodes. *Optics Letters*, 26(4):205–207, 2001.
- [36] B. Povazay, A. Apolonski, A. Unterhuber, B. Hermann, K. K. Bizheva, H. Sattmann, P. S. Russell, F. Krausz, A. F. Fercher, and W. Drexler. Visible light optical coherence tomography. *Coherence Domain Optical Methods in Biomedical Science and Clinical Applications Vi*, 3(11):90–94, 2002.
- [37] R. Tripathi, N. Nassif, J. S. Nelson, B. H. Park, and J. F. de Boer. Spectral shaping for non-Gaussian source spectra in optical coherence tomography. *Optics Letters*, 27(6):406–8, 2002.
- [38] M. Bashkansky, M. D. Duncan, and J. Reintjes. Signal processing for improving field cross-correlation function in optical coherence tomography. *Applied Optics*, 37(34):8137–8138, 1998.
- [39] M. D. Kulkarni, C. W. Thomas, and J. A. Izatt. Image enhancement in optical coherence tomography using deconvolution. *Electronics Letters*, 33(16):1365–1367, 1997.
- [40] E. D. J. Smith, A. V. Zvyagin, and D. D. Sampson. Real-time dispersion compensation in scanning interferometry. *Optics Letters*, 27(22):1998–2000, 2002.
- [41] A. F. Fercher, C. K. Hitzenberger, M. Sticker, R. Zawadzki, B. Karamata, and T. Lasser. Dispersion compensation for optical coherence tomography depth-scan signals by a numerical technique. *Optics Communications*, 204(1-6):67–74, 2002.
- [42] W. V. Sorin and D. M. Baney. A simple intensity noise reduction technique for optical low-coherence reflectometry. *IEEE Photonics Technology Letters*, 4:1404–1406, 1992.
- [43] J. Szydlo, N. Delachenal, R. Gianotti, R. Walti, H. Bleuler, and R. P. Salathé. Air-turbine driven optical low-coherence reflectometry at 28.6-kHz scan repetition rate. *Optics Communications*, 154(1-3):1–4, 1998.
- [44] G. J. Tearney, B. E. Bouma, and J. G. Fujimoto. High-speed phase- and group-delay scanning with a grating-based phase control delay line. *Optics Letters*, 22(23):1811–1813, 1997.
- [45] A. V. Zvyagin, E. D. J. Smith, and D. D. Sampson. Delay and dispersion characteristics of a frequency-domain optical delay line for scanning interferometry. *Journal of the Optical Society of America A-Optics Image Science and Vision*, 20(2):333–341, 2003.

- [46] M. A. Choma, Sarunic M. V., C. Yang, and J. A. Izatt. Sensitivity advantage of swept source and Fourier domain optical coherence tomography. *Optics Express*, 11:2183–2189, 2003.
- [47] R. Leitgeb, C. K. Hitzenberger, and A. F. Fercher. Performance of Fourier domain vs. time domain optical coherence tomography. *Optics Express*, 11:889–894, 2003.
- [48] S. Bourquin, P. Seitz, and R. P. Salathé. Optical coherence topography based on a two-dimensional smart detector array. *Optics Letters*, 26(8):512–514, 2001.
- [49] L. Vabre, A. Dubois, and A. C. Boccara. Thermal-light full-field optical coherence tomography. *Optics Letters*, 27(7):530–532, 2002.
- [50] J. M. Schmitt, S. H. Xiang, and K. M. Yung. Speckle in optical coherence tomography. *Journal of Biomedical Optics*, 4(1):95–105, 1999.
- [51] M. Bashkansky and J. Reintjes. Statistics and reduction of speckle in optical coherence tomography. *Optics Letters*, 25(8):545–547, 2000.
- [52] K. M. Yung, S. L. Lee, and J. M. Schmitt. Phase-domain processing of optical coherence tomography images. *Journal of Biomedical Optics*, 4(1):125–136, 1999.
- [53] M. Pircher, E. Gotzinger, R. Leitgeb, A. F. Fercher, and C. K. Hitzenberger. Speckle reduction in optical coherence tomography by frequency compounding. *Journal of Biomedical Optics*, 8(3):565–569, 2003.
- [54] N. Iftimia, B. E. Bouma, and G. J. Tearney. Speckle reduction in optical coherence tomography by "path length encoded" angular compounding. *Journal of Biomedical Optics*, 8(2):260–263, 2003.
- [55] M. R. Hee, D. Huang, E. A. Swanson, and J. G. Fujimoto. Polarization-sensitive low coherence reflectometer for birefringence characterization and ranging. *Journal of the Optical Society of America A-Optics Image Science and Vision*, 9:903–908, 1992.
- [56] J. F. deBoer, T. E. Milner, M. J. C. vanGemert, and J. S. Nelson. Two-dimensional birefringence imaging in biological tissue by polarization-sensitive optical coherence tomography. *Optics Letters*, 22(12):934–936, 1997.
- [57] M. J. Everett, K. Schoenenberger, B. W. Colston, and L. B. Da Silva. Birefringence characterization of biological tissue by use of optical coherence tomography. *Optics Letters*, 23(3):228–230, 1998.
- [58] J. F. deBoer, S. M. Srinivas, A. Malekafzali, Z. P. Chen, and J. S. Nelson. Imaging thermally damaged tissue by polarization-sensitive optical coherence tomography. *Optics Express*, 3:212–218, 1998.
- [59] M. D. Stern. *In vivo* evaluation of microcirculation by coherent light scattering. *Nature*, 254:56–58, 1975.
- [60] T. Tanaka, C. Riva, and I. Ben-Sira. Blood velocity measurements in human retinal vessels. *Science*, 186:830–831, 1974.
- [61] Z. P. Chen, T. E. Milner, D. Dave, and J. S. Nelson. Optical Doppler tomographic imaging of fluid flow velocity in highly scattering media. *Optics Letters*, 22:64–66, 1997.
- [62] Z. P. Chen, T. E. Milner, S. Srinivas, X. J. Wang, A. Malekafzali, M. J. C. van Gemert, and J. S. Nelson. Non-invasive imaging of *in vivo* blood flow velocity using optical Doppler tomography. *Optics Letters*, 22:1–3, 1997.



- [63] S. Yazdanfar, M. D. Kulkarni, and J. A. Izatt. High resolution of *in vivo* cardiac dynamics using color Doppler optical coherence tomography. *Optics Express*, 1:424–431, 1997.
- [64] U. Morgner, W. Drexler, F. X. Kartner, X. D. Li, C. Pitris, E. P. Ippen, and J. G. Fujimoto. Spectroscopic optical coherence tomography. *Optics Letters*, 25(2):111–113, 2000.
- [65] R. Leitgeb, M. Wojtkowski, A. Kowalczyk, C. K. Hitzenberger, M. Sticker, and A. F. Fercher. Spectral measurement of absorption by spectroscopic frequency-domain optical coherence tomography. *Optics Letters*, 25(11):820–2, 2000.



## Chapter 2

# Parallel detection

The parallel detection or wide-field OCT concept aims to increase image acquisition speed and to simplify the optical setup by realizing direct wide-field sample imaging onto an array detector, instead of using lateral scanning devices and probing the sample point by point with a single-point detector as in conventional OCT. The first section of this chapter discusses the concept of parallel detection in OCT and presents various methods that have been elaborated by different research groups for achieving parallel heterodyne detection based on CCD cameras. Our approach makes use of a customized CMOS detector array that has specifically been developed for OCT within our institute. It associates a signal processing circuit to each pixel, capable of performing a demodulation of the interferometric OCT signal on chip, detecting directly the desired signal envelope. This device is described in detail in section 2.2.

At the beginning of this thesis, the CMOS detector had only been tested on reflective surfaces. This work is being continued here by extending its use to volumetric acquisition in scattering samples. In a first step, the feasibility of wide-field OCT based on this device is demonstrated experimentally on scattering samples in section 2.3. An artificial sample consisting of a reflective surface covered with scattering solution of varying concentrations is studied in order to estimate the sensitivity of the method. Then, three-dimensional OCT acquisitions are realized on onion peels. A principal advantage of parallel detection is the possibility of significantly increasing the imaging rate, making possible the realization of video-rate, three-dimensional OCT. This is demonstrated on a dynamically changing sample in section 2.4. The thermal deformations induced by the probing beam on a dark strand of human hair are imaged at 25 volume acquisitions per second.

## 2.1 Concept of and approaches to parallel OCT

### 2.1.1 Parallel detection: advantages and disadvantages

Most current OCT systems are based on a point by point scanning approach, illuminating one surface point of the sample at a time and translating that illumination to neighboring points in order to build up a tomogram or a three-dimensional image. These schemes therefore rely on three scanning motions for three-dimensional imaging, one for depth scanning and two for lateral scanning of the illumination point. The idea of parallel detection is to implement an optical imaging system that images the light coming from a whole surface of the sample onto a two-dimensional detector array, thus eliminating the need for lateral scanning. A major advantage of parallel detection is therefore a simplification of the experimental setup. Only one axial depth scan is required. Furthermore, the acquisition of  $N$  pixels in parallel relaxes the requirements on the depth scanning device for a given image acquisition speed.

The image acquisition speed in OCT is generally limited by three factors: the depth scan speed  $V$  of the delay line, the data acquisition rate  $r$  of the detection system and the acceptable signal-to-noise ratio

(SNR) of the measurement. The latter is intricately linked to the optical power of the employed light source and thus translates to a limitation due to the source. A system's maximum theoretical signal-to-noise ratio ( $SNR_{th,max}$ ) in the case of shot-noise limited detection is given by the following formula [1, 2]:

$$SNR_{th,max} = 10 \log \left( \frac{\eta}{2h\nu} \frac{P_{s,max}}{B} \right) \quad (2.1)$$

$P_{s,max}$  is the maximum optical power backreflected from the sample as seen by one photodiode of the detector array,  $B$  stands for the power equivalent detection bandwidth,  $\eta$  is the quantum efficiency,  $h$  Planck's constant and  $\nu$  the optical frequency of the light used. The optimum detection bandwidth  $B$  to reject as much noise as possible without attenuating the OCT signal is considered to be twice the width of the signal's frequency band  $\Delta f$ , as discussed by [2]. The latter is centered at the Doppler frequency  $f_{Doppler}$  that is determined by the source spectrum central wavelength  $\lambda$  and the depth scan speed  $V$

$$f_{Doppler} = \frac{2V}{\lambda} \quad (2.2)$$

$$\Delta f = 2V \frac{\Delta\lambda}{\lambda^2} \quad (2.3)$$

$$\Delta f = \frac{\Delta\lambda}{\lambda} f_{Doppler} \quad (2.4)$$

Using equations 2.2 and 2.4 for substituting  $B$  in equation 2.1, we obtain a relationship linking the maximum SNR to the optical power and the depth scan speed

$$SNR_{th,max} = 10 \log \left( \frac{\eta}{8h\nu} \frac{\lambda^2}{\Delta\lambda} \frac{P_{s,max}}{V} \right) \quad (2.5)$$

In the case of the parallel detection of  $N$  pixels, the optical power received by one detector element is  $N$  times lower than the power detected in the single-photodiode approach, considering the same light source. Thus, for the same SNR and the same overall image acquisition speed as in the point-scanning approach, the depth scan speed  $V$  can be reduced by a factor  $N$  in the parallel approach. This relaxation on the requirements of the scanning device are exchanged for an increased demand in the data acquisition rate, which has to be now a factor  $N$  higher than in the single-detector approach in order to receive the increased data flow. The principal limitation for the imaging speed with parallel detection is therefore the available data acquisition speed.

Three important points should still be noted in this context. First, equations 2.1 and 2.5 are only valid for shot-noise limited detection. An infinite increase in the light power will not lead to an infinite SNR, because other noise sources, notably the source relative intensity noise, will become dominant (see [3]). Second, the optical power separation onto  $N$  pixels generally results in power losses due to a geometrical mismatch between the circular illumination spot and the rectangular detector and losses due to the detector fill factor. Third, parallel detection does not mean simultaneous detection of  $N$  pixels, because the pixel read-out is generally done sequentially. In other words, the mechanical lateral scan of the beam is replaced by an electronic scan of the different pixels.

The wide-field illumination of parallel schemes allows for the use of a larger variety of light sources than the point scanning approach. For high lateral resolution and optimal fiber coupling, point scanning systems depend on sources with high spatial coherence. On the other hand, those light sources need to be of low temporal coherence in order to obtain high axial resolutions. These conditions are only met for highly specialized and expensive sources such as femtosecond lasers, supercontinuum sources or superluminescent diodes. For parallel OCT one can use spatially incoherent illumination as provided by much cheaper thermal light sources without sacrificing axial resolution. Furthermore, thermal sources

exhibit larger spectral bandwidths than sources conventionally used for OCT and achieve among the highest axial resolutions yet reported [4–6]. The principal drawback is a lower sensitivity than with spatially coherent laser-based systems due to a lower source brightness per spatial mode.

Another reason for using spatially incoherent light sources for parallel OCT is the problem of optical cross talk. Wide-field illumination of a scattering sample creates much more backscattered light than point illumination. Furthermore, the parallel scheme cannot rely on a confocal filtering effect like the one present in the point scanning approach to reduce the level of multiple scattered light reaching the detector. Multiple scattered light cannot be used for diffraction limited imaging, because its angle of incidence on the optical system is not directly related to the location of the original scattering site. If a spatially coherent illumination is used in parallel OCT, multiple scattered light can interfere with the reference field and create an erroneous OCT signal. On the other hand, if spatially incoherent light is employed, interference can only take place if spatially coherent zones in the sample and reference fields are matched. This condition acts like a filter, eliminating the interference and thus detection of multiple scattered light. The important question of optical cross talk in the context of parallel OCT has been studied by Karamata [7–9].

A very important practical aspect is the question of a system's handling and maintenance in a clinical setting. Fiber-based point scanning systems can easily be integrated in endoscopic and catheter applications and require little adjustment or alignment. The only element that needs to be made available to the user is the optical fiber to illuminate the sample. The rest of the system can safely be stowed away in a box and easily be made shock-, spill- and heat-resistant. A parallel detection system on the other hand depends on bulk imaging optics and is therefore more difficult to handle and align. For clinical applications it could be integrated into a surgical microscope or used with biological samples that fit under a microscope stand.

### 2.1.2 CCD-based approaches to parallel detection

Parallel detection relies on a detector array for image acquisition. The most easily available commercial photodetector arrays today are charge-coupled devices (CCDs). These are semiconductor devices that use an electric potential well associated to each photosensitive area to store the photo-electrons that are generated by the incoming radiation. The accumulated charges, corresponding to an integrated measurement, are then emptied line by line and the associated voltage is a measure of the number of photons detected.

The direct use of CCD cameras for heterodyne detection in time-domain OCT is limited mainly by two factors:

- The high optical DC intensity reflected by the reference mirror reduces the dynamic range available for AC interferometric signal detection. No AC coupling is possible to increase the dynamic range for the information-containing AC part. CCDs suffer therefore from a low dynamic range for AC detection, even though the sensitivity of the devices can be quite high.
- The standard CCD frame rates (typically  $\approx 100$  Hz for  $512 \times 512$  pixels) are much lower than the typically used signal Doppler frequencies ( $>1$  kHz). Therefore, the depth scan speed has to be drastically reduced in order to permit sufficient sampling of the interferometric signal with the low CCD frame rate. The result is a very slow image acquisition.

CCD cameras can nevertheless be used for parallel OCT measurements if the heterodyne detection method employed in point scanning implementations is replaced by a phase stepping method. The relatively slow frame rate of CCD cameras is then no limitation anymore, because no high frequency

interferometric signal, but only a few phase-stepped images have to be acquired. However, the low dynamic range remains a weak point of CCD implementations. The following methods use CCD cameras for parallel OCT. They differ mainly in the way the phase steps are realized and in the type of algorithm used to extract the envelope of the modulated optical signal. A review of phase-stepping algorithms in interferometry can be found in [10].

### **Temporally multiplexed phase-shifting by stroboscopic illumination**

Boccara *et al.* have developed a method for performing lock-in detection of a coherent signal in parallel on a CCD based on stroboscopic illumination [4, 11, 12]. They use a fast photoelastic birefringence modulator to introduce a sinusoidal phase shift between the sample and reference waves. The interferometer light source is synchronized with the phase modulator and is only switched on for one quarter of the modulation period. After the acquisition of one CCD frame the illumination is shifted in time by a quarter of the modulation period and a second frame is acquired. Four images with different interference fringe patterns are thus recorded successively and used to calculate one optically sectioned *en face* image.

### **Frequency synchronous detection using liquid crystal shutters**

Akiba *et al.* use two CCD cameras equipped with fast liquid-crystal shutters to realize two-dimensional heterodyne detection [13, 14]. They employ an axially scanned reference mirror to generate a heterodyne frequency. The light in the interferometer's detection arm is separated and projected onto two CCD cameras with high-speed shutters synchronized to the Doppler frequency. The two shutters are phase-shifted by  $\pi/2$ , allowing for the simultaneous acquisition of the in-phase and quadrature components of the heterodyne signal. Three images shifted by a phase of 0,  $\pi/2$  and  $\pi$  are acquired to reconstruct numerically the interference signal intensity.

### **Sequential phase-stepping of reference mirror**

Sequential phase-stepping of the interferometer's reference mirror with the help of a piezoelectric translation stage and the acquisition of four phase-shifted images on a CCD is realized by several authors [5, 15–17]. The final image is calculated based on the phase-shifted frames. After each four-frame acquisition the sample is translated longitudinally and the procedure is repeated in order to build up a three-dimensional image.

### **Spatially separated, single-shot, phase-stepped imaging**

Dunsby *et al.* propose a method that is capable of acquiring four phase-shifted images on the four quadrants of a single CCD camera in a single shot [18]. It is based on a four-channel polarisation phase-stepped imaging setup that spatially separates the interferometer light into four images, each of which being phase-shifted by  $\pi/2$  by an ingenious combination of polarizing beam splitters and quarter-wave plates.

## **2.1.3 CMOS-based approach to parallel detection**

The technological progress in semiconductor devices of the last decade has enabled the production of ever cheaper and more sophisticated image sensors based on the Complementary Metal-Oxide-Semiconductor (CMOS) technology. CMOS sensors offer the possibility of integrated and customized signal processing on chip. Each pixel can have an associated electronic circuit that directly treats the received data even

before it leaves the detector. In this manner highly specialized processing tasks can be designed, resulting in very unique detector systems that can overcome the limitations of CCDs.

Such a customized CMOS detector array has been conceived for parallel heterodyne detection, as is required for direct parallel OCT. To our knowledge it is the first of its kind. This device has been used extensively in this thesis and will be described in the next section.

## 2.2 Smart pixel detector array

### 2.2.1 Working principle and characteristics

Bourquin *et al.* have developed the first specialized CMOS image sensor for parallel OCT [19–21]. This prototype device consists of 58 by 58 pixels, with a demodulation circuit associated to each pixel. Because of this pixel-specific signal processing capabilities, it has been named Smart Pixel Detector Array (SPDA). Each pixel realizes in parallel the data treatment operations indicated in figure 2.1.

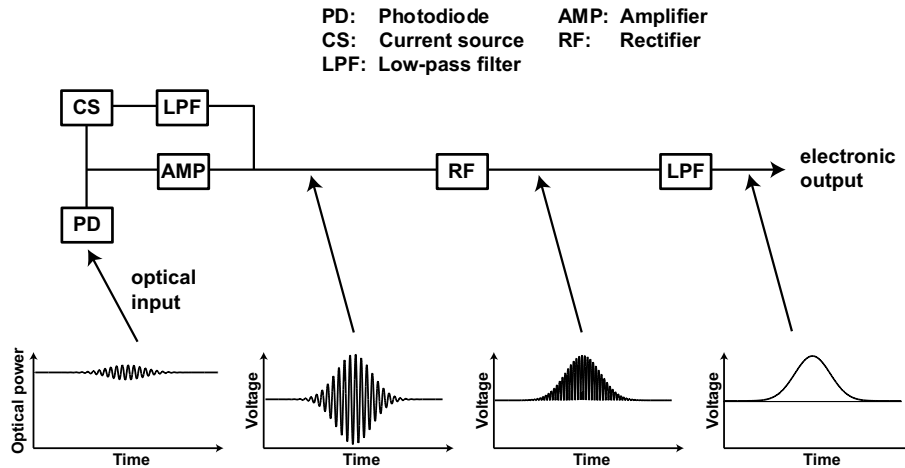


Figure 2.1: SPDA pixel functionality. Complete AC coupling and envelope detection is realized on each pixel in parallel.

Starting with a typical incoming OCT signal that is composed of a large DC optical power modulated with a small AC component, the first processing step is an AC coupling of the detected optical signal. This is realized with a feedback loop consisting of an amplifier, a low-pass filter and a current source. The latter delivers just enough current to counterbalance the photo current generated by the optical DC power. This DC level is determined through the low-pass filter that in turn controls the current source. The resulting AC signal is then amplified, rectified and finally low-pass filtered in order to extract its envelope. The exact working points of the different processing elements, such as filter bandwidths and amplification gain can be adjusted externally by reference voltage settings leading to the detector chip. Those settings depend on the DC optical power and have to be adapted to the particular light source or sample used.

The significant advantage of this treatment over a direct readout of the interference signal is that the resulting envelope signal can now be sampled at a much lower frequency than would have been necessary for the original interferometric signal. However, once calculated for each pixel in parallel, the envelope signal is being sampled and read out sequentially, row by row and column by column. The readout principle is schematically indicated in figure 2.2.

The readout process is controlled by an external electronic circuit that pilots the row and column address decoders. These are part of the detector chip and are responsible for switching the pixel and column buffers according to the address information received externally. The buffers in turn act as gates that connect the voltages currently present at their entry to the output. By sequentially addressing the different pixels and connecting them to the output, a continuous series of voltages is generated that constitutes the detector signal.

It becomes clear that the SPDA by itself, consisting only of photo detectors, signal processing circuitry and address decoders, is not a complete functioning system. It needs to be supplied with power,



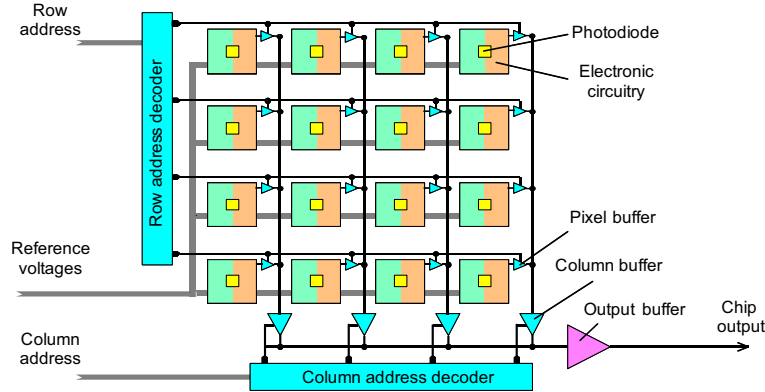


Figure 2.2: SPDA sequential readout principle. The electronic circuitry associated to each photodetector realizes the data treatment operations indicated in figure 2.1. It is controlled by an externally adjustable set of reference voltages. Row and column address decoders are piloted by an external readout electronics. They control the pixel and column buffers that act as gates to connect each pixel sequentially to the detector output buffer.

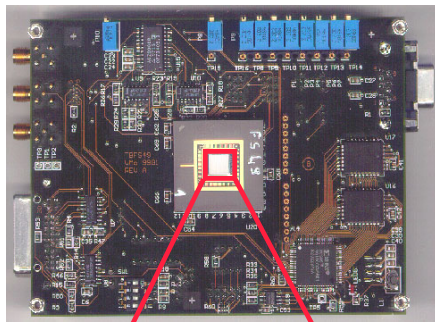
reference voltages and address signals. These functions are realized by standard electronic elements that are mounted together with the chip on an electronic board. The system as a whole is connected to a laboratory DC power supply and requires as input a TTL frame trigger signal, initiating the readout of the detector array. The readout itself is timed by an on-board quartz-driven system clock running at 10 MHz that can be reduced by multiples of two down to 78.125 kHz. The maximum clock frequency that does not induce image deformations is 5 MHz. For each clock pulse the output buffer is connected to another pixel, until the whole array has been read. The system then waits for the next frame trigger in order to repeat the detector readout cycle. Both the pixel trigger signal and the output signal are available to the user. Using a standard RS232 serial protocol the readout electronics can be instructed to use only a subarray of the detector. Equally, the reference voltages that control the amplification and filtering characteristics of the signal processing circuitry can be adjusted via RS232.

The entire detection and processing circuitry, up to and including the detector output is analog. Only the readout electronics and trigger clocks are digital. The maximum dynamic range obtained with the device is 55 dB. Pictures of the whole detector system, the SPDA chip and a pixel detail, together with a summary of the main physical characteristics can be seen in figure 2.3.

### 2.2.2 Current SPDA applications

Since its development, the SPDA has seen a host of interesting applications, in OCT of course, but also in other fields of optics. In the following two sections two publications discuss the experimental work realized in the context of this thesis in the field of parallel OCT. In the first one, the feasibility of parallel OCT using a smart CMOS detector in scattering samples is demonstrated. The possibility for fast three-dimensional OCT using a parallel detection scheme and a SPDA is the subject of the second publication. Furthermore, the SPDA has also been employed for spectroscopic OCT based on the wavelength demultiplexing method, as described in chapter 3.

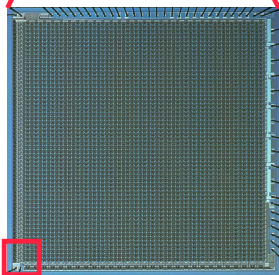
Outside the field of OCT, the detector has been used for a new femtosecond pump-probe spectroscopy method permitting high-speed, parallel acquisition of pump-probe measurements at multiple wavelengths [22]. Femtosecond pump-probe spectroscopy is a technique for investigating ultrafast phenomena in condensed matter, chemical, and biological systems. In this case, spectrally resolved measurements of carrier dynamics in a thin sample of bulk GaAs were demonstrated. The 250nm-bandwidth probe beam was spectrally analysed with a diffraction grating and projected onto one line of the SPDA, thus



## SPDA and readout board

### Readout electronic features:

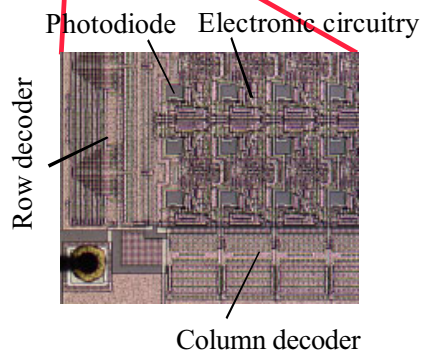
- Pixel pattern to readout programmable by PC
- Data readout rate: up to 5 Mpixel/sec
- Dimensions: 130 x 100 x 30 mm



## SPDA chip

### Chip specifications

- Process : CMOS 2  $\mu\text{m}$
- Dimensions : 7.2 mm x 7.2 mm
- Pixel number : 58 x 58
- Power supply : 5V
- Power dissipation: 300mW



## Pixel detail

### Pixel parameters

- Dimensions : 110  $\mu\text{m}$  x 110  $\mu\text{m}$
- Photodiode dimensions : 35  $\mu\text{m}$  x 35  $\mu\text{m}$
- Fill factor : 10 %

Figure 2.3: Photographs of the SPDA detector system and its main characteristics.

associating the 58 neighboring pixels to 58 different wavelength channels.

In another application, the SPDA was successfully employed to realize wide-field optical sectioned microscopy based on a structured illumination method [23]. Structured illumination introduces high spatial frequencies into the image whose contrast decreases much faster with de-focusing than the naturally present spatial frequencies of the sample due to the optical transfer characteristics of microscope objectives. In this manner, out-of-focus light is more efficiently rejected, resulting in optically sectioned images. By continuously varying the illumination pattern, a time-varying optical signal is generated on each pixel of the detector array whose amplitude corresponds to the optically sectioned image pixel value. The SPDA realizes this envelope detection on-chip and provides the user directly with the optically sectioned image.

## 2.3 Parallel optical coherence tomography in scattering samples using a two-dimensional smart-pixel detector array

(published in Optics Communications 202 (2002) 29-35, 1 February 2002)

M. Ducros, M. Laubscher, B. Karamata, S. Bourquin, T. Lasser and R. P. Salathé  
Institute of Applied Optics, Swiss Federal Institute of Technology, CH-1015 Lausanne, Switzerland

### ABSTRACT

Parallel optical coherence tomography in scattering samples is demonstrated using a 58 by 58 smart-pixel detector array. A femtosecond mode-locked Ti:Sapphire laser in combination with a free space Michelson interferometer was employed to achieve 4  $\mu\text{m}$  longitudinal resolution and 9  $\mu\text{m}$  transverse resolution on a 260x260  $\mu\text{m}^2$  field of view. We imaged a resolution target covered by an intralipid solution with different scattering coefficients as well as onion cells.

### 2.3.1 Introduction

Optical coherence tomography (OCT) allows acquisition of spatially resolved maps of reflectivity in scattering samples. In most common OCT systems, depth scanning is achieved by the longitudinal translation of a reference mirror, and lateral scanning is obtained by the lateral translation of a focused probe beam using scanning mirrors [24–26]. To increase the acquisition speed and eliminate the need for lateral scanning, parallel detection schemes have been investigated [12, 19, 27–29]. Parallel OCT systems previously developed consist of a free-space Michelson interferometer illuminated by a short temporal coherence source. The sample under study is placed in one arm of the interferometer, illuminated with a uniform extended beam and imaged on an array of photodetectors. Charge coupled devices (CCD) cameras are the most commonly used imaging devices for parallel detection schemes. However, CCD cameras suffer from two drawbacks when used in parallel OCT systems:

- the high optical DC intensity reflected by the reference mirror reduces the dynamic range available for AC interferometric signal detection,
- the CCD frame rate (typically  $\approx 100$  Hz for 512x512 pixels) is much lower than the interferometric signal frequency (typically  $> 1$  kHz).

In this case a lock-in detection or synchronous illumination scheme has to be employed [12], which limits the image acquisition speed. A different photodetector array based on CMOS technology was developed for parallel OCT [19, 20]. Besides transducing light signals into electrical signals, CMOS detectors offer the additional functionality of customized, integrated signal processing for each pixel. Such smart pixel detector arrays (SPDA) have been developed for OCT interferometric signal demodulation. The feasibility of using one- and two-dimensional SPDAs for OCT was demonstrated on reflective surfaces [19, 29]. In the present work we demonstrate the feasibility of employing a SPDA to obtain parallel OCT images in scattering samples.

### 2.3.2 Method

#### Optical set-up

The optical set-up is illustrated in figure 2.4. The output of a femtosecond mode-locked Ti:Sapphire laser (MLTS) is coupled into 100 m of single-mode optical fiber in order to reduce peak pulse powers by pulse stretching. Dispersion in the fiber increases the temporal width of the laser pulses, which reduces

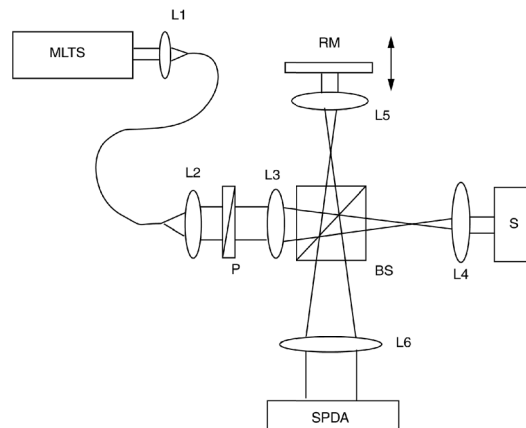


Figure 2.4: Optical setup schematic. The different elements are: mode-locked Ti:Sapphire femtosecond laser (MLTS); achromatic lenses ( $L1=f8$ ,  $L2=f40$ ,  $L3=f140$ , and  $L6=f200$ ); linear polarizer (P); non-polarizing achromatic beamsplitter cube (BS); achromatic microscope objectives 20X, 0.45NA ( $L4$  and  $L5$ ); reference mirror (RM); 58 by 58 smart pixel detector array (SPDA) and sample (S).

dramatically the peak power. This precaution is taken to avoid damage to the sample and the optics. The fiber output is collimated by lens  $L2$  and linearly polarized by polarizer P. An average power of 100 mW is coupled into a free space Michelson interferometer. The light spectrum is nearly Gaussian and has a full-width at half-maximum of 70 nm centered at 800 nm. The resulting system axial resolution is 4  $\mu\text{m}$ . A non-polarizing beamsplitter cube (BS) separates the light into the interferometer reference and sample arms. Two identical 20x achromatic microscope objectives ( $L4$  and  $L5$ ) are used to illuminate and collect reflected light from the sample (S) and the reference mirror (RM). Light reflected from S and RM interferes only if the optical path lengths match to within the source coherence length. RM is translated longitudinally using a voice coil scanning stage at a speed of 1.17 mm/s inducing a heterodyne interference signal at a frequency of 2.9 kHz. The sample is imaged onto the detector (SPDA) with a magnification of 25 by lens  $L6$  and microscope objective  $L4$ . The detector is composed of 58 by 58 smart pixels. One pixel consists of a  $35 \times 35 \mu\text{m}^2$  silicon photodiode coupled to a CMOS electronic circuit that amplifies and demodulates AC signals, delivering an analog voltage proportional to the envelope of the optical interference signal [19, 20]. The photodiode covers 10% of the total pixel area ( $110 \times 110 \mu\text{m}^2$ ), the rest being occupied by the CMOS electronic circuit. Due to the detector photosensitive fill factor and to optical system losses, the DC optical power reflected from the reference mirror and incident onto each photodiode is 170 nW. The incident power on the sample corresponding to one photodiode area of the detector is 340 nW. The pixels are read out sequentially. The output voltage is digitized by an external 12-bit A/D card at a sampling rate of 2.5 MHz and stored in a computer memory. Volumetric images consisting of  $58 \times 58 \times 600$  voxels ( $260 \times 260 \times 950 \mu\text{m}^3$ ) are acquired in 0.8 s. The user can display on a computer screen any 2-dimensional cross-sectional image from the three-dimensional data set.

Due to the small depth of field (Rayleigh range of 4.6  $\mu\text{m}$ ) of the microscope objectives  $L4$  and  $L5$ , care has to be taken to place the region of interest in the sample at the focal plane of  $L4$ . Replacing temporarily the SPDA with a standard CCD camera we adjusted the longitudinal position of the sample with a micrometer translation stage to obtain a focused image on the CCD camera.

### Samples

Two kinds of sample were used in the present work. Sample 1 is a cuvette constructed with four microscope cover slips glued on a USAF resolution target (Fig.2.5). A drop of intralipid scattering solution is

deposited in the cuvette and a top cover slip is pressed down to close the cuvette and remove the excess solution. We varied the intralipid solution scattering coefficient ( $\mu_s$ ) between  $0 \text{ cm}^{-1}$  and  $100 \text{ cm}^{-1}$  by dilution of 20% Lipovenös® intralipid solution (Fresenius AG, Switzerland).  $\mu_s$  was measured using the collimated transmission method described van Staveren *et al.* in reference [30].

Note that the total thickness of the sample is superior to the depth of field of L4, which means that it is impossible to have a well-focused image for all depth positions in one scan. The transverse resolution is optimum at the focal plane and degrades below and above. However, scanning the whole volume of the sample provides an accurate measurement of the thickness of the intralipid solution that can vary slightly due to a liquid film between the cover slip. The USAF resolution target was placed at the focal plane of L4.

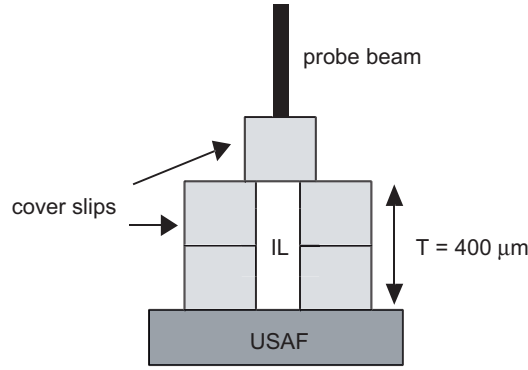


Figure 2.5: Schematic of sample 1. The probe beam illuminates from top to bottom one microscope cover slip, a scattering intralipid solution (IL) approximately  $400 \mu\text{m}$  thick, and the USAF resolution target.

Sample 2 is an onion. The probe beam penetrates from the outer surface of the onion. Images are acquired with the focal plane placed at the surface and approximately  $100 \mu\text{m}$  below the surface.

### 2.3.3 Results and discussion

#### System performances

We measured the system longitudinal response on a mirror in air to be  $4 \mu\text{m}$ . The depth resolution measurement was repeated on the reflective bars of the USAF resolution target placed behind a layer of scattering intralipid solution (sample 1) and the same result was obtained taking into account the index of refraction of intralipid (1.33). Thus, neither scattering nor dispersion degrades the system longitudinal resolution as measured in sample 1. Transverse resolution in air was determined using the USAF resolution target patterns. We could resolve reflective bars with a maximum spatial frequency of 114 lines/mm, which corresponds to a transverse resolution of  $8.8 \mu\text{m}$ .

We define the signal to noise ratio (SNR) as the ratio between the following two quantities:  $V_{\text{signal}}$ , the detector output voltage for a voxel that corresponds to the image of a reflective site (such as a USAF reflective bar, a mirror or a backscattering in a biological sample) and  $\sigma_{\text{noise}}$ , the standard deviation of the measured voltage on all voxels without a sample. SNR in decibel is:

$$SNR(\text{dB}) = 20 \log \frac{V_{\text{signal}}}{\sigma_{\text{noise}}} \quad (2.6)$$

When the sample is a gold mirror with reflectivity 0.98 we measure  $SNR=50 \text{ dB}$ , which we consider to be the maximum SNR obtainable with our system.

For a rigorous performance analysis this value has to be compared to the maximum theoretical SNR ( $SNR_{th,max}$ ) for a shot-noise limited system, which is given by the following formula [1, 2]:

$$SNR_{th,max} = 10 \log \left( \frac{\eta}{2h\nu} \frac{P_{s,max}}{B} \right) \quad (2.7)$$

where  $P_{s,max}$  is the maximum power coming from the sample arm (as seen by one photodiode of the detector),  $B$  the detection bandwidth,  $\eta$  the quantum efficiency,  $h$  Planck's constant and  $\nu$  is the optical frequency of the light used. We have measured the bandwidth of the SPDA detector tuned for optimum performances in the experimental conditions to be 120 kHz and estimate the quantum efficiency to be 0.5, which gives a theoretical shot-noise limited SNR of 61.5 dB. The observed detection limit was thus 11.5 dB above the shot-noise limit. We attribute this difference to additional read-out noise generated by the electronic circuitry.

Note that the optimum filtering bandwidth  $B$  to filter out as much noise as possible without attenuating the OCT signal is given by [2]

$$B = 2 \frac{\Delta\lambda}{\lambda} f_{Doppler} \quad (2.8)$$

$\Delta\lambda$  being the source spectrum full width at half maximum,  $\lambda$  the source spectrum central wavelength and  $f_{Doppler}$  the interference fringes frequency. In the current experimental settings,  $B$  is 508 Hz, and the maximum obtainable shot noise limited SNR is 85 dB.

The large filtering bandwidth of 120 kHz used in our experiments is due to an intrinsic limitation of the electrical circuitry of the SPDA for the given experimental conditions. Indeed, being conceived for heterodyne frequencies of the order of 100-300 kHz, this detector has a rather poor filtering performance for low heterodyne frequencies. Furthermore, the achievable minimum filtering bandwidth also increases with the light power illuminating the detector, which was in the current study rather higher than in previously published experiments [19]. We have nevertheless employed a slow reference mirror scanning velocity (resulting in a low OCT signal frequency of 2.9 kHz) in order to sample the high axial resolution (4  $\mu m$ ) given by the short temporal coherence of the femtosecond laser source. The bottleneck is the pixel read-out rate of 2.5 MHz (5 MHz with some reduction in image contrast), which does not permit to sample a sufficient number of points per coherence envelope at high heterodyne frequencies.

### Images of USAF resolution target

In Fig. 2.6 are presented longitudinal cross section (Fig. 2.6a) and *en face* images (Fig. 2.6b/c) of sample 1. The sample longitudinal position is adjusted to bring the surface of the resolution target into focus on the SPDA. The field of view is centered on elements 5 and 6, group 4, of the resolution target. In Figures 2.6a and 2.6b the target is covered by 400  $\mu m$  water. The three lines in Fig. 2.6a at optical distances of 0, 270 and 800  $\mu m$  correspond to the two interfaces of the glass slide and the resolution target, respectively. The optical thickness measured on the longitudinal cross-sections (e.g. Fig 2.6a.) is used to determine the physical thickness of intralipid solution, assuming an index of refraction of 1.33. In Fig. 2.6c the resolution target is covered by 385  $\mu m$  intralipid solution with  $\mu$  of 100  $cm^{-1}$ , which corresponds to nearly 4 scattering mean free paths (single pass). For greater scattering samples the pattern was undistinguishable.

For a quantitative assessment of imaging performance, the signal from a reflective bar of the USAF resolution target was measured as a function of the number of scattering mean free paths in the intralipid solution, also called one-way optical depth (OD). The results are presented in term of SNR as a function of OD (Fig. 2.7), with

$$OD = \mu_s t \quad (2.9)$$

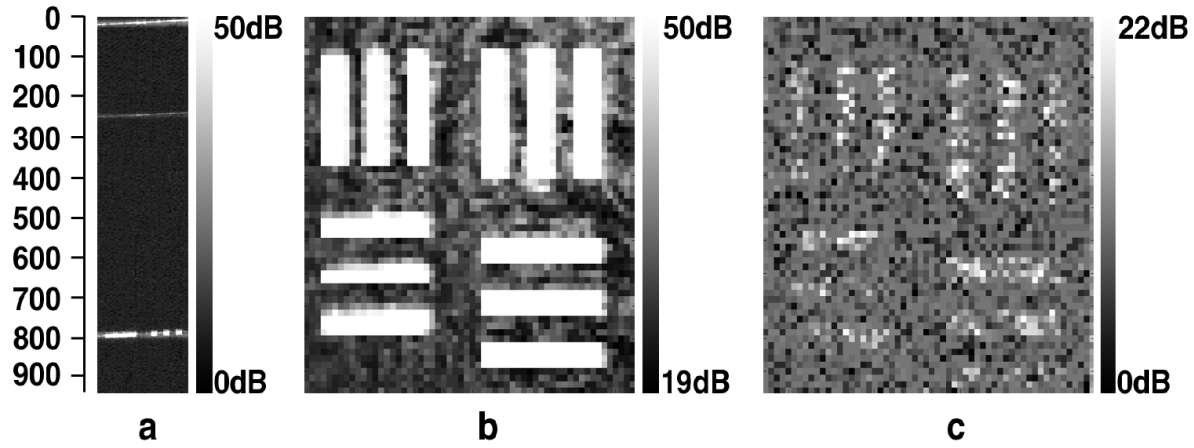


Figure 2.6: Longitudinal cross-section ( $260 \times 950 \mu\text{m}^2$ ) (a) and *en face* ( $260 \times 260 \mu\text{m}^2$ ) images of resolution target behind  $400 \mu\text{m}$  water (a and b) and intralipid solution  $\mu_s = 100 \text{ cm}^{-1}$  (c). The intensity scale corresponds to the SNR in dB. Depth scale on the left of (a) is in microns.

where  $\mu_s$  and  $t$  are the measured intralipid solution scattering coefficient and thickness respectively. Note that for the intralipid solution concentration and the wavelength employed,  $\mu_t \ll \mu_s$  [30, 31]. Therefore, we neglected  $\mu_a$  in the calculation of OD.

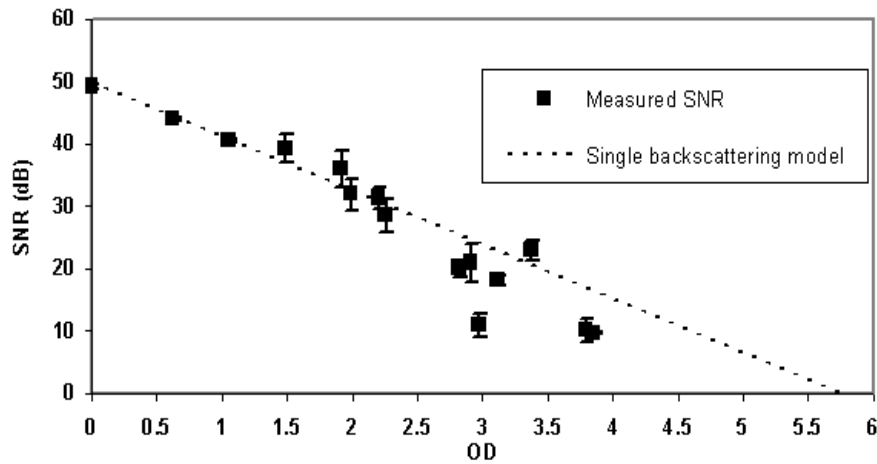


Figure 2.7: SNR (square dots) measured from a reflective bar of the USAF resolution target behind  $\approx 400 \mu\text{m}$  intralipid scattering solution as a function of the scattering solution optical depth (OD). The dashed line represents the OCT signal attenuation according to a single backscattering model.

According to an accepted model of OCT in scattering media [32–34], the greatest light contribution to OCT signals comes from single backscattered photons. Therefore, mainly photons that are not scattered in the round trip travel in the intralipid solution and are reflected by the USAF resolution target reflective elements contribute to the signal. To compare our measurements with this model we plotted (dashed line in Fig. 2.7) the theoretical SNR ( $SNR_{model}$ ) according to Beer's law attenuation as a function of optical



depth (OD):

$$SNR_{model} = 20 \log \left( \frac{2\sqrt{e^{-2\mu_s t} I_s I_r}}{\sigma_{noise}} \right) = SNR_{max} + 10 \log(e^{-2OD}) \quad (2.10)$$

where  $I_r$  and  $I_s$  are the coherent light power incident on the detector that are reflected by perfect mirrors in the reference and sample arms respectively.  $SNR_{max}$  is the maximum SNR, i.e. 50 dB (measured) in our case.

The measured SNR values for ODs up to 2.5 correspond well to the exponential decay given by the single scattering model, but for  $OD > 2.5$  significant differences are observed which could be explained by the following two sources of errors. First, for samples with  $OD > 2.5$ , the use of a CCD camera for longitudinal positioning of the USAF resolution target becomes impractical because the pattern is not distinguishable anymore through the turbid media. In those conditions the uncertainty on sample longitudinal positioning increases and the measured signals are lower than they would be if the USAF target was placed at the objective focal plane. Secondly, the scattering coefficient could be underestimated for samples with  $OD > 2.5$ . Indeed, when measuring  $\mu_s$  with the collimated light transmission method described in reference [30], very weak signals have to be measured for highly scattering samples. In this case, the signals might be overestimated due to system noise, which induces an underestimation of  $\mu$ .

Furthermore, for scattering samples greater than 2.5 OD, Yadlowski *et al.* [33] demonstrated that the single backscattering model fails to describe accurately the attenuation of OCT signals. At depths greater than 2.5 OD multiply scattered photons contribute significantly to OCT signals. In particular, when the scattering medium is composed of particles with diameters small compared to the wavelength, which is the case with intralipid solution (intralipid particles average diameter measured by van Staveren *et al.* [30] is 93 nm), multiply scattered photons induce a background haze and a loss of contrast. This could explain why we were not able to discern the reflective bars on the USAF resolution target beyond 4 OD, even though the single backscattering model indicates that the limit is approximately 5.7 OD (intercept of the  $SNR_{model}$  dashed line with 0 dB level in Fig.2.7). Another effect that could be responsible for the lower-than-expected signals is speckle. The situation can be compared to a random walk speckle model (the scattering medium) together with a constant phasor (the reference beam) [35]. The averaging of speckles might have reduced the measured signal.

Finally, the technique of parallel detection itself might be at the origin of the differences between observation and single backscattering model. By illuminating the whole sample field at once in contrast to point-by-point beam scanning there is the possibility for an optical cross-talk between pixels that could reduce contrast. Although each SPDA photodiode ( $35 \times 35 \mu m^2$ ) acts as a confocal pinhole, it cannot reject entirely out of focus light. The chance of detecting coherent photons backscattered from a site outside of the imaged voxel is increased by illuminating a large sample area instead of focusing the illumination beam on a single point. We intend to study this point in more detail in the future in order to draw conclusions about the advantages and disadvantages of parallel vs. point-by-point scanning OCT approaches.

### Images of onion cells

In Fig. 2.8 are presented longitudinal cross-sectional (Fig. 2.8a) and *en face* images (Fig. 2.8b/c) of an onion. Figures 2.8b and 2.8c are the images of cell layers at the surface and  $100 \mu m$  below the surface of the onion, respectively. The sample longitudinal position was adjusted to bring the images presented in Figures 2.8b and 2.8c into focus. Backscattered light is detected in the cross sectional image up to a depth of approximately  $450 \mu m$ . One clearly distinguishes cell boundaries in the *en face* images.

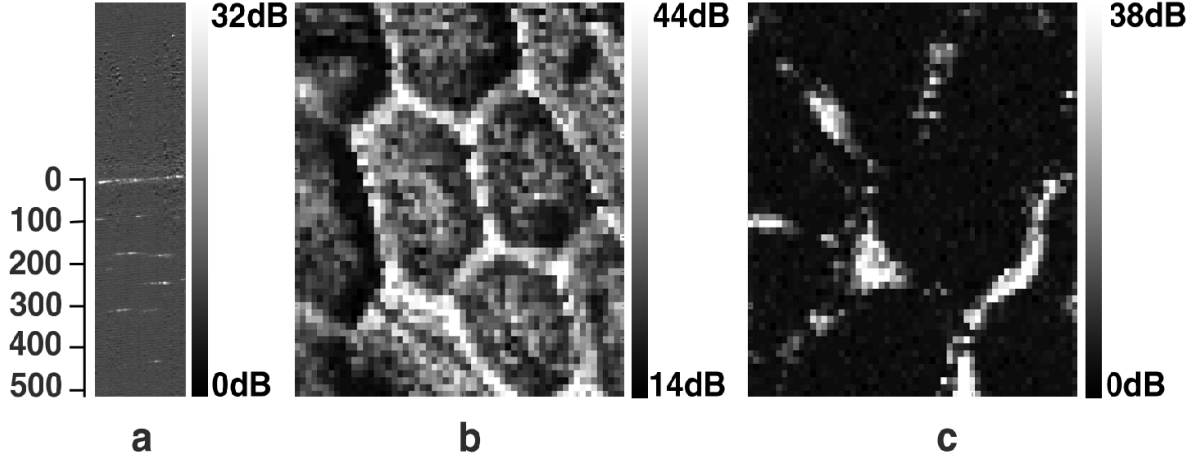


Figure 2.8: Longitudinal cross-section ( $260 \times 950 \mu\text{m}^2$ ) (a) and *en face* ( $260 \times 260 \mu\text{m}^2$ ) images of onion at a depth of  $\approx 0$  (b) and  $100 \mu\text{m}$  (c). The intensity scale corresponds to the SNR in dB. Depth scale on the left of (a) is in microns.

### 2.3.4 Conclusion and outlook

These results show the performances of our parallel OCT system using a SPDA for imaging scattering samples. To our knowledge it is the first demonstration of the use of CMOS smart pixel technology for parallel OCT in scattering phantoms and biological samples. Volumetric image acquisition is achieved at a relatively high speed ( $2.5 \times 10^6$  pixels/s) compared to OCT systems using transverse scanning mechanisms (up to  $2 \times 10^6$  pixels/s [36]). However, imaging depth penetration is currently limited by the SNR of the system (50 dB compared to 90 dB in [36]).

Furthermore, using a femtosecond light source combined with a microscopic imaging scheme, we obtained high longitudinal and transverse resolutions. However, transverse resolution depends strongly on the distance to the object focal plane. Further improvements of imaging performances rely on future developments of SPDAs (narrower CMOS electronic bandpass filter, higher pixel read-out rate and higher number of pixels) as well as a dynamic focusing mechanism to maintain transverse resolution throughout the entire depth scan.

## 2.4 Video-rate three-dimensional optical coherence tomography

(published in Optics Express Vol. 10, No. 96, 429-435, 6 May 2002)

M. Laubscher, M. Ducros, B. Karamata, T. Lasser and R. P. Salathé

Institute of Applied Optics, Swiss Federal Institute of Technology, CH-1015 Lausanne, Switzerland

### ABSTRACT

Most current optical coherence tomography systems provide two-dimensional cross-sectional or en face images. Successive adjacent images have to be acquired to reconstruct three-dimensional objects, which can be time consuming. Here we demonstrate three-dimensional optical coherence tomography (3D OCT) at video rate. A 58 by 58 smart-pixel detector array was employed. A sample volume of  $210 \times 210 \times 80 \mu\text{m}^3$  (corresponding to  $58 \times 58 \times 58$  voxels) was imaged at 25 Hz. The longitudinal and transverse resolutions are  $3 \mu\text{m}$  and  $9 \mu\text{m}$  respectively. The sensitivity of the system was 76 dB. Video rate 3D OCT is illustrated by movies of a strand of hair undergoing fast thermal damage.

### 2.4.1 Introduction

Over the past 15 years the biomedical imaging technique called optical coherence tomography (OCT) has experienced many technological improvements and found a host of useful applications [25, 26, 37]. The main aspects of development have been spatial resolution [38], sensitivity and acquisition speed [36, 39]. In addition, new implementations of OCT have been developed that provide additional information about the sample under study. For example, polarization-sensitive OCT allows the measurement of depth-resolved sample birefringence [40, 41] and Doppler OCT permits the assessment of flow velocity in biological samples [42]. However, acquiring two-dimensional OCT images is not sufficient to fully describe the three dimensional morphology of biological samples under study. For example, three-dimensional OCT images would be required to measure the depth and lateral extent of epithelial tumors in the skin, cervix or oral mucosa. A few research groups reported the reconstruction of three dimensional maps of reflectivity obtained by acquiring two-dimensional arrays of adjacent OCT A-scans, but such a procedure can be time consuming [43–45].

Besides the "classic" longitudinal OCT imaging technique based on A-scans, two classes of *en face* (transversal) OCT imaging techniques have been proposed: the "flying spot" and the "parallel OCT" techniques. Both can be used to acquire three-dimensional reflectivity maps. In the "flying spot" technique the probing light beam is scanned transversally in raster scans to acquire en face images at different depths [46, 47] whereas in the "parallel OCT" technique wide-field illumination and acquisition is used [12, 19, 27]. The detectors employed in the latter technique are photodetector arrays in contrast to all other OCT techniques which rely on single-unit detectors. The need for lateral scanning is in this case eliminated, to the advantage of higher acquisition rates.

Charge coupled device (CCD) cameras are the most commonly used imaging devices for parallel imaging schemes. However, CCD cameras suffer from two drawbacks when used in parallel OCT systems: (1) the high optical DC intensity reflected by the reference mirror reduces the dynamic range available for AC interferometric signal detection, (2) the CCD frame rate (typically 100 Hz for  $512 \times 512$  pixels) is much lower than the interferometric signal frequency (typically greater than 1 kHz). In this case a lock-in detection or synchronous illumination scheme has to be employed [12], which limits the image acquisition speed. A different photodetector array based on CMOS technology was specifically developed for parallel OCT [19, 29]. Besides transducing light signals into electrical signals, CMOS detectors offer the additional functionality of customized, integrated signal processing for each pixel. Optical coherence tomography with a parallel detection scheme using such one and two-dimensional

smart pixel detector arrays (SPDA) was previously demonstrated on reflective surfaces [19]. Recently, we have shown the feasibility of using a SPDA in scattering samples as well [48]. In the present work we use a SPDA to demonstrate for the first time to our knowledge 3D OCT imaging at video-rate.

## 2.4.2 Method

### Optical set-up

The optical set-up is illustrated in Figure 2.9. The light source employed is a compact femtosecond mode-locked Ti:Sapphire laser (MLTS) (FemtoLasers Inc., Vienna, Austria) with a nearly Gaussian spectrum centered at 800 nm and a full-width-at-half-maximum (FWHM) spectral bandwidth of 100 nm. Lenses L1 and L2 form a telescope to increase the beam diameter before it enters a free space Michelson interferometer. An average power of 430 mW is available at the interferometer input. A beamsplitter cube (BS) separates the light into the interferometer reference and sample arms. A variable neutral density filter wheel (F) is placed into the reference arm and a compensation glass plate (C) of equal thickness into the reference arm. Two identical microscope objectives (L4 and L5, 20x) are used to illuminate and collect reflected light from the sample (S) and reference mirror (RM). The incident average power on the sample is 120 mW. The illumination profile on the sample is approximately Gaussian and covers the square field of view of the detector of  $210 \times 210 \mu\text{m}^2$ . Light reflected from S and RM interferes only if the optical path lengths match to within the source coherence length. RM is translated longitudinally using a voice-coil scanning stage (Physik Instrumente (PI) GmbH & Co) that is driven by a triangular input function at a frequency of 12.5 Hz. The scan amplitude is  $80 \mu\text{m}$ , as measured by the voice coil stage encoder. Acquisition is performed both during the forward and backward half-period of the triangular scan, i.e. at 25 Hz. The sample is imaged by lens L6 onto a SPDA with  $58 \times 58$  pixels. Each pixel consists of a silicon photodiode coupled to a CMOS electronic circuit that amplifies and demodulates AC signals [19]. Each pixel output provides an analog voltage proportional to the envelope of the optical interference signal. The analog signals corresponding to each pixel are read out sequentially at a rate of 5 MHz, digitized by a 12-bit A/D card and displayed on a computer screen. Volumetric data sets with  $58 \times 58 \times 58$  pixels, corresponding to  $210 \times 210 \times 80 \mu\text{m}^3$  are thus acquired at a rate of 25 Hz.

### Sample

The sample was a strand of dark human hair on a microscope glass slide positioned at the focal plane of the microscope objective L4. The average irradiance incident on the sample is approximately  $173 \text{ W/cm}^2$ . Because of the high melanin concentration in the hair strand the illuminating laser beam is strongly absorbed. As the hair is only in contact with a glass plate and with the air, the heat transfer to the surrounding media is rather low and the accumulated thermal energy causes the hair to swell and to burn. Only because of the high absorption coefficient of the imaged sample do we observe an interaction between the probing laser beam and the sample. Indeed, we have observed light-colored hair and onions under identical conditions and no damage to the sample was observed. Even though the total power used for sample illumination is high (120 mW) the irradiance remains relatively low. Indeed, the employed average irradiance is inferior to irradiance reported in literature in point by point scanning OCT systems using femtosecond lasers [38]. Nevertheless, thermal effects, depending on irradiance, pulse length, exposition duration, tissue absorption coefficient and thermal properties, should be investigated for each specific sample.

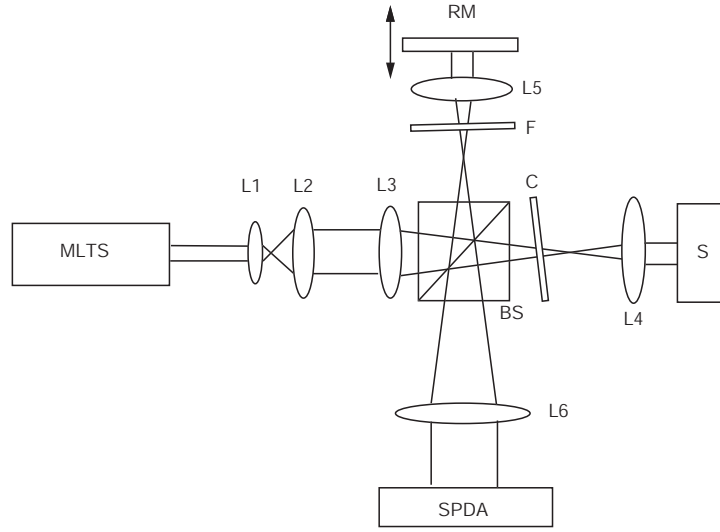


Figure 2.9: Parallel OCT optical setup schematic. The different elements are: mode-locked Ti:Sapphire femtosecond laser (MLTS); achromatic lenses (L1, L2, L3, and L6); non-polarizing achromatic beamsplitter cube (BS); identical achromatic microscope objectives 20X, 0.45 NA (L4 and L5); reference mirror (RM); variable neutral density filter wheel (F); compensation glass plate (C); 58 by 58 smart pixel detector array (SPDA) and sample (S).

### 2.4.3 Results

#### System performance

We measured the system longitudinal response on a mirror in air to be  $3 \mu\text{m}$  (FWHM), which is in good agreement with the theoretically expected value for a Gaussian spectrum of 100 nm bandwidth at a central wavelength of 800 nm. Transverse resolution in air was determined using a USAF resolution target at the focal plane of L4. Using the 20x objectives we could resolve reflective bars with a maximum spatial frequency of  $114 \text{ mm}^{-1}$ , corresponding to a transverse resolution of  $8.8 \mu\text{m}$ . The transverse resolution is limited by the NA of the microscope objectives (0.45) and the fill factor of the detector array (10%).

To measure the system sensitivity we imaged an air-water interface (2% power reflection) and varied the attenuation of the reference arm intensity by rotating the neutral density filter wheel F until the detector signal was maximized to a value that we call  $V_{2\%max}$ . The sensitivity S in decibel of the system is then given by

$$S = 20 \log \frac{V_{2\%max}}{\sigma} + 10 \log \frac{1}{0.02} \quad (2.11)$$

where  $\sigma$  is the electronic signal noise that is experimentally taken to be the standard deviation of all voxels values when no sample was present. The sensitivity was measured to be 76 dB. During all experiments on biological samples, such as the hair strand, the neutral density filter wheel stayed at the same position.

The advantages of using the method described above to measure the system sensitivity are three-fold: (1) The sample (water) mimics typical biological samples reflectivities; (2) The electronic AC gain of the SPDA detector depends on the level of optical DC illumination. The lower the DC illumination the higher the AC gain. Therefore, by decreasing the reference arm intensity the AC gain is increased more than the optical AC signal is attenuated and thus a higher electric output signal can be obtained; (3) By decreasing the optical DC illumination the noise decreases and approaches the shot noise limit.

The maximum SNR of an OCT system is reached when (1) the detection is shot noise limited and (2) the detection bandwidth matches the interferometric signal bandwidth [1, 2]. In the present experimental

conditions we calculated the optimum SNR to be 92 dB. However, the current implementation of the electronic filter integrated in each pixel ( $110 \times 110 \mu m^2$ ) of the SPDA does not allow a very fine filtering of the signal. We estimated the filtering bandwidth to about 40 kHz. The shot noise limited SNR of our setup is then 77.6 dB which is close to the measured SNR.

### Sample images

In the following we reproduce image data that has been acquired during a 1600 ms time interval at a rate of 25 volumes per second, i.e. a time sequence of 40 volumetric data sets with dimensions of  $58 \times 58 \times 58$  voxels each. The raw data is in the form of a one-dimensional array of  $58 \times 58 \times 58 \times 40$  16-bit integers from which we have reconstructed the following two and three-dimensional images.

Figure 2 shows a schematic of the imaged volume in relation to the sample and three tomographic images along the sample symmetry axes at the beginning of the time sequence. The image size format has been adjusted to represent the true geometric dimensions of  $210 \times 210 \mu m^2$  and  $210 \times 80 \mu m^2$ , respectively. All images are shown in inverted grayscale reflectivity coding. The *en face* image (center) shows the shadow caused by the hair at the height of the supporting glass plate. On the longitudinal cut (right top), taken parallel to and at the center of the hair strand, one distinguishes its upper and lower surfaces. The cross sectional cut (right bottom) exhibits the profile of the hair on the glass plate.

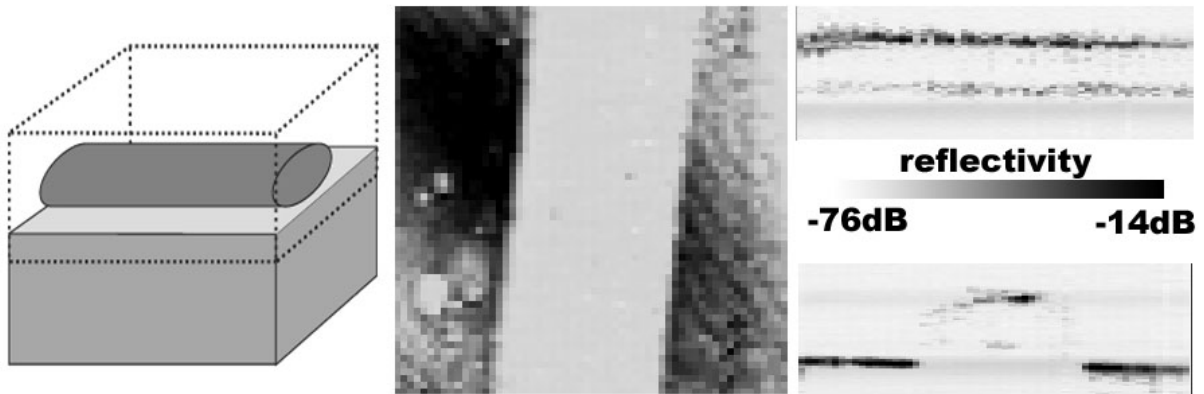


Figure 2.10: (left) Schematic of the imaged volume (dashed parallelepiped) in relation to the sample (hair strand on glass slide). (center) *En face* image ( $210 \times 210 \mu m^2$ ) at the height of the contact between hair and glass. (right top) Longitudinal cut ( $210 \times 80 \mu m^2$ ) parallel to and at the center of the hair. (right bottom) Cross-sectional cut ( $210 \times 80 \mu m^2$ ) perpendicular to the axis of the hair strand.

The reflectivity scale bar of Figure 2.10 also applies to all following tomographic images which we represent for simplicity in a square  $58 \times 58$  pixel image format. The series of images in figure 2.11 shows the temporal evolution of the sample in the three tomographic planes previously discussed. During the first 960 ms (24 time frames) no modification of the hair is visible. The incident laser radiation is highly absorbed and locally heats up the hair strand. At frame 25 (1000 ms after the beginning of irradiation) first modifications become noticeable in the longitudinal and cross-sectional cuts. We see locally some higher reflectivity signals from inside the hair volume, to the detriment of the signal corresponding to the lower side of the hair that starts to be shadowed by these new backscattering sites. On the *en face* image these changes are not yet visible, because the interaction between the laser and the hair has up to this moment not progressed far enough in depth to modify the hair's shadow on the glass plate. On the next frame (40 ms later) a burn crater in the center of the hair can clearly be distinguished on the longitudinal and cross-sectional cuts. Its depth can be estimated to approximately 45% of the hair's thickness. The formerly smooth surface of the hair becomes very fragmented and scattering in the area of the burn crater

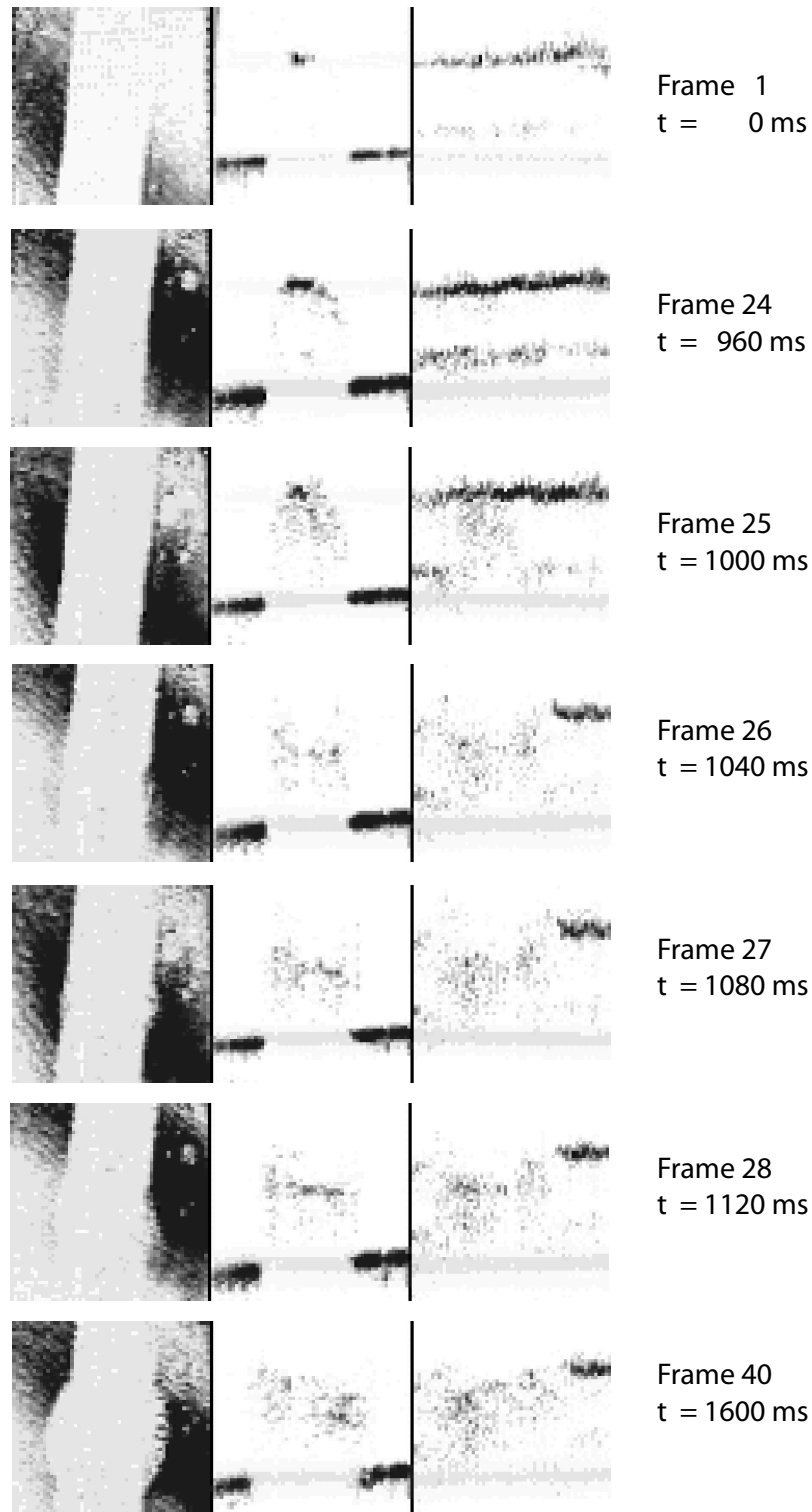


Figure 2.11: Tomographic images acquired during a 1600 ms time interval at a rate of 25 volumes per second (40 time frames). (left) *En face* image ( $210 \times 210 \mu\text{m}^2$ ) at the height of the contact between hair and glass. (center) Transversal cut ( $210 \times 80 \mu\text{m}^2$ ). (right) Longitudinal cut ( $210 \times 80 \mu\text{m}^2$ ) parallel to and at the center of the hair. Reflectivity grayscale as in Figure 2.10.

and the signals from the lower hair surface disappear because of shadowing. Reflectivity signals from above the former position of the hair appear and might be identified as debris. The localization of the laser-hair interaction to the center of the optical field is due to the Gaussian like spatial intensity profile of the probing laser beam. Note that the SPDA cannot compensate for non-uniform illumination since settings are common to all pixels. The area of interaction can be measured to be of a diameter of about 120-130  $\mu\text{m}$ . On the next frame (40 ms later) the hair's modifications become finally visible on the *en face* image. The hair starts to swell laterally into a bulb and continues doing so for the next 520 ms until the end of the acquisition. This bulb attains approximately 150% of the hair's original width. The swelling can of course be observed on the cross-sectional images as well. However, other than the lateral swelling no other major modifications are visible in this final phase of the interaction.

Because of an experimental problem of synchronization images of even and odd volumes are slightly shifted in relation to each other, which causes the image jumps on this image sequence. This imperfection can easily be corrected for and this has been done in Figure 2.12. Furthermore, the last column of photodetectors (rightmost column of pixels on an *en face* image) exhibits a markedly different response than the others, which causes image artifacts. This is due to a different electronic pixel layout that has been realized on the last column for experimental purposes. The distortions visible on adjacent columns in the beginning of the time sequence (clearly visible as trailing signals of the glass plate on the cross-sectional cuts) might be related.

Figure 2.11 illustrates three tomographic views that permit to visualize relatively well the dynamic phenomenon observed. However, much more data has been acquired with this 3D OCT method and any chosen view could be visualized. In order to allow an inspection of the entire volume at one glance we use the whole data set to generate a three-dimensionally rendered representation based on iso-surfaces. Each of the 40 time frames has been rendered as described in [49] and combined into the image series shown in Figure 2.12. This representation goes far beyond tomographic images and is very useful for localizing regions of particular interest.

#### 2.4.4 Conclusion

In conclusion, we have implemented a parallel OCT system capable of 3D data acquisition at video-rate. The key element of the system is a smart pixel detector array, conceived and developed specifically for *en face* OCT imaging. Combined with a femtosecond light source and a microscopic imaging scheme this system allows for both high longitudinal and transverse resolutions when limited to a small sample volume. We have illustrated its performance by imaging the time-resolved thermal damage of a strand of dark human hair under the influence of the probing laser beam. Besides tomographic images we have also shown a three-dimensionally rendered image sequence.



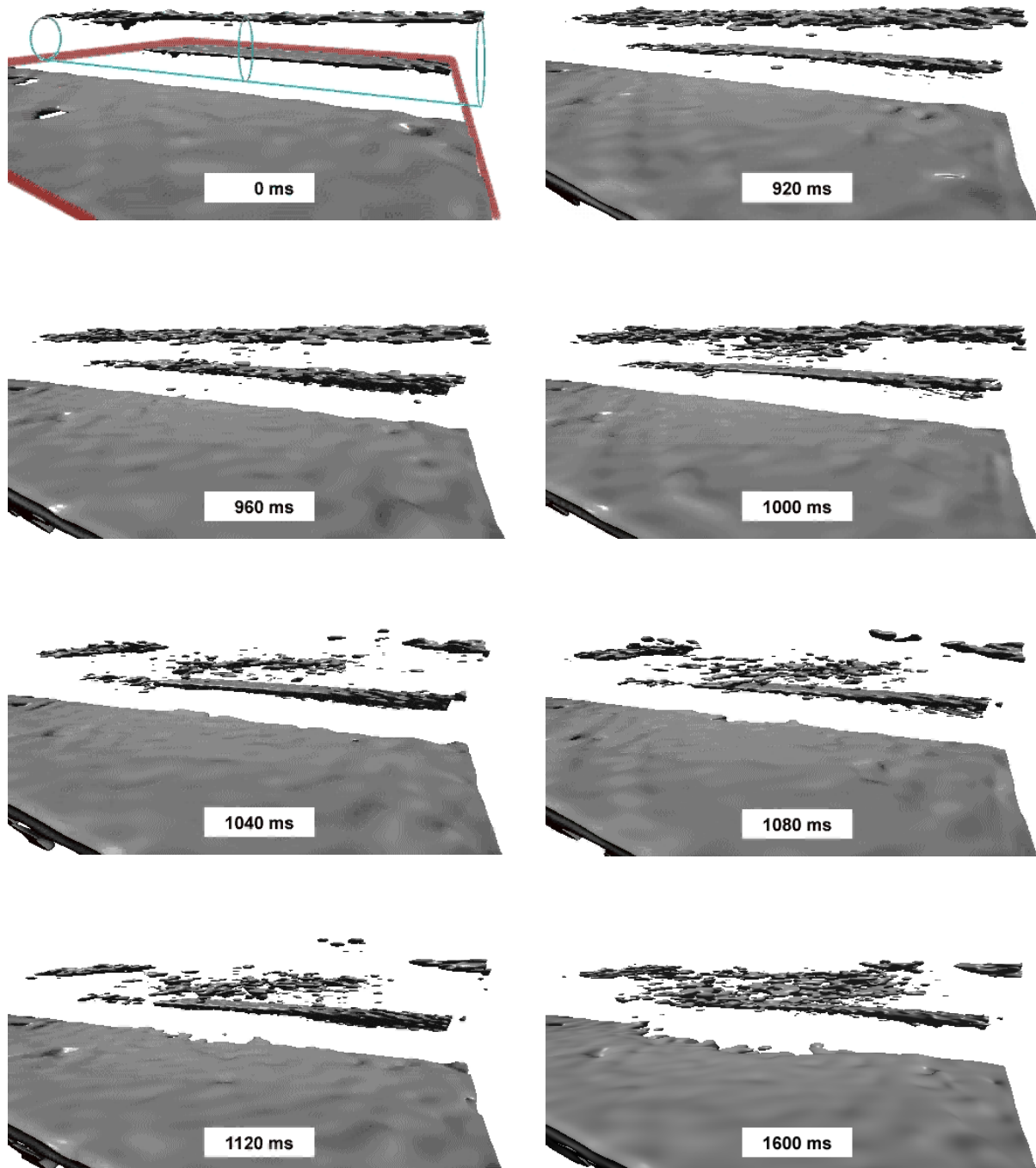


Figure 2.12: 3D rendering of the sample based on iso-surfaces. To facilitate the comprehension of this particular perspective we indicate the situation of the hair and the glass slide by the lines in the first frame.

## 2.5 Conclusion

The goal of this work on parallel detection using the SPDA has been to extend the detector's application from reflective surface measurements to volumetric measurements in scattering media and to elucidate its limitations. The feasibility of realizing parallel OCT imaging with such a device in scattering samples has been shown. Three-dimensional OCT acquisitions of reflective surfaces hidden by a scattering solution and images of onion have been presented. Furthermore, high speed imaging, allowing for video-rate, three-dimensional OCT could be demonstrated. The thermal deformations of a human hair under laser irradiation have been imaged at 25 volume acquisitions per second. By employing a high power femtosecond laser source together with the SPDA, a sensitivity of 76 dB could be achieved.

The principal limitation of parallel OCT in scattering media is the generation of optical cross-talk. This question has not been addressed here, but has been studied in depth by Karamata [9]. The limitation of the CMOS detector array itself is mainly its low sensitivity. Even with the power delivered by a mode-locked Ti:Sa laser, the sensitivity did not exceed 76 dB, whereas at least 90-100 dB would be needed for competitive imaging in scattering tissues. Furthermore, the low number of  $58 \times 58$  pixels and the maximum readout rate of 5 Msamples/s are not satisfactory for fast, high-resolution imaging. Finally, the current device suffers from sample dependant working parameters, stability problems and difficult and frequent re-calibration.

However, dedicated detectors for parallel OCT are still in their infancy and the prototype used in this work is the first of its kind. New improved detectors have been developed in the meantime and are currently under test [50]. Due to a novel circuit approach and sensor architecture, they are more power-efficient, permitting the integration of more pixels, more robust to drifts in operational conditions, requiring less re-calibrations and are also faster. Furthermore, the newer devices provide additional information on the optical signal, such as offset level and temporal phase.

## 2.6 References

- [1] J. A. Izatt, M. R. Hee, G. M. Owen, E. A. Swanson, and J. G. Fujimoto. Optical coherence microscopy in scattering media. *Optics Letters*, 19(8):590–2, 1994.
- [2] E. A. Swanson, D. Huang, M. R. Hee, J. G. Fujimoto, C. P. Lin, and C. A. Puliafito. High-speed optical coherence domain reflectometry. *Optics Letters*, 17(2):151–3, 1992.
- [3] W. V. Sorin and D. M. Baney. A simple intensity noise reduction technique for optical low-coherence reflectometry. *IEEE Photonics Technology Letters*, 4:1404–1406, 1992.
- [4] A. Dubois, L. Vabre, A. C. Boccara, and E. Beaurepaire. High-resolution full-field optical coherence tomography with a linnik microscope. *Applied Optics*, 41(4):805–812, 2002.
- [5] L. Vabre, A. Dubois, and A. C. Boccara. Thermal-light full-field optical coherence tomography. *Optics Letters*, 27(7):530–532, 2002.
- [6] A. F. Fercher, C. K. Hitzenberger, M. Sticker, E. Moreno Barriuso, R. Leitgeb, W. Drexler, and H. Sattmann. A thermal light source technique for optical coherence tomography. *Optics Communications*, 185:57–64, 2000.
- [7] B. Karamata, P. Lamblet, M. Laubscher, and T. Lasser. Spatially incoherent illumination as a mechanism for cross-talk suppression in wide-field optical coherence tomography. *Optics Letters*, 29:736–738, 2004.
- [8] B. Karamata, P. Lamblet, M. Laubscher, and T. Lasser. Multiple scattering in Optical Coherence Tomography. *submitted to JOSA A*, 2004.
- [9] B. Karamata. *On spatial coherence and multiple scattering in wide-field OCT (in preparation)*. PhD thesis, Swiss Federal Institute of Technology, 2004.
- [10] J. E. Greivenkamp and J. H. Bruning. Phase shifting interferometry. In D. Malacara, editor, *Optical shop testing*, pages 501–598. John Wiley and Sons, 1992.
- [11] A. C. Boccara, F. Charbonnier, D. Fournier, and P. Gleyzes. Procédé et dispositif de détection synchrone multicanal. *French patent FR90.092255 and international extensions*, 1990.
- [12] E. Beaurepaire, A. C. Boccara, M. Lebec, L. Blanchot, and H. Saint-Jalmes. Full-field optical coherence microscopy. *Optics Letters*, 23(4):244–246, 1998.
- [13] M. Akiba, K. P. Chan, and N. Tanno. Real-time, micrometer depth-resolved imaging by low-coherence reflectometry and a two-dimensional heterodyne detection technique. *Japanese Journal of Applied Physics*, 39:1194, 2000.
- [14] M. Akiba, K. P. Chan, and N. Tanno. Full-field optical coherence tomography by two-dimensional heterodyne detection with a pair of ccd cameras. *Optics Letters*, 28(10):816–818, 2003.
- [15] A. F. Fercher, R. Leitgeb, C. K. Hitzenberger, and H. Sattmann. Complex Spectral Interferometry OCT. *Proc. SPIE*, 3564:173–178, 1999.
- [16] E. Bordenave, E. Abraham, G. Jonusauskas, N. Tsurumachi, J. Oberle, C. Rulliere, P. E. Minot, M. Lassegues, and J. E. S. Bazeille. Wide-field optical coherence tomography: imaging of biological tissues. *Applied Optics*, 41(10):2059–2064, 2002.

- [17] E. Bordenave, E. Abraham, G. Jortusauskas, J. Oberle, and C. Rulliere. Longitudinal imaging in biological tissues with a single-shot correlation system. *Optics Express*, 10(1):35–40, 2002.
- [18] C. Dunsby, Y. Gu, and P. M. W. French. Single-shot phase-stepped wide-field coherence-gated imaging. *Optics Express*, 11(2):105–115, 2003.
- [19] S. Bourquin, P. Seitz, and R. P. Salathé. Optical coherence topography based on a two-dimensional smart detector array. *Optics Letters*, 26(8):512–514, 2001.
- [20] S. Bourquin, P. Seitz, and R. P. Salathé. Two dimensional smart detector array for interferometric applications. *Electronic Letters*, 37:975–976, 2001.
- [21] S. Bourquin. *Low-coherence interferometry based on customized detector arrays, no. 2171*. PhD thesis, Swiss Federal Institute of Technology, 2000.
- [22] S. Bourquin, R. P. Prasankumar, F. X. Kärtner, J. G. Fujimoto, T. Lasser, and R. P. Salathé. High-speed femtosecond pump probe spectroscopy with a smart pixel detector array. *Optics Letters*, 28(17):1588–1590, 2003.
- [23] J. Mitic, T. Anhut, M. Meier, M. Ducros, A. Serov, and T. Lasser. Optical sectioning in wide-field microscopy obtained by dynamic structured light illumination and detection based on a smart pixel detector array. *Optics Letters*, 28(9):698–700, 2003.
- [24] D. Huang, E. A. Swanson, C. P. Lin, J. S. Schuman, W. G. Stinson, W. Chang, M. R. Hee, T. Flotte, K. Gregory, C. A. Pufalito, and J. G. Fujimoto. Optical coherence tomography. *Science*, 254:1178–1181, 1991.
- [25] A. F. Fercher. Optical coherence tomography. *Journal of Biomedical Optics*, 1(2), 1996.
- [26] J. M. Schmitt. Optical Coherence Tomography (OCT): A Review. *IEEE Journal of selected topics in quantum electronics*, 5(4):1205–1215, 1999.
- [27] A. Knüttel, J. M. Schmitt, and J. R. Knutson. Low-coherence reflectometry for stationary lateral and depth profiling with acousto-optic deflectors and a ccd camera. *Optics Letters*, 19(4):302–304, 1994.
- [28] G. Häusler and M. W. Lindner. "coherence radar" and "spectral radar" - new tools for dermatological diagnosis. *Journal of Biomedical Optics*, 3(1):21–31, 1998.
- [29] S. Bourquin, V. Monterosso, P. Seitz, and R. P. Salathé. Video rate optical low-coherence reflectometry based on a linear smart detector array. *Optics Letters*, 25(2):102–104, 2000.
- [30] H. J. van Staveren, C. J. M. Moes, J. van Marle, S. A. Prahl, and M. J. C. van Gemert. Light scattering in intralipid-10400-1100nm. *Applied Optics*, 30(31):4507–4514, 1991.
- [31] S. T. Flock, S. L. Jacques, B. C. Wilson, W. M. Star, and M. J. C. van Gemert. The optical properties of intralipid: A phantom medium for light propagation studies. *Lasers in Surgery and Medicine*, 12:510–519, 1992.
- [32] J. M. Schmitt, A. Knüttel, and R. F. Bonner. Measurement of optical properties of biological tissues by low-coherence reflectometry. *Applied Optics*, 32(30):6032–6042, 1993.
- [33] M. J. Yadlowsky, J. M. Schmitt, and R. F. Bonner. Multiple scattering in optical coherence microscopy. *Applied Optics*, 34(25):5699–5707, 1995.

- [34] D. J. Smithies, T. Lindmo, Z. Chen, J. S. Nelson, and T. E. Milner. Signal attenuation and localization in optical coherence tomography. *Physics in Medicine and Biology*, 43(10):3025–3044, 1998.
- [35] J. W. Goodman. Statistical properties of laser speckle patterns. In J. C. Dainty, editor, *Laser Speckle and Related Phenomena*, volume 9 of *Topics in Applied Physics*. Springer, Berlin, 1975.
- [36] A. M. Rollins, M. D. Kulkarni, S. Yazdanfar, R. Ung-arunyawee, and J. A. Izatt. *In vivo* video rate optical coherence tomography. *Optics Express*, 3(6):219–229, 1998.
- [37] M. E. Brezinski and J. G. Fujimoto. Optical coherence tomography: high-resolution imaging in nontransparent tissue. In *IEEE Journal of Selected Topics in Quantum Electronics*, pages 1185–92. vol.5 no.4, 1999.
- [38] W. Drexler, U. Morgner, F. X. Kartner, C. Pitris, S. A. Boppart, X. D. Li, E. P. Ippen, and J. G. Fujimoto. *In vivo* ultrahigh-resolution optical coherence tomography. *Optics Letters*, 24:1221–3, 1999.
- [39] J. Szydlo, N. Delachenal, R. Gianotti, R. Walti, H. Bleuler, and R. P. Salathé. Air-turbine driven optical low-coherence reflectometry at 28.6-kHz scan repetition rate. *Optics Communications*, 154(1-3):1–4, 1998.
- [40] M. J. Everett, K. Schoenenberger, B. W. Colston, and L. B. Da Silva. Birefringence characterization of biological tissue by use of optical coherence tomography. *Optics Letters*, 23(3):228–230, 1998.
- [41] J. F. deBoer, T. E. Milner, M. J. C. vanGemert, and J. S. Nelson. Two-dimensional birefringence imaging in biological tissue by polarization-sensitive optical coherence tomography. *Optics Letters*, 22(12):934–936, 1997.
- [42] X. J. Wang, T. E. Milner, and J. S. Nelson. Characterization of fluid-flow velocity by optical Doppler tomography. *Optics Letters*, 20(11):1337–1339, 1995.
- [43] J. K. Barton, J. A. Izatt, M. D. Kulkarni, S. Yazdanfar, and A. J. Welch. Three-dimensional reconstruction of blood vessels from *in vivo* color Doppler optical coherence tomography images. *Dermatology*, 198(4):355–361, 1999.
- [44] Y. Pan and D. Farkas. Non-invasive imaging of living human skin with dual-wavelength optical coherence tomography in two and three dimensions. *Journal of Biomedical Optics*, 3:446–455, 1998.
- [45] J. M. Herrmann, M. E. Brezinski, B. E. Bouma, S. A. Boppart, C. Pitris, J. F. Southern, and J. G. Fujimoto. Two- and three-dimensional high-resolution imaging of the human oviduct with optical coherence tomography. *Fertility and Sterility*, 70(1):155–158, 1998.
- [46] A. G. Podoleanu, J. A. Rogers, and D. A. Jackson. Three dimensional OCT images from retina and skin. *Optics Express*, 7(9):292–298, 2000.
- [47] B. M. Hoeling, A. D. Fernandez, R. C. Haskell, E. Huang, W. R. Myers, D. C. Petersen, S. E. Ungersma, R. Y. Wang, M. E. Williams, and S. E. Fraser. An optical coherence microscope for 3-dimensional imaging in developmental biology. *Optics Express*, 6(7):136–146, 2000.
- [48] M. Ducros, M. Laubscher, B. Karamata, S. Bourquin, T. Lasser, and R. P. Salathé. Parallel optical coherence tomography in scattering samples using a two-dimensional smart-pixel detector array. *Optics Communications*, 202(1-3):29–35, 2002.

- [49] P. Thevenaz and M. Unser. High-quality isosurface rendering with exact gradient. *Proceedings of the 2001 IEEE International Conference on Image Processing (ICIP'01)*, vol. I:854–857, 2001.
- [50] S. Beer, S. Waldis, and P. Seitz. Video-rate optical coherence tomography imaging with smart pixels. *Proc. SPIE*, 5140:69–76, 2003.

## Chapter 3

# Wavelength de-multiplexing

Wavelength de-multiplexing is an experimental method that permits online spectroscopic OCT by using the smart pixel detector array (SPDA) described in the previous chapter in a new way. Instead of acquiring signals from different spatial positions in parallel, now different spectral channels are associated to different detector elements. The question addressed in this chapter is how this experimental approach compares to the currently employed methods for spectroscopic OCT. In the first section the latter ones are described, notably the joint time-frequency analysis method and the multiple source approach. Then the concept of wavelength de-multiplexing is introduced and the experimental results obtained with this method for the absorption measurement of a glass filter plate are discussed. In section 3.2 a comparison between the de-multiplexing and time-frequency analysis approaches is presented, based on absorption measurements realized on a Nd-doped crystal. During these initial experiments, the SPDA has been substituted with a photodiode, requiring multiple measurements while translating the single detector in order to gain experience with the experimental approach. In section 3.3, the SPDA is finally introduced into the de-multiplexing setup in a proof-of-principle experiment of online spectroscopic OCT. The dynamically changing, spatially resolved absorption of a dye diffusing in a solvent-filled volume is measured on a single A-scan without post-processing. Section 3.4 is dedicated to the description of a further extension of this spectroscopic approach to multi-resolution imaging, a concept that has so far not been tested experimentally due to lack of time.

### 3.1 Methods for spectroscopic OCT

#### 3.1.1 Joint time-frequency analysis

Today's method of choice for spectroscopic OCT is the joint time-frequency analysis (JTFA) of either a time domain OCT [1] or a Fourier domain OCT measurement [2]. In many areas of science and engineering it has been found that the nature of time-varying signals is more easily recognized in the joint time-frequency domain than in either the time or the frequency domain alone. Whereas the evolution of the signal's amplitude is most easily represented in the time domain and the signal's frequency signature most conveniently seen in the frequency domain, it is only in the joint time-frequency representation that the temporal evolution of the signal's frequency content can be visualized directly. JTFA maps a one-dimensional time or frequency domain signal into a two-dimensional representation of energy versus time and frequency. A number of different mathematical transforms are known for achieving this, the most commonly used ones being windowed Fourier transforms and wavelet transforms. For a detailed discussion of the mathematical underpinnings of JTFA, see the excellent book of Qian and Chen [3].

In the case of OCT it is on the basis of the Wiener-Khinchin theorem that the frequency domain of the measurement corresponds to the optical spectrum of the interferometer light. More precisely, the

theorem states that the temporal coherence function  $G(\tau)$  and the power spectral density  $S(\nu)$  form a Fourier transform pair (see [4], section 10.1B)

$$S(\nu) = \int_{-\infty}^{\infty} G(\tau) \exp(i2\pi\nu\tau) d\tau \quad (3.1)$$

In Fourier-domain OCT the power spectral density  $S(\nu)$  of the cross-correlation field is measured directly and then Fourier-transformed as a whole in order to obtain a time-resolved, i.e. geometrical, representation. In time-domain OCT it is  $G(\tau)$  that is measured as part of the interference signal

$$I(\tau) = I_1 + I_2 + 2\sqrt{I_1 I_2} \text{Re}\{G_{12}(\tau)\} \quad (3.2)$$

where  $I(\tau)$  is the intensity of the interference signal as a function of the mutual time delay  $\tau$  of the two interfering fields with intensities  $I_1$  and  $I_2$ . By calculating piecewise, shifted Fourier transformations of either signal, a joint time-frequency analysis is realized that results in the before-mentioned two-dimensional representation of energy versus time (i.e. depth coordinate) and frequency (i.e. spectral coordinate).

An important limitation in all spectroscopic OCT methods is the impossibility of obtaining both a high axial resolution and a high spectral resolution of a measurement at the same time. A Fourier uncertainty relation exists between spectral bandwidth  $\Delta\nu$  and the coherence time  $\Delta\tau$  that reads

$$\Delta\nu \cdot \Delta\tau \geq k \quad (3.3)$$

The factor  $k$  is on the order of unity and depends on the shape of the power spectral density, respectively the Fourier-related coherence function. The strict equality holds only for widths that are Fourier-limited, i.e. without dispersion. The corresponding axial resolution  $\Delta z$  is then given by

$$\Delta z = \frac{l_c}{2} = \frac{\Delta\tau \cdot c}{2} \quad (3.4)$$

$$\Delta z \geq \frac{k}{2} \frac{c}{\Delta\nu} = \frac{k}{2} \frac{\lambda^2}{\Delta\lambda} \quad (3.5)$$

where  $l_c$  is the coherence length and  $c$  the speed of light. A detailed discussion on the estimation of axial resolution in OCT can be found in [5]. The spectral resolution is limited to  $2\Delta\lambda$  due to the Nyquist sampling theorem. Concerning the numerical values of  $k$  for different functional shapes, there exists some confusion in the literature. Authors from the domain of short pulsed laser physics (notably [6] and [7]) consistently cite values that are half of those found in math books [8]. This is presumably due to the fact that the laser pulse durations are generally measured with auto-correlators and that the double pass in those interferometric setups is not taken into account by convention. However, notably for a rectangular function and the corresponding sinc-function, the cited values in [6, 7] are not consistent. In one case they are given for the width of squared functions, in the other for non-squared functions, whereas both books use non-squared functions in the case of Gaussians. The table below lists the  $k$ -values for the three functional shapes of interest in this thesis, namely a Gaussian, a rectangle and a Hanning window, as verified by numerical simulation. The full width half maximum (FWHM) values of  $\Delta\nu$  and  $\Delta\tau$  are used.

In the particular case of JTFA, this means that choosing small Fourier windows or wavelet bases in either measurement domain in order to increase the resolution in one dimension, results in a deteriorated resolution in the conjugated dimension. Thus, for gaining the additional information sought after with a JTFA, a loss in resolution of the originally acquired signal has to be accepted. As an example consider figure 3.1, showing the measurement of a glass plate interface originally acquired in time-domain OCT



<i>function</i>	<i>k</i>
<i>Gaussian</i>	0.882
<i>rect</i>	1.207
<i>Hanning</i>	1.003

Table 3.1: Values of  $k$  for different functions

and then transformed using a JTFA with varying window sizes. Either the finer spectral features of the used light source are resolved with a large temporal window, or the spatial resolution is optimized with a large spectral window. Both resolutions can not be optimized simultaneously.

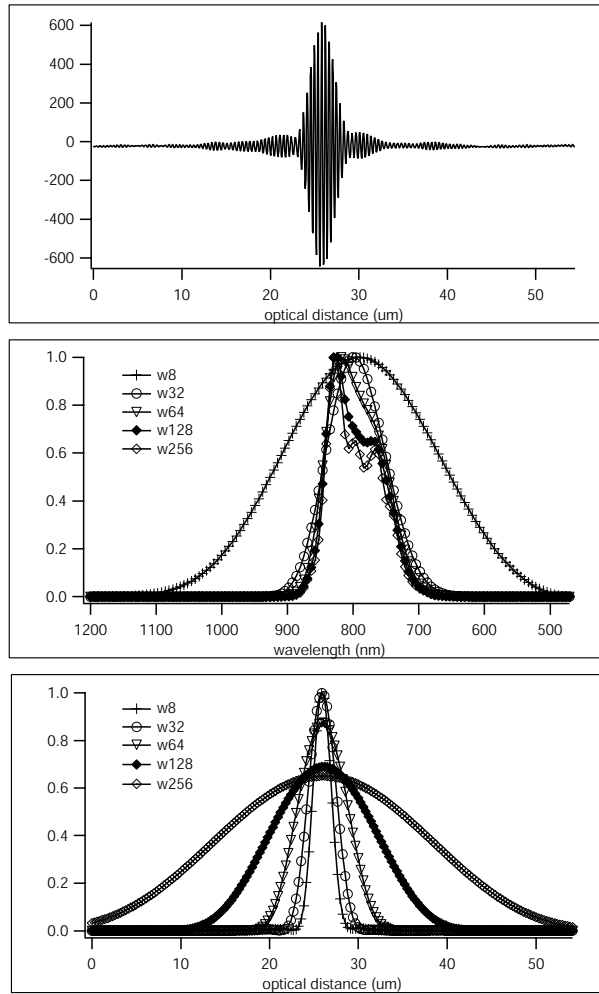


Figure 3.1: (top) Original time-domain OCT measurement of an air-glass interface, with a sampling of 28 points per  $\mu\text{m}$ . (middle) Cuts along the spectral coordinate of a JTFA with varying window sizes ( $wX$  corresponds to a window length of  $X$  sample points). (bottom) Cuts along the depth coordinate of the same JTFA.

However, being a post-processing method, JTFA offers the advantage of complete liberty over the choice between axial and spectral resolutions, even permitting the calculation of many different resolutions depending on the requirements dictated by the sample. No particular experimental conditions are imposed by the method, making it possible to treat previously acquired, fringe-resolved measurements

for spectroscopic information that at the time of acquisition were not intended to be analysed in this manner. However, the mapping of a time or Fourier-domain signal into the joint time-frequency domain is computationally intensive, currently still prohibiting the real-time use of JTFA in OCT.

### 3.1.2 Multiple source approach

A conceptually much simpler approach for gaining depth-resolved spectroscopic information is to use various light sources with different central wavelengths and realize multiple OCT measurements of the same sample region. Schmitt *et al.* [9] have demonstrated that by cleverly choosing the central wavelengths of only two sources, important additional information can already be gained from a sample by differential absorption measurements. They used two light-emitting diodes, one emitting in a vibrational absorption band of a targeted chemical compound (water, in this case) and the other emitting just outside this band. By comparing the OCT signals acquired with both sources they could clearly distinguish between lipid and water inclusions in a scattering material.

The difficulty of extending this concept to more sources is twofold. First, suitable low coherent light sources that cover piecewise a large spectral region are commercially difficult to find. Second, coupling many independent light sources together and ensuring that they illuminate the exact same sample region becomes experimentally very challenging.

### 3.1.3 Wavelength de-multiplexing

A natural extension of the multiple source approach is to illuminate the sample with only one large bandwidth source and separate its spectrum into multiple virtual sources afterwards. With the increased demand for higher axial resolutions in OCT, sources with ever larger bandwidths have been introduced into the field, such as femtosecond lasers, supercontinuum sources and white light sources. Instead of using them for high axial resolution, they can also be considered as a large spectral pool for multiple wavelength measurements with less axial resolution, but additional spectral information. The wavelength separation is advantageously realized in the detection arm of a time-domain OCT setup using either a prism or a grating. The so-created wavelength channels are detected independently using a detector array and treated as time-domain OCT signals of different central wavelengths. The method corresponds to an experimental joint time-frequency analysis and lies between time and Fourier-domain OCT.

This concept was first published for OCT by Watanabe *et al.* in 1999 [10, 11] and called dispersive coherence spectrotomography, because they were using a dispersive prism for separating the light into different wavelength channels in the interferometer detection arm. We rather choose to call this approach wavelength de-multiplexing, because it corresponds to measuring many wavelength-multiplexed OCT signals or rather de-multiplexed ones, as the wavelength separation takes place after the interaction between the light and the sample. Watanabe's work was not cited in any other article on spectroscopic OCT and we discovered it only after having independently come up with and tried out the same idea. In the following, some experimental results obtained with the wavelength de-multiplexing method are shown in order to illustrate the concept.

#### Absorption measurements on a glass filter plate

For a first test of this concept, the basic experimental set-up shown in figure 3.2 has been used. A free-space Michelson interferometer is illuminated with a mode-locked Titanium:Sapphire femtosecond laser of 90 nm bandwidth, centered at 800 nm. The incident beam is split into a reference and a sample beam of equal intensity by a beam splitter cube. In the reference arm a mirror is mounted on a motorized translation stage that permits to change the optical length of the arm with a nearly constant velocity. The reflected light from both reference and sample arms is recombined in the detection arm by the beam

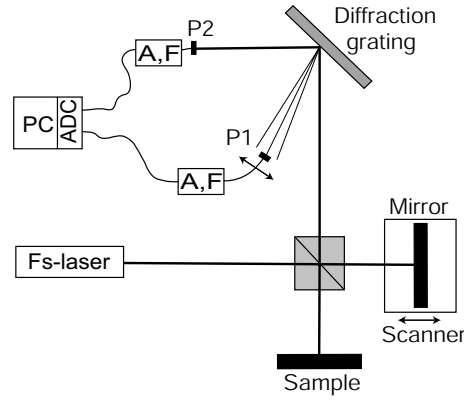


Figure 3.2: Optical setup schematic for wavelength de-multiplexing in a free-space Michelson interferometer. Principal elements are fs-laser as light source, voice coil scanner for depth scanning, diffraction grating for wavelength separation, photodiodes P1 and P2 for the detection of the zero and first diffraction order signals, A amplifier, F bandpass filter and ADC/PC analog-to-digital converter and personal computer.

splitter cube. The combined beam is diffracted by a holographic diffraction grating (1200 lines/mm) and thus split into the different wavelength channels in the first diffraction order. The photodiode P1 integrates the diffracted light over a certain bandwidth, depending on the solid angle seen by P1 and the diffractive power of the grating. By changing the lateral position of P1 by an amount corresponding to its width, the different channels are sampled sequentially. In these experiments 60 channels were sampled. Using a photodiode array, one can acquire the whole spectrum with one single depth scan, but for the sake of simplicity the former option has been chosen in this first experiment. The spectrally unchanged zero diffraction order is used to obtain the high depth resolution signal which is detected by a second photodiode P2. The electronic signals delivered by the photodiodes are preamplified using low-noise preamplifiers and digitized and acquired using a PC acquisition card. Envelop detection of the interferometric signal is performed by numerical filtering using LabView. As samples were used a BK7 glass plate (thickness 1 mm) and a Schott glass filter plate RG780 (optical highpass filter centered at 780 nm, thickness 2 mm).

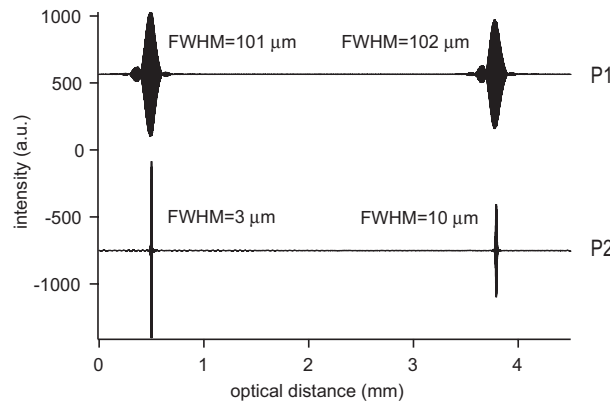


Figure 3.3: Interferometric signals as seen by photodiodes P1 (top) and P2 (bottom) for the glass filter plate.

The effective spectral bandwidth  $\Delta\lambda$  seen by P1 is 4.3 nm, as calculated from the angular diffraction of the grating and the solid angle subtended by the photodiode. The spatial extension of the light beam is negligible compared to the geometrical size of the photodiode. Applying equation 3.4 and assuming

a rectangular spectral window due to the rectangular geometry of P1 for the measurement in the first diffraction order and a Gaussian spectrum for the signal in the zero order, one predicts optimal axial resolutions of  $3\ \mu\text{m}$  for channel P2 and  $90\ \mu\text{m}$  for channel P1.

Figure 3.3 shows the interferometric signals acquired from the glass filter plate in the first and zeroth diffraction orders. The axial resolutions, measured as the FWHM value of the signals that correspond to the air-glass interface, are  $3\ \mu\text{m}$  and  $101\ \mu\text{m}$  in the high resolution and in the spectral channel, respectively. These widths increase for the rear surface of the plate due to a reduction in spectral bandwidth caused by the filter and due to dispersion. The measured FWHM values for the second interface are  $10\ \mu\text{m}$  and  $102\ \mu\text{m}$ , respectively. The signals in the spectral channel exhibit marked sidelobes that are due to rectangular spectral windowing.

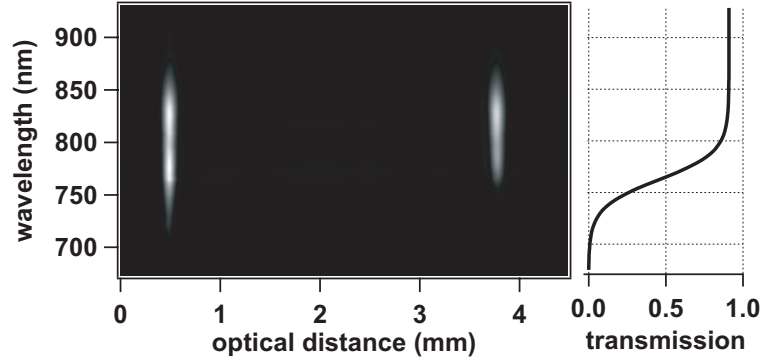


Figure 3.4: Spectroscopic OCT result for filter RG780 (left) and its transmission curve (right).

In Figure 3.4 the result of the complete spectroscopic OCT measurement obtained with the RG780 filter as sample is shown. The horizontal axis indicates the spatial coordinate and the vertical axis the spectral coordinate. Intensity is coded in linear grayscale. Each spectral coordinate corresponds to the signal envelope of one wavelength channel. One clearly distinguishes the front and rear surfaces of the filter plate and the change in the back reflected spectrum. The transmission characteristic of the filter is indicated to the right of figure 3.4.

The spectra as measured from the front and rear surfaces of the filter plate and the BK7 plate are depicted in detail in figure 3.5. These spectra are not corrected for the spectral response of the photodiode, as our interest lies in relative spectral changes. However, it has been verified that the spectra reflected from the front surfaces correspond to that of the femtosecond laser source. Intensities are normalized to their peak values for the front surfaces and an attenuation factor is calculated and applied for the rear surfaces. In the case of BK7 this factor takes into account the losses due to multiple reflections, i.e.  $(1 - R)^2$ , where  $R$  is the intensity reflectivity of the air-glass interface. In the case of the filter plate, additionally, the known filter attenuation at one wavelength is used to calibrate the peak intensity of the rear surface.

For the BK7 glass plate the back reflected spectra of the front and rear surfaces are identical as expected. For the RG780 filter we compare the measured spectrum of the rear surface with the theoretical expectation given by

$$S_{rear}(\lambda) = S_{front}(\lambda) \cdot T^2(\lambda) \cdot (1 - R)^2 \quad (3.6)$$

where  $T(\lambda)$  is the known intensity transmission function of the filter, see figure 3.6. The measured and the calculated spectra are found to be nearly identical, as can be seen in figure 3.5.

In conclusion, these preliminary experiments illustrate that the wavelength de-multiplexing method is capable of extracting depth-resolved spectroscopic information, of realizing spectroscopic OCT mea-

surements. One might ask now how this method compares to the more widely employed JTFA. This is the subject of the next section.

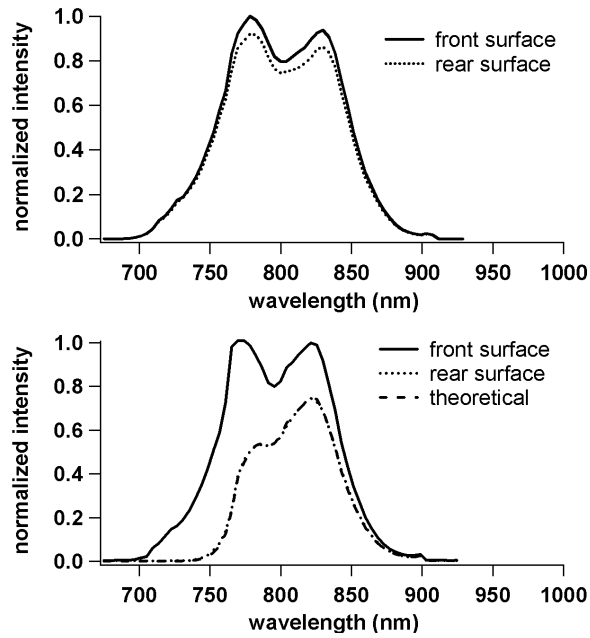


Figure 3.5: Spectra of back reflections from front and rear surfaces of BK7 plate (top) and of filter RG780 (bottom). The theoretically expected spectrum from the rear surface is identical to the measured one.

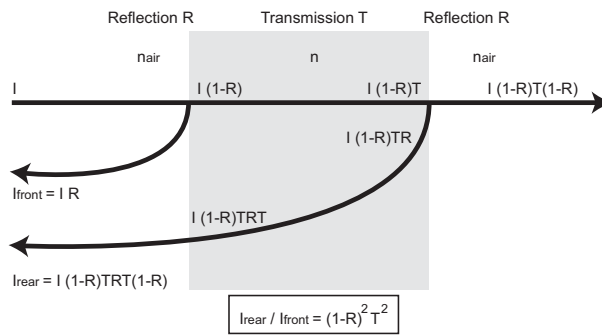


Figure 3.6: Schematic for the derivation of equation 3.6, illustrating the intensities reflected from the front and rear interfaces of a glass filter plate of transmission  $T$ .

## 3.2 Comparison of JTFA and wavelength de-multiplexing

### 3.2.1 General considerations

Wavelength de-multiplexing corresponds to an experimental realization of a JTFA. Whereas in the numerical method the windowed Fourier transformations are done on a previously acquired and digitized electrical signal via a computer, in this case it is done optically using a grating or a prism in the case of wavelength de-multiplexing. The situation is schematically illustrated in figure 3.7.

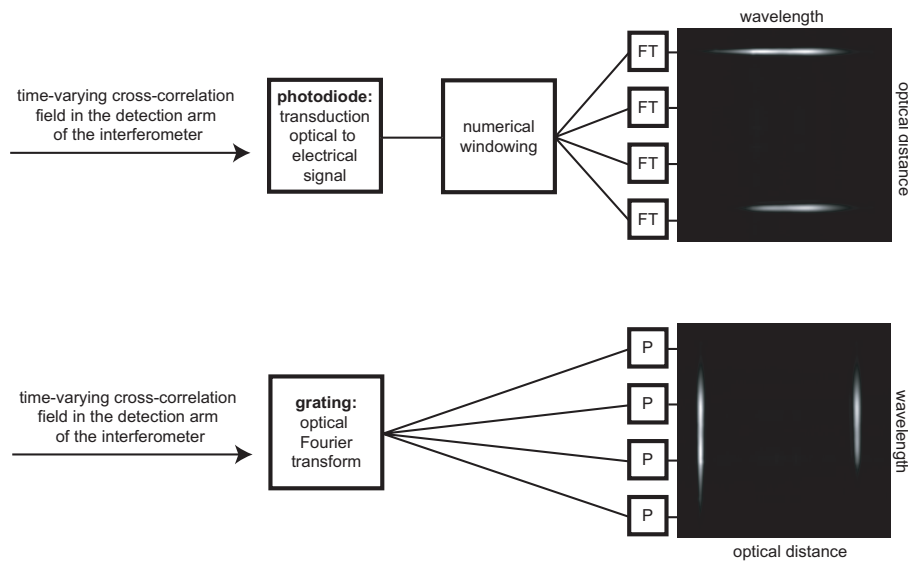


Figure 3.7: Schematic comparison of JTFA in time-domain OCT using windowed Fourier transformations (top) and wavelength de-multiplexing (bottom). FT stands for Fourier transform and P for photodiode.

Using wavelets instead of windowed Fourier transforms for a JTFA reduces problems with windowing effects, but it is for the sake of this comparison qualitatively similar. There is no fundamental difference between the two approaches, only a different order of manipulations and different ways of realizing the same manipulations. Let's take a look at the most important performance criteria:

#### Axial vs. spectral resolutions

The same trade-off between axial and spectral resolutions applies to both methods. This is a fundamental limitation already mentioned earlier (see equation 3.4). In wavelength de-multiplexing one dictates the form and the bandwidth of the optical spectrum detected by each wavelength channel. This in turn determines the axial resolution. In JTFA it is either the spectral or the axial resolution that is fixed first by the size of the analyzing windows, depending on the measurement domain.

#### Windowing problems

Windowing effects are a problem in both approaches. Being liable for introducing abrupt edges in the data to be Fourier transformed, careless windowing can create numerical noise in the case of JTFA. However, many high performing windows have been studied and the use of wavelets reduces this problem even further. Windowing effects are also present in the wavelength de-multiplexing method due to the geometrical shape of the photodiodes that integrate the signal over their surface in the frequency domain. Standard photodiodes correspond to a rectangular window being applied to the optical spectrum. The

associated creation of sidelobes in the interference signal has already been noted in the previous section. Some form of optical apodization using for example apodized microlenses could be introduced in order to reduce this effect.

### Signal-to-noise ratio

Comparing the overall signal-to-noise ratio (SNR) of both methods is a difficult task due to the many possible noise sources in experimental systems and the different approaches in the numerical field. However, let us consider two ideal systems without any other noise than shot noise, ideal experimental conditions and no errors due to numerical problems in order to identify possible fundamental differences in SNR performance. For the JTFA approach let it be a time-domain OCT setup for clarity of comparison. Both receive the same optical signal of equivalent power.

The maximum theoretical SNR of a shot-noise limited system is given by equation 2.1 which is reproduced here for easier reading:

$$SNR_{max} = 10 \log \left( \frac{\eta}{2h\nu} \frac{P_{s,max}}{B} \right) \quad (3.7)$$

where  $B$  has been derived in equation 2.4 to be

$$B = 2 \frac{\Delta\lambda}{\lambda_0} f_{Doppler} \quad (3.8)$$

The values of  $P_{s,max}$  and  $B$  to be considered are different in the two approaches. In the de-multiplexing method the detected power in each of  $N$  wavelength channels is approximately  $P_{s,max}/N$ , a factor of  $N$  less than in the JTFA detection. This simple relationship is valid for a hypothetical light source with a top-hat formed spectrum and separation into non-overlapping wavelength channels, which is considered to be an acceptable approximation for the sake of this comparison. Stepwise integration of the power spectral density is necessary to derive relationships that take into account other spectral forms.

The detection bandwidths applicable to either method are principally determined by the width of the detected light spectrum  $\Delta\lambda$ . The wavelength separation reduces its value by a factor  $N$  compared to the direct detection, again assuming the before-mentioned approximations. Both the central wavelength  $\lambda_0$  and the Doppler frequency  $f_{Doppler} = 2V/\lambda_0$ , where  $V$  is the depth scan speed, also change from wavelength channel to channel. However, the latter contribution is typically an order of magnitude less than the differences in  $\Delta\lambda$  and shall be neglected here.

Thus, because of the identical reduction of detected power and detection bandwidth per wavelength channel, the wavelength de-multiplexing method yields the same SNR as the JTFA detection in this first approximation. The process of windowing and numerical Fourier transformation in the case of JTFA does not affect the SNR. It is a fundamental characteristic of Fourier transformations that the norm is conserved between the time and frequency domains (Parseval's formula).

In a non-idealized case, differences in SNR performance are principally introduced by signal losses due to the optical wavelength separation and multiple channel detection on the one hand and windowing and rounding errors on the other.

### Flexibility and speed

Much more notable differences between the two approaches are in terms of flexibility and speed. JTFA is clearly much more flexible than wavelength de-multiplexing. As mentioned earlier, JTFA offers the advantage of complete liberty over the choice between axial and spectral resolutions for a given measurement at the push of a button, even permitting the calculation of many different resolutions. No

particular experimental conditions are imposed by the method, making it possible to treat older measurements for spectroscopic information that at the time of acquisition were not intended to be analysed in this manner. On the other hand, the numerical treatment is computationally intensive, limiting JTFA to post-processing for the time being. However, computer speeds are still increasing rapidly and it is probable that JTFA could be used in real-time in a few years. Wavelength de-multiplexing takes advantage of the instantaneous optical Fourier transform realized by the grating or the prism. It can therefore already be applied in real-time without difficulty. Combining this advantage with the smart pixel detector technology for direct envelope detection is the subject of section 3.3.

### **Spectral stability**

A weakness of JTFA in time-domain OCT is that the spectroscopic information is obtained via the interpretation of the signal's Doppler frequency. In the case of a non-linear scan mechanism or a moving sample (presenting flow, for example) the measured Doppler frequencies are attributed to wrong wavelength values. The extent of this problem has been verified experimentally for the scanning device used throughout this thesis. The results are presented in chapter 4. The problem is non-existent in the case of wavelength de-multiplexing, because the wavelength separation is performed optically. A demonstration of this problem can be seen in the following experimental comparison of the two methods.

### **3.2.2 Experimental comparison**

An experimental comparison of the two methods has been realized with the setup described in section 3.1.3 and with a Nd-doped Lanthanum Scandium Borate (Nd:LSB) crystal as absorbing sample. The crystal has polished and nearly parallel interfaces and is transparent in the near infrared except for Nd absorption bands at around 748 nm, 808 nm and 880 nm. A JTFA was realized on the zero diffraction order signal of the experimental measurement using a short time Fourier analysis with a Hanning window. The window size was chosen to yield comparable axial and spectral resolutions for both methods. The resulting spectrograms are shown in figure 3.8.

### **Spectral stability**

The before-mentioned weakness of JTFA to scan non-linearities becomes apparent in this experiment. The calculated spectra for the air-crystal and crystal-air interfaces seem to be wavelength-shifted (see figures 3.8 and 3.10). This shift is due to a different signal Doppler frequency introduced by different scan speeds in the beginning and the end of the scan. Even the spectral shape itself is subject to scan-induced modifications, as will be further illustrated in chapter 4. Without scan calibration, the spectral measurement and the association of wavelength values to the calculated data is therefore to be considered with caution. In the present case, the JTFA data was adjusted to spectrally coincide with the de-multiplexing data for the second crystal-air interface.

### **Axial and spectral resolutions**

Cuts along the axial and spectral dimensions of figure 3.8 are shown in figures 3.9 and 3.10. In the wavelength de-multiplexing case, the same experimental conditions were used as in section 3.1.3 and the resolutions obtained there are approximately reproduced. The axial resolution is 90  $\mu\text{m}$  and the spectral resolution as dictated by the setup is 8.6 nm. The resolutions obtained with the JTFA analysis depend primarily on the chosen analysis window size. With the numerical JTFA implementation used, the window size is restricted to powers of 2. The size yielding the closest match of axial resolution with the de-multiplexing method was chosen. The obtained resolution value is 105  $\mu\text{m}$ . Using equation



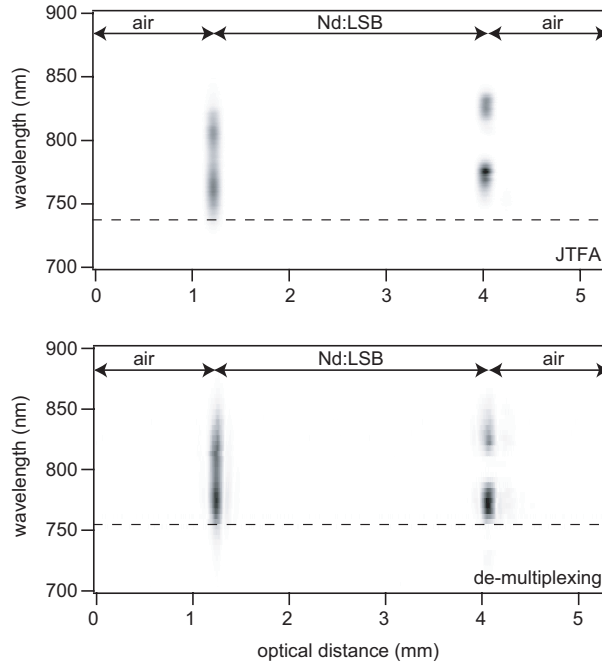


Figure 3.8: Time-wavelength plots for Nd-doped crystal in linear inverse gray scale. (top) Calculated from zero order A scan using windowed Fourier transforms, (bottom) wavelength de-multiplexed acquisition. The strong absorption of Nd at 808 nm is particularly visible on the second interface. The spectra of the interfaces calculated by JTFA (top) are wavelength-shifted with respect to each other due to scan non-linearities, as indicated by the dashed lines.

3.4 with a value of  $k$  corresponding to a Hanning window, a theoretical spectral bandwidth of 3 nm is expected, yielding a spectral resolution of 6 nm.

In order to compare the spectroscopic measurement to published reference values, the spectral transmission curve  $T$  is calculated from the spectra  $S_1$  and  $S_2$  of the air-crystal and crystal-air interface reflections (figure 3.10), respectively:

$$T = \frac{S_2}{S_1} = \exp(-\alpha d) = \exp(-\sigma Nd) \quad (3.9)$$

The crystal thickness is abbreviated as  $d$ , the absorption coefficient as  $\alpha$ ,  $\sigma$  stands for the Nd absorption cross section and  $N$  for the Nd concentration. The studied crystal was doped with  $N = 2.55 \cdot 10^{21} \text{ cm}^{-3}$ . Its physical thickness is determined from the measured optical thickness (2.82 mm) and the known index of refraction of Nd:LSB ( $n=1.84$ ) to be  $d = 1.58 \text{ mm}$ . The spectral absorption cross section values have been taken from [12]. Figure 3.11 shows the transmission curves obtained for both methods, compared to the published reference curve. The measurements' sensitivity limits, as determined below, are also indicated on the graph. For the JTFA data, the scan-induced wavelength shift between the two interface reflections has been corrected before applying equation 3.9.

The two Nd-absorption bands centered at 748 nm and 808 nm, lying within the spectrum of the employed light source, are clearly detected by both methods. The theoretically estimated spectral resolution difference of 50% between the two measurements is apparent. The de-multiplexing result, due to its lower resolution and subsequent signal integration, resolves less spectral features and has a generally higher transmission value. In addition to this integration effect, the comparison to the reference curve suffers from the sensitivity limits of the measurement, which do not allow the resolution of the two most prominent absorption peaks.

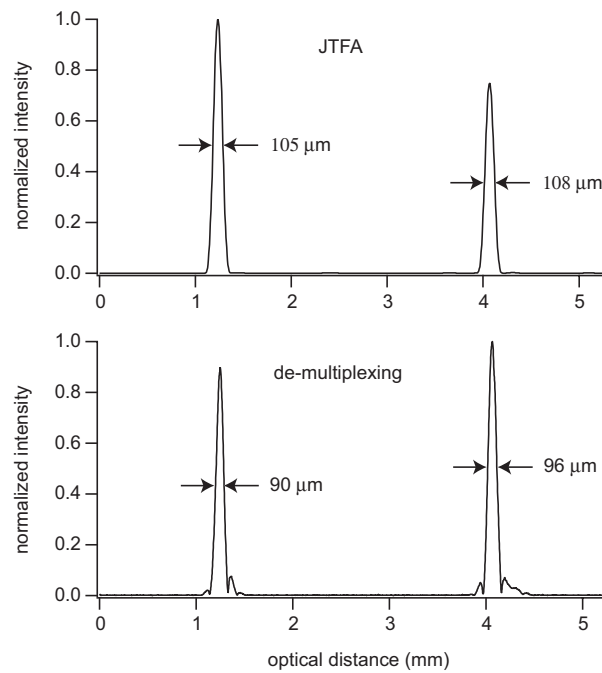


Figure 3.9: Cuts along the depth axis at a wavelength of 770 nm of the results in figure 3.8, normalized to the maximum value. Indicated are the FWHM values for the measured interface signals. The apparent amplitude difference between the signals of front and back interfaces in the JTFA case are due to the scan-induced wavelength shift. In the wavelength de-multiplexing case it stems from a better optical alignment for the rear interface as compared to the front interface.

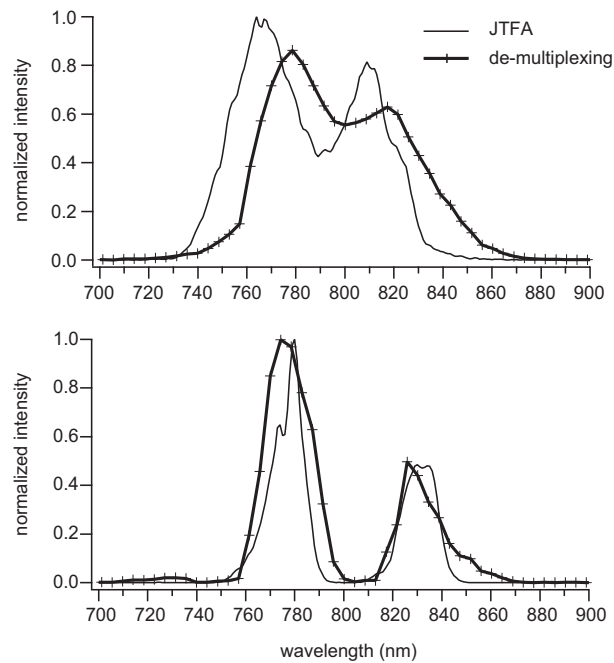


Figure 3.10: Cuts along the wavelength axis of the results in figure 3.8. (top) Air-crystal interface, (bottom) crystal-air interface. A very strong absorption is clearly visible at around 808 nm, almost completely canceling the reflection from the crystal-air interface. Note how the JTFA spectra are wavelength-shifted with respect to each other due to scan non-linearities.

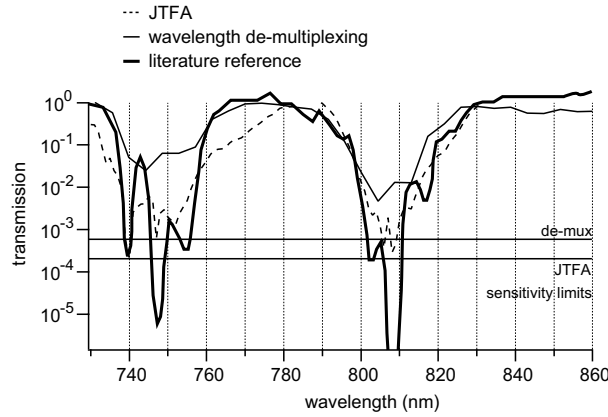


Figure 3.11: Transmission curve of Nd:LSB, as obtained with wavelength de-multiplexing and JTFA, compared to published reference curve from [12].

### Signal-to-noise ratio

Because the optical powers used in this experiment are in the mW-range, a shot-noise limited detection can be assumed for the comparison of the method's SNR. The theoretically obtainable SNR values are therefore given by equations 3.7 and 3.8. The two key parameters are the optical power and the detection bandwidth. Under experimental conditions, the total optical power in the interferometer's detection arm is divided equally into the zero and first diffraction orders by the grating. The first order signal power is then further divided into the different wavelength channels, whereas the zero order signal power is integrally detected by a single photodiode and subsequently analysed by JTFA.

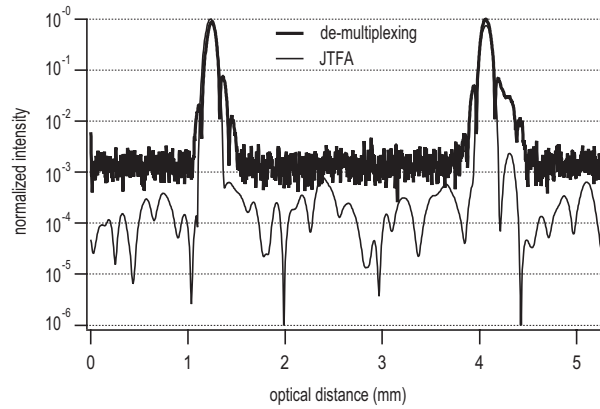


Figure 3.12: Plots of figure 3.9 in logarithmic intensity scale.

Ideally, the employed detection bandwidths should be adapted to each of the two situations for direct comparison of the obtainable SNR. However, due to scan non-linearities introduced by the voice-coil translation stage, the signal's frequency spectra have an uncertainty corresponding to a wavelength shift of approximately 30 nm (see analysis in section 4.2, notably figure 4.8). This value has to be compared to the signals' optical spectra with their FWHM of 90 nm and 4.3 nm for the zero and first diffraction orders, respectively. Thus, for the JTFA measurement this corresponds to an uncertainty of only FWHM/3, but for the de-multiplexed channels the uncertainty is 7 FWHM. It is therefore not feasible to apply the ideal

filter bandwidth given by equation 3.8 to the first order measurements. Instead, both signals were filtered with an identical bandwidth, equal to the ideal one for the JTFA measurement.

The plot of figure 3.9 is reproduced in logarithmic scale in figure 3.12 in order to visualize the signal noise. The SNR was calculated as the standard deviation  $\sigma$  of the noise in these normalized plots, where noise is considered to be the only signal contribution outside the crystal interface reflections. Expressed in decibels, the SNR values are obtained through  $SNR = -20\log(\sigma)$  and found to be 64 dB for the wavelength de-multiplexed measurement and 74.4 dB for the JTFA measurement. The measured SNR difference is thus 10.4 dB.

According to equation 3.8 the ideal detection bandwidth is linearly proportional to the signal's optical bandwidth  $\Delta\lambda$ . The ideal filter bandwidth for the de-multiplexed measurement would therefore be a factor of  $90 \text{ nm}/4.3 \text{ nm} = 21$  smaller than the actually used one. According to equation 3.7 this theoretically results in a SNR increase of  $10\log(21) = 13 \text{ dB}$ , to be compared to the measured SNR difference of 10.4 dB. In conclusion, the experiment shows that the achieved SNR is indeed comparable with both approaches if the adapted detection bandwidths are used.

### 3.3 Spectroscopic optical coherence tomography based on wavelength de-multiplexing and smart pixel array detection

(accepted for publication in Optics Communications)

M. Laubscher, S. Bourquin, L. Froehly, B. Karamata and T. Lasser  
Laboratoire d'optique biomédicale, Swiss Federal Institute of Technology,  
CH-1015 Lausanne, Switzerland

#### ABSTRACT

Current spectroscopic optical coherence tomography methods rely on *a posteriori* numerical calculation. We present an experimental alternative for accessing spectroscopic information in optical coherence tomography without post-processing based on wavelength de-multiplexing and parallel detection using a diffraction grating and a smart pixel detector array. Both a conventional A-scan with high axial resolution and the spectrally resolved measurement are acquired simultaneously. A proof-of-principle demonstration is given on a dynamically changing absorbing sample. The method's potential for fast spectroscopic OCT imaging is discussed. The spectral measurements obtained with this approach are insensitive to scan non-linearities or sample movements.

#### 3.3.1 Introduction

Optical coherence tomography (OCT) is a biomedical imaging method based on low-coherence interferometry that has been developed in the last decade [13]. Originally only concerned with providing spatially resolved reflectivity maps of biomedical samples, it has rapidly evolved into a measuring modality that gives access to various spatially resolved functional parameters, such as flow velocities, birefringence or spectroscopic information. Current spectroscopic OCT (SOCT) methods rely on numerical post-processing of a conventional OCT signal in order to obtain spectral information, either in time-domain [1] or in Fourier-domain [2]. By realizing a joint time-frequency analysis using windowed Fourier transformations or wavelet transformations, the one-dimensional OCT signal is mapped into a two-dimensional time-frequency representation that allows to extract the time-resolved spectral information content of the signal.

In this paper we explore an alternative approach for obtaining spectroscopic information in OCT based on wavelength de-multiplexing of a broadband light source and direct envelope detection of the interferometric signal using a smart pixel detector array (SPDA). In contrast to the conventional methods, it does not require numerical post-processing and thus has the potential for faster SOCT measurements. The approach realizes spectroscopic measurements optically and is therefore insensitive to scan non-linearities or sample movements that can lead to erroneous results in the case of numerical time-domain SOCT. We show the feasibility of this approach in a proof-of-principle experiment and discuss its potentials.

#### 3.3.2 Method and optical setup

A conceptually simple way to obtain spectroscopic information in an OCT experiment is to use multiple broadband light sources of different central wavelengths. For each one a tomogram of the same sample region is acquired and the different tomograms are then compared to extract spectroscopic information. A first demonstration of differential absorption measurements using two different light sources has been shown by Schmitt et al. [9]. However, the commercially available superluminescent diode light sources commonly used for OCT operate in very restricted spectral bands, so multiple light sources over a large and continuous spectrum are very difficult to find. On the other hand, large spectral bandwidth sources

such as white light, femtosecond lasers or supercontinuum sources are now being used in OCT. They were introduced mainly in order to increase the axial resolution of tomograms, but one can also consider them as a spectral reservoir to be split into different wavelength bands, each of which to be treated as a separate detection channel. The associated reduction of spectral bandwidth decreases the axial resolution of such a spectral channel, in exchange of a gain in spectral resolution. This trade-off between axial and spectral resolutions is a fundamental limitation also encountered in numerical methods [2].

The wavelength separation is advantageously realized at the interferometer exit after having illuminated the sample with the whole spectrum. Using a detector array for channel acquisition permits a parallel read-out of all the wavelength channels. Watanabe and Itoh [11] have followed this approach using a prism spectrograph for wavelength separation and a CCD camera for channel detection. The realization proposed here is conceptually similar, but uses a grating spectrometer for wavelength demultiplexing and a CMOS SPDA for direct envelope detection of the spectrally resolved interference signals. The grating splits the light into a spectrally unchanged zero diffraction order that contains the conventional high resolution OCT signal and that is detected with a standard photodiode and the spectrally resolved first diffraction order that is detected by the SPDA. The employed  $58 \times 58$  pixel detector array performs amplitude demodulation on each pixel and has been developed especially for OCT [14]. It has been employed for imaging in scattering media [15] and for fast 3D OCT acquisition [16].

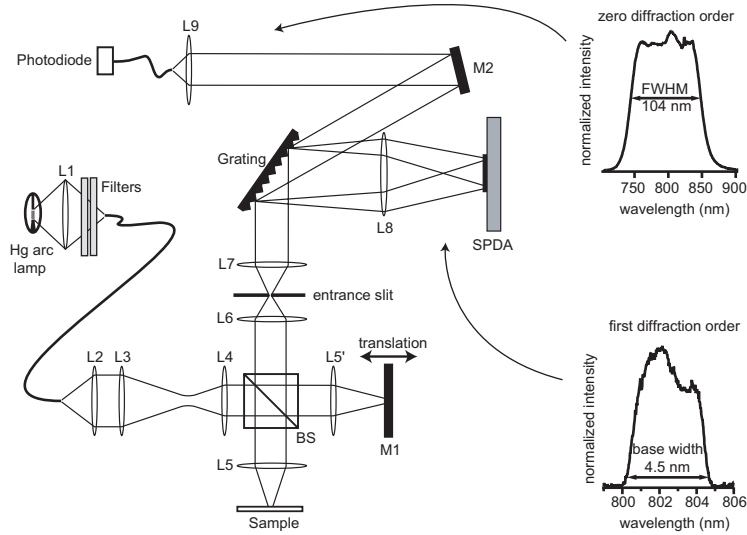


Figure 3.13: Optical setup and light spectra in the zero and first diffraction orders. Focal lengths of lenses L1-L9 (mm): 100, 30, 70, 50, 41, 40, 50, 100, 50; BS 50:50 beamsplitter cube. For spectral measurement, light was captured with a multimode fiber (core 50  $\mu\text{m}$ ) in the focal planes of L8 (one channel in the first diffraction order) and L9 (zero diffraction order) and detected with a resolution of 0.1 nm using an Ando AQ-6315B spectrum analyzer. For comparison with equation 3.10, the relevant spectral width in the first diffraction order is the base width. Scales are linear and normalized.

The optical setup is shown in figure 3.13. The light of a Hg-arc lamp is spectrally filtered with two interferometric filters (Andover 750FL07-50S and 850FL07-50S) in order to obtain a relatively flat spectral output with a 800 nm central wavelength and a 104 nm spectral width. It is injected into a multimode fiber with a core diameter of 550  $\mu\text{m}$  for easy handling and delivery. The fiber end is imaged via the lens system L2-L5 onto the sample and the reference mirror M1 of a free space Michelson interferometer. L5 and L5' are 4x microscope objectives with a numerical aperture (NA) of 0.1. The low NA was chosen in order to extend the depth of focus in the region of interest on the sample and thus allow for measurements without dynamic focusing. M1 is mounted on a voice-coil translation stage, driven by

a triangular signal at a frequency of 1 Hz. The total depth of scan is 4 mm, with the acquisition being done over 2 mm, once per cycle, yielding a signal Doppler frequency of 20 kHz. The illuminated area on the sample and on M1 has a diameter of 1 mm at the focal plane. The reflected light is recombined by a beam splitter cube and imaged onto the entrance slit of a spectrometer setup using lens L6. Lens L7 collimates the beam that is then diffracted by a 600 lines/mm diffraction grating under an incidence angle of 75 degrees. The zero diffraction order -the high resolution signal- is folded with mirror M2 and injected into a multimode fiber with a 50  $\mu\text{m}$  core diameter using lens L9. At the fiber end a photodiode detects the optical signal that is then pre-amplified and bandpass filtered before being digitized on a PC. In the first diffraction order -the spectrally resolved signal- laterally translated spectral images of the entrance slit are formed onto the SPDA via lens L8. Only one line of 58 pixels is used in this setup, being read 1500 times per A-scan. The data from the SPDA is acquired synchronously with the zero order signal and digitized on the PC for online display. The same acquisition card is used for both zero and first order signals. Scan triggering is realized by the voice coil scanner and subsequent pixel triggering for both zero order and first order signals is controlled by a clock circuit on the read-out board of the SPDA at a frequency of 312.5 kHz.

### 3.3.3 Measurements

#### Sample

In order to demonstrate the method's potential in a proof-of-principle experiment, a simple test sample with a dynamic change of absorption in the spectral region of interest was chosen. It consists of a two-layer system in the form of a liquid-containing cell delimited by a 160  $\mu\text{m}$ -thick microscope cover glass on the front side and a mirror on the back side. The thickness of the cell is 650  $\mu\text{m}$ . The experiment consists of observing the mixing dynamics of a drop of absorbing dye in the solvent-containing cell. The system is used vertically with the solvent being injected through an opening on the bottom of the cell prior to measurement and the dye being added through a second opening on the top of the cell during measurement, as indicated in figure 3.14a.

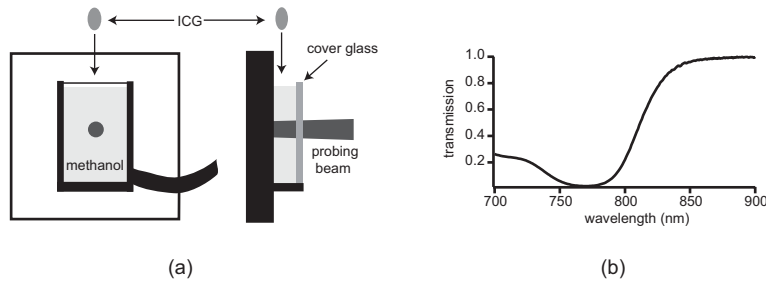


Figure 3.14: (a) Sample schematic, front and side views. The drop of ICG is added from the top into the solvent-filled cell. (b) Spectrally resolved transmission curve of ICG in methanol.

As absorbing dye we used indocyanine green (ICG), a substance being employed as a diagnostic aid for blood volume determination, cardiac output or hepatic function. Its optical absorption characteristics are described in [17]. Methanol was used as solvent. The spectrally resolved transmission curve between 700 nm and 900 nm as measured with a commercial spectrometer (Perkin-Elmer Lambda19) is shown in figure 3.14b. Drops with a volume of approximately 5  $\mu\text{l}$  and a concentration of  $2 \times 10^{-5} \text{ M}$  were used for adding to the cell (total cell volume 250  $\mu\text{l}$ ). The concentration in the cell varied therefore between  $0 - 2 \times 10^{-5} \text{ M}$  with an equilibrium value of  $3.9 \times 10^{-7} \text{ M}$ . These concentrations induce an optical attenuation of the mirror reflection at 800 nm of up to 99.8% (double pass).

## Results

A snapshot of the online data display during an ICG mixing process is shown in figure 3.15. The data acquired with the SPDA are represented as a depth-wavelength image plot in the center of the figure. These measurements are not corrected for the decreasing quantum yield of the silicon SPDA between 750 nm and 850 nm. The high-resolution zero order measurement can be seen above the SPDA image, sharing the same depth axis. The normalized transmission curve of the solution located between the mirror and the cover glass at the height of the probing beam is shown to the right of the SPDA image, on the same wavelength axis. It is obtained by dividing the signal intensity of the mirror surface by the intensity of the first cover glass interface for each wavelength channel. The form of the measured transmission curve corresponds to the one of figure 3.14b. Its amplitude varies with the local concentration seen by the probing beam.

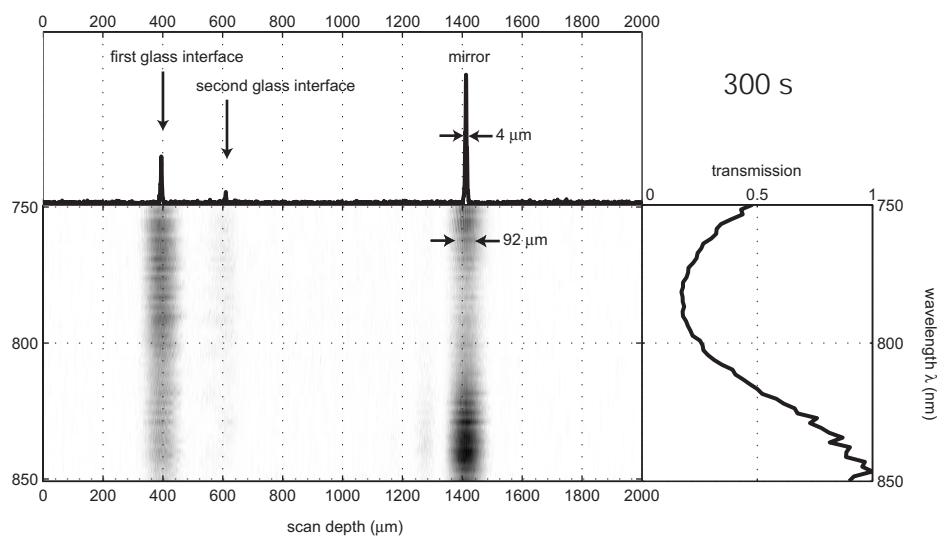


Figure 3.15: Snapshot at  $t=300$ s of a spectroscopic OCT measurement during an ICG mixing process. Depth-wavelength plot obtained with the SPDA in the center, high-resolution A-scan above on the same depth scale, normalized transmission curve to the right on the same wavelength scale.

In order to visualize the mixing dynamics when a drop of ICG solution is added to the cell, we plot the temporal evolution of the spatially-resolved spectral transmission curve in figure 3.16. During the first seconds of the measurement no ICG is present in the cell and the transmission curve is relatively flat. When the drop of ICG solution is added after 23 s, it passes through the probing beam and heavily absorbs it. The spectral components of the mirror reflections in the absorption band of ICG are completely lost. Sinking to the bottom of the cell, below the probing beam, the drop gets dissolved in the solvent. The transmission signal goes back up and varies thereafter according to the concentration of the ICG solution on the beam path. The mixing takes place slowly and by diffusion only. The equilibrium of homogenous ICG concentration in the cell is not reached on the time scale presented here. Unfortunately, longer measurements were not possible with the used sample setup because of solvent evaporation.

### 3.3.4 Discussion

#### Spectral and axial resolutions

The spectral resolution of the OCT measurement is limited by two factors, the spectral resolving power of the spectrometer setup ( $d\lambda_{spectro}$ ) on the one hand and the resolution limit given by the sampling of



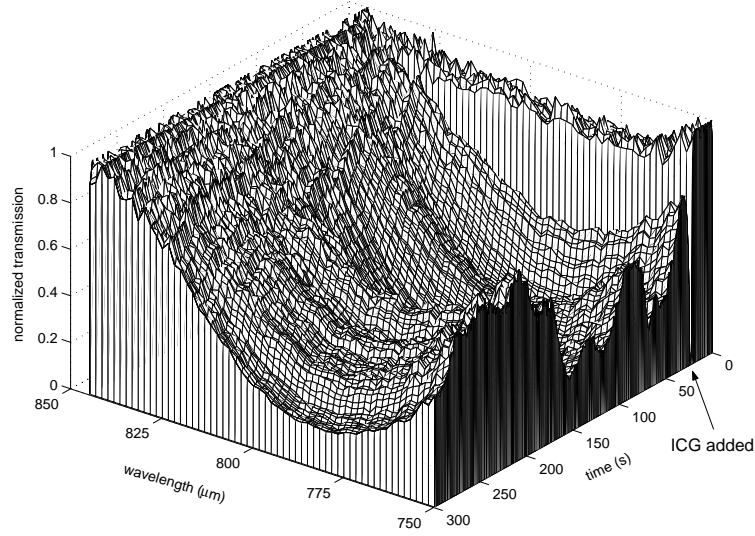


Figure 3.16: Temporal evolution of spatially resolved spectral transmission measurements during an ICG mixing process. Transmission curves represent localized transmission between the glass-solvent interface and the mirror surface. ICG is added to the methanol-filled cell at  $t=23s$ .

the spectral channels ( $d\lambda_{sampling}$ ) on the other. The spectral resolving power or spectrometer line profile is in the ideal case expressed as the convolution of the entrance slit image  $w'$  and the size  $p$  of the photosensitive area of a pixel [18]

$$d\lambda_{spectro} = (w' * p)D_{lin} = \left(\frac{f_8 \cos\alpha}{f_7 \cos\beta} w * p\right) \frac{\cos\beta}{Gf_8} \quad (3.10)$$

$D_{lin}$  is the linear dispersion in the focal plane of lens L8,  $f_7$ ,  $f_8$  the focal lengths of lenses L7 and L8,  $\alpha$  and  $\beta$  the incident and diffraction angles and  $G$  the grating line density. The Nyquist sampling limit is determined by the total spectral width  $\Delta\lambda$  projected on  $N$  spectral channels:  $d\lambda_{sampling} = 2\Delta\lambda/N$ .

In the case of the current setup with  $D_{lin} = 15.1$  nm/mm, a pixel array length of 6.4 mm and a pixel number of 58, we find  $d\lambda_{sampling} = 3.3$  nm. The resolving power of the spectrometer setup was chosen to be of roughly the same order with  $w = 0.3$  mm and  $p = 35$   $\mu m$ . This results in a base line width of the convolution in equation 3.10, i.e. the width of  $d\lambda_{spectro}$ , of 4.5 nm. The effective spectral resolution of the OCT setup is the larger of the two values, thus 4.5 nm. The spectra of one representative spectral channel and the total spectral shape of the light source captured with a multimode fiber (50  $\mu m$  core diameter) can be seen in figure 3.13. The spectra were acquired with an Ando AQ-6315B spectrum analyzer at a spectral resolution of 0.1nm.

The axial resolution  $\Delta z$  of an OCT measurement is given by

$$\Delta z = \frac{l_c}{2} = \frac{k \lambda_0^2}{2 \delta\lambda} \quad (3.11)$$

with  $l_c$  the coherence length,  $\lambda_0$  the central wavelength and  $\delta\lambda$  the bandwidth;  $k$  is a factor of the order of unity that takes into account the spectral shape ( $k=0.882$  for a Gaussian shape,  $k=1.207$  for a rectangular shape [6]). The measured axial resolutions are 4  $\mu m$  and 92  $\mu m$ , for the zero and first diffraction order signals, respectively, corresponding to a factor  $k$  of 1.29 (see figure 3.15).

### Spectral stability

In time-domain SOCT the spectroscopic information is extracted by time-frequency analysis from a time-varying interferometric signal that is generated by an optical path difference (OPD) variation between the interferometer sample and reference arms. We have shown in a previous publication that the calculated spectra obtained in this manner can become heavily distorted and their precise wavelength association difficult in the case of non-linear OPD variations due to delay line imperfections [19]. The same problem is likely to arise when applying the numerical approach to *in vivo* spectroscopic measurements, where sample movements or flow can induce wavelength-shifts in the calculated spectra. By realizing the spectral analysis of the interferometric signal optically, as is done in Fourier-domain SOCT and in the here discussed wavelength de-multiplexing time-domain method, the obtained spectroscopic results are insensitive to scan non-linearities or sample movements, leading to an improved stability and precision of spectroscopic measurements.

### Imaging speed

In the presented proof-of-principle experiment the imaging speed was one spectroscopic A-scan per second. It was limited by the slow scanning mechanism and no particular effort was made to optimize this speed. Much faster delay lines such as rotating cube scanners [20] or rapid scanning optical delay lines [21] are available that would have permitted an increased imaging speed. Not requiring any post-processing, the limiting factor of the method is rather the maximum read-out rate of the SPDA. In the current implementation it is 5 Msamples/s. The discussed ICG measurements were carried out at 1/16th of this rate, still heavily over-sampling the data.

The principal advantage of the experimental method over the numerical method is that the proposed concept does not require any post-processing. However, the time penalty of numerical post-processing involved with both time-domain and Fourier-domain SOCT is difficult to estimate. It depends on the kind of algorithm used and especially on the computational speed of the employed computer. Any absolute values given here would soon be outdated. It seems therefore more useful to compare this limitation to the one encountered in the wavelength de-multiplexing method, which is given by the detector read-out rate. As will be discussed below, the required data sampling frequency is not changed by the wavelength de-multiplexing procedure with direct envelope detection. Thus, the ratio between the computation time in the post-processing approach and the acquisition time in the experimental approach for a given number of data points seems a valid indicator of the difference in imaging speed between the two methods. With a current 2.4-GHz Pentium IV processor, it takes approximately 20 ms to calculate the digital Fourier transform of a 1024-point array. Acquiring the same number of points with today's acquisition cards that easily reach speeds of 5 Msamples/s takes only 0.2 ms. So regardless of absolute values, the experimental method has a potential advantage in imaging speed of about a factor 100. Given that the same technological progress that provides us with ever-increasing computation speeds will also permit increased data acquisition rates, this advantage seems to be largely independent of gradual technological advances.

Without the need for post-processing, it is not necessary to measure the full, fringe-resolved, interferometric time-domain signal. Wavelength de-multiplexing makes envelope detection sufficient. It is therefore particularly advantageous to employ a SPDA that allows direct envelope detection in this context. It permits a further gain in imaging speed, because envelope detection requires a factor  $M$  less sampling points than fringe-resolved sampling, where  $M$  is given by

$$M = \frac{\Delta z}{\lambda_0/2} = k \frac{\lambda_0}{\delta \lambda} \quad (3.12)$$

In the present case,  $M$  equals approximately 10 (230) for the zero (first) diffraction order signal. In order to take full advantage of this fact, SPDAs should be used for the detection of both the zero and first diffraction order signals.

As described by equation 3.11, the axial resolution is decreased in the wavelength de-multiplexing process, corresponding to an increase in coherence length. When realizing envelope detection, this means that acquiring the signal of one wavelength channel requires proportionally less sampling points than for the spectrally unchanged signal. In exchange, a number of spectral channels have to be acquired instead of only one signal, which finally leads to a conservation of the required sampling frequency.

Using a two-dimensional SPDA allows for further simplification in an SOCT measurement. Instead of employing only one detector line for spectroscopic A-scans, the entire 2D array could be used to realize spectroscopic B-scans by spectrally imaging a line (58 neighboring points) of the sample in parallel. In this manner, no lateral scan would be necessary and a gain in imaging speed could possibly be achieved.

### Signal-to-noise ratio

In this first proof-of-principle experiment the optimization of signal-to-noise ratio (SNR) was not a concern. In previous publications the employed SPDA has shown to yield a sensitivity of 76 dB with a dynamic range of 50 dB [14, 16]. In a first approximation, the wavelength de-multiplexing method incurs no SNR penalty compared to standard detection if shot-noise limited, because the reduced power in each wavelength channel is compensated by a reduced detection bandwidth. The maximum theoretical SNR ( $SNR_{max}$ ) for a shot-noise limited OCT measurement is given by the following formula [22]:

$$SNR_{max} = 10 \log \left( \frac{\eta}{2h\nu} \frac{P_{s,max}}{B} \right) \quad (3.13)$$

where  $P_{s,max}$  is the maximum power back-reflected from the sample arm (as seen by one photodiode of the detector),  $B$  the detection bandwidth,  $\eta$  the quantum efficiency,  $h$  Planck's constant and  $\nu$  is the optical frequency of the light used. The optimum detection bandwidth  $B$  to filter out as much noise as possible without attenuating the OCT signal is given by

$$B = 2 \frac{\delta\lambda}{\lambda_0} f_{Doppler} \quad (3.14)$$

$\delta\lambda$  being the source spectrum full width at half maximum,  $\lambda_0$  the source spectrum central wavelength and  $f_{Doppler}$  the interference fringe frequency. Thus, the distribution of  $P_{s,max}$  over  $N$  wavelength channels is offset by the reduction of  $\delta\lambda$  by the same factor  $N$ . However, other limitations reduce the SNR in the wavelength de-multiplexing method, such as power losses due to zero and higher order grating diffractions and low pixel fill factor or difficulty of precise adjustment of the optimum filter bandwidth.

### 3.3.5 Conclusion

We have shown that optical wavelength de-multiplexing of a broadband light source in a time-domain OCT system permits online measurement of depth-resolved spectroscopic information directly without numerical post-processing when using a smart pixel detector array and a diffraction grating. The presented optical setup permits the simultaneous acquisition of both a conventional OCT A-scan with 4  $\mu\text{m}$  axial resolution and a spectrally resolved OCT measurement with 4.5 nm spectral resolution at a frame rate of 1 Hz. The system has been tested on a simple dynamically changing absorbing sample: the mixing process of ICG dye in a solvent-filled cell.

In this proof-of-principle experiment no attempt was made to optimize signal-to-noise ratio or acquisition speed. These factors are very much dependant on the type of detector array used, which is

the major limiting factor due to its detection sensitivity and read-out rate. Spectroscopic B-scans of  $58 \times 1500$  pixels at one frame per second with a sensitivity of 76 dB are within the limits of the current detector design. The used smart pixel detector array is the first of its kind and further developments are being made to increase the performance of these types of detectors [23].

It is estimated that the method itself has the potential of outperforming conventional spectroscopic OCT methods by two orders of magnitude in imaging speed. The theoretically obtainable signal-to-noise ratio is nearly equivalent to the one in standard time-domain OCT. Furthermore, the spectral measurements obtained with this method are insensitive to scan non-linearities or sample movements, making it particularly adapted for *in vivo* spectroscopic imaging.

### 3.4 Possible extension: multi-resolution spectroscopic OCT

Wavelength de-multiplexing offers the possibility of acquiring a spectroscopic OCT A-scan with different spectral and axial resolutions in one scan. By using the full 2D SPDA, each detector line can be attributed to a spectroscopic A-scan with a different compromise between spectral and axial resolutions. In this manner multi-resolution spectroscopic OCT acquisition can be performed. A possible experimental realization of this concept is indicated in figure 3.17.

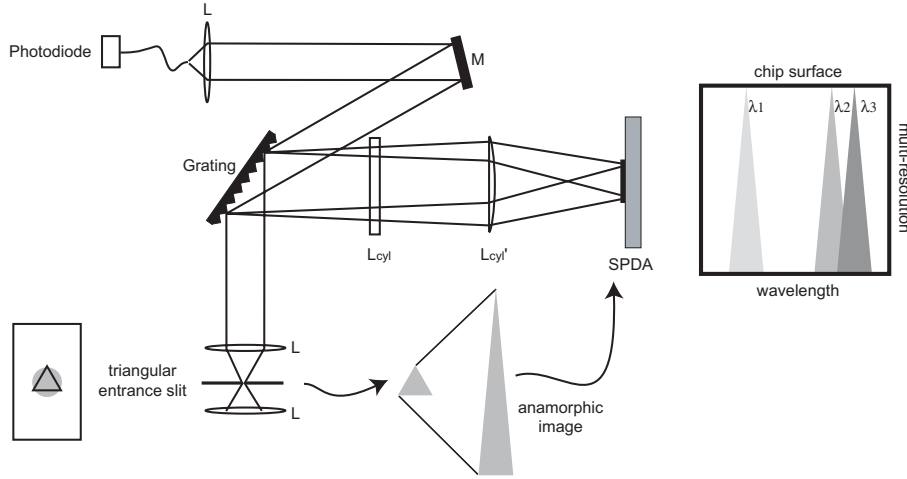


Figure 3.17: Interferometer detection arm of a multi-resolution spectroscopic OCT setup. By introducing a triangular shape with a customized spectrometer entrance slit and realizing an anamorphic image onto the SPDA chip surface, the spectral and thus also the axial resolutions will vary from one line of the SPDA to the next.

This setup is a slightly modified version of the one used in the previous section. Instead of employing a regular entrance slit in the spectrometer and illuminating only one line of the SPDA, a special triangular slit is introduced and its anamorphic image projected onto the whole detector array. With the help of two cylindrical lenses of different focal lengths, the originally isosceles triangular intensity distribution is stretched in one axis to cover the whole detector surface. The wavelength dependent diffraction introduced by the grating causes the various wavelength components to be projected onto the perpendicular axis. As the spectral resolution is primarily determined by the size of the entrance slit image (see equation 3.10), the linear variation of the slit's image size introduced by this setup causes a linear variation in the spectral and therefore axial resolutions for different detector lines.

Some limitations of the method become immediately apparent. An important part of the available signal power is filtered out by the triangular mask and is thus lost for the measurement. The rest is distributed over the whole two-dimensional array, leading to a proportional reduction in available signal-to-noise ratio. Furthermore, by employing the whole detector array for the spectral and multi-resolution dimensions, this approach is limited to the acquisition of A-scans. However, associated to a point-scanning OCT system, it represents an interesting experimental approach for online, multi-resolution, spectroscopic OCT. It has not been studied in depth so far for lack of time.

### 3.5 Conclusion

Wavelength de-multiplexing associated to parallel detection with a SPDA has been proposed as a new concept for spectroscopic OCT. Its feasibility has been demonstrated and it has been compared to the conventionally used numerical method for extracting spectroscopic information from standard OCT signals. This experimental approach is inherently faster than numerical methods and does not suffer from other fundamental performance penalties, such as resolution or signal-to-noise ratio. Furthermore, the spectral measurements obtained with this method are insensitive to scan non-linearities or sample movements, making it particularly adapted for *in vivo* spectroscopic imaging. However, it requires a particular experimental setup and is therefore less flexible than numerical methods.

Only the first steps have been taken so far in the study of this innovative concept. The method can be extended from the currently demonstrated spectroscopic A-scans to parallelly acquired spectroscopic B-scans by employing the entire two-dimensional SPDA. For studying scattering samples, it can be combined with more powerful pseudo-thermal light sources that would increase the obtainable sensitivity and eliminate optical cross-talk in parallel detection. Furthermore, the novel concept of multi-resolution spectroscopic OCT for simultaneous spectroscopic OCT measurements of different spectral resolutions that has been proposed here could be investigated.

### 3.6 References

- [1] U. Morgner, W. Drexler, F. X. Kartner, X. D. Li, C. Pitris, E. P. Ippen, and J. G. Fujimoto. Spectroscopic optical coherence tomography. *Optics Letters*, 25(2):111–13, 2000.
- [2] R. Leitgeb, M. Wojtkowski, A. Kowalczyk, C. K. Hitzenberger, M. Sticker, and A. F. Fercher. Spectral measurement of absorption by spectroscopic frequency-domain optical coherence tomography. *Optics Letters*, 25(11):820–2, 2000.
- [3] S. Qian and D. Chen. *Joint Time-Frequency Analysis*. Prentice Hall, 1996.
- [4] B. E. A. Saleh and M. C. Teich. *Fundamentals of Photonics*. John Wiley and Sons, 1991.
- [5] C. Akcay, P. Parrein, and J. P. Rolland. Estimation of longitudinal resolution in optical coherence imaging. *Applied Optics*, 41(25):5256–5262, 2002.
- [6] J. C. Diels and W. Rudolph. *Ultrashort Laser Pulse Phenomena*. Academic Press, 1996.
- [7] C. Hirlimann. Pulsed optics. In C. Rulliere, editor, *Femtosecond Laser Pulses*, page 31. Springer, 1998.
- [8] R. N. Bracewell. *The Fourier transform and its applications*. McGraw-Hill, 2000.
- [9] J. M. Schmitt, S. H. Xiang, and K. M. Yung. Differential absorption imaging with optical coherence tomography. *Journal of the Optical Society of America A (Optics, Image Science and Vision)*, 15(9):2288–96, 1998.
- [10] W. Watanabe, Y. Masuda, and K. Itoh. Dispersive coherence spectrotomography with white-light continuum. *Opt. Rev.*, 6:455–458, 1999.
- [11] W. Watanabe and K. Itoh. Coherence Spectrotomography: Optical spectroscopic tomography with low-coherence interferometry. *Opt. Rev.*, 7:406–414, 2000.
- [12] J. P. Meyn, T. Jensen, and G. Huber. Spectroscopic properties and efficient diode-pumped laser operation of Neodymium-doped Lanthanum Scandium Borate. *IEEE Journal of Quantum Electronics*, 30(4):913–917, 1994.
- [13] A. F. Fercher, W. Drexler, C. K. Hitzenberger, and T. Lasser. Optical coherence tomography - principles and applications. *Rep. Prog. Phys.*, 66:239–303, 2003.
- [14] S. Bourquin, P. Seitz, and R. P. Salathé. Optical coherence topography based on a two-dimensional smart detector array. *Optics Letters*, 26(8):512–514, 2001.
- [15] M. Ducros, M. Laubscher, B. Karamata, S. Bourquin, T. Lasser, and R. P. Salathé. Parallel optical coherence tomography in scattering samples using a two-dimensional smart-pixel detector array. *Optics Communications*, 202(1-3):29–35, 2002.
- [16] M. Laubscher, M. Ducros, B. Karamata, S. Bourquin, T. Lasser, and R. P. Salathé. Video-rate three-dimensional optical coherence tomography. *Optics Express*, 10(9):429–435, 2002.
- [17] M. L. J. Landsman, G. Kwant, G. A. Mook, and W. G. Zijlstra. Light- absorbing properties, stability, and spectral stabilization of indocyanine green. *Journal of Applied Physiology*, 40:575–583, 1976.
- [18] E. G. Loewen and E. Popov. *Diffraction Gratings and Applications*. Marcel Dekker, New York, 1997.

- [19] M. Laubscher, L. Froehly, B. Karamata, R. P. Salathé, and T. Lasser. Self-referenced method for optical path difference calibration in low-coherence tomography. *Optics Letters*, 28:2476–2478, 2003.
- [20] J. Szydlo, N. Delachenal, R. Gianotti, R. Walti, H. Bleuler, and R. P. Salathé. Air-turbine driven optical low-coherence reflectometry at 28.6-kHz scan repetition rate. *Optics Communications*, 154(1-3):1–4, 1998.
- [21] G. J. Tearney, B. E. Bouma, and J. G. Fujimoto. High-speed phase- and group-delay scanning with a grating-based phase control delay line. *Optics Letters*, 22(23):1811–1813, 1997.
- [22] E. A. Swanson, D. Huang, M. R. Hee, J. G. Fujimoto, C. P. Lin, and C. A. Puliafito. High-speed optical coherence domain reflectometry. *Optics Letters*, 17(2):151–3, 1992.
- [23] S. Beer, S. Waldis, and P. Seitz. Video-rate optical coherence tomography imaging with smart pixels. *Proc. SPIE*, 5140:69–76, 2003.



## Chapter 4

# Depth scan calibration

In all time-domain OCT setups, a depth scan has to be realized that shifts the coherence gate to different depths inside the sample. For precise, phase-sensitive and repetitive measurements, these scans have to be calibrated. The wavelength de-multiplexing setup described previously allows for the implementation of an innovative scan calibration technique that is the subject of this chapter. By narrow spectral filtering, the temporal coherence of part of the light can be increased and used to precisely measure the optical path difference variation introduced by the employed axial scanning device. In the first section of this chapter, the need for scan calibration is discussed with the help of the example of three different scan mechanisms. A commonly used method for measuring the non-linearities of scanners in interferometry is by way of a secondary interferometer with a high-coherence source. This approach is tested on the employed scanner and the results are described in section 4.2. In the next section, the proposed self-referenced calibration technique is introduced and applied to the same scanner. The resulting scan correction is demonstrated by comparing the corrected and the uncorrected cross-correlation measurements of a pellicle beam splitter when applying a recently published, numerical technique for sidelobe suppression in OCT. This technique manipulates the Fourier components of the measured signals and is thus very sensitive to frequency shifts introduced by scan non-linearities. In section 4.4 the used algorithms for scan calibration and sidelobe suppression are explained in detail. The possibility for numerically correcting the dispersion mismatch in an interferometer is a natural extension of the latter and is briefly discussed there as well. Several possible implementations and extensions of the depth scan calibration method are proposed in section 4.5.

### 4.1 The need for scan calibration

The ideal scan mechanism for time-domain OCT is fast, reproducible, introduces a completely linear change in optical path difference (OPD) and shows no random fluctuations. This scan mechanism has still to be found. An important problem with current scanning techniques is that their variation of OPD is not perfectly linear in time and that the phase shifts they introduce are not always reproducible from one scan to the other. The result in an OCT device are image distortion and errors in the interpretation of data. For most applications they are negligible, but for phase-sensitive measuring schemes, for example, the non-linearities may induce large measurement errors [1, 2]. Consider the following examples of currently employed scan mechanisms for OCT:

#### Voice-coil translation stage

The conceptually simplest scan mechanism for optical path modulation is the translation of the interferometer's reference mirror with a translation stage. In all the experiments presented in this thesis a

highly versatile, computer-controlled voice-coil translation stage from Physik Instrumente was used. It has a maximum scan range of 6 mm and a scan repetition rate of up to 20 Hz. Different translation movements are pre-programmed, among them a triangular scan that is generally used for approximating a linear mirror displacement. Figure 4.1 shows the displacement and scan speed pattern of a typical scan as measured with the double interferometer calibration method to be discussed in the next section. Differences in scan speed at different moments of the scan can easily reach 10%.

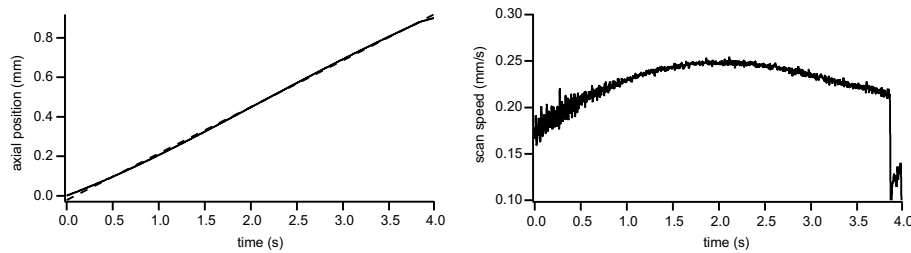


Figure 4.1: Typical displacement and scan speed pattern of voice-coil translation stage during a depth scan. Dashed line is a linear fit of the displacement curve for visual reference.

### Rotating cube scanner

The currently fastest scan method is based on the rotating cube principle being described by [3–5]. Introducing a rotative scan movement eliminates the speed-penalizing acceleration and deceleration problems of linear scanners. The principle is illustrated in figure 4.2.

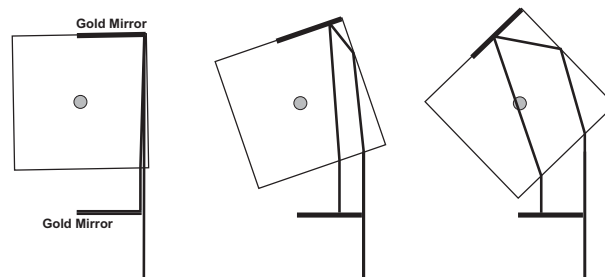


Figure 4.2: Principle of the rotating cube scanner. The incoming beam is reflected internally by total internal reflection and due to the gold plating on the cube corner, exits the cube, is reflected back by a fixed mirror and retraces its way back to the point of entry. By turning the cube the optical path varies nearly linearly with the rotating angle.

When rotating the cube with a constant velocity the OPD variation is nearly linear for small angles, but becomes highly non-linear for larger angles, as can be seen in figure 4.3. This scan method induces a large and OPD-dependent dispersion due to the varying distance traveled inside the glass cube. It is therefore of limited use in high resolution OCT.

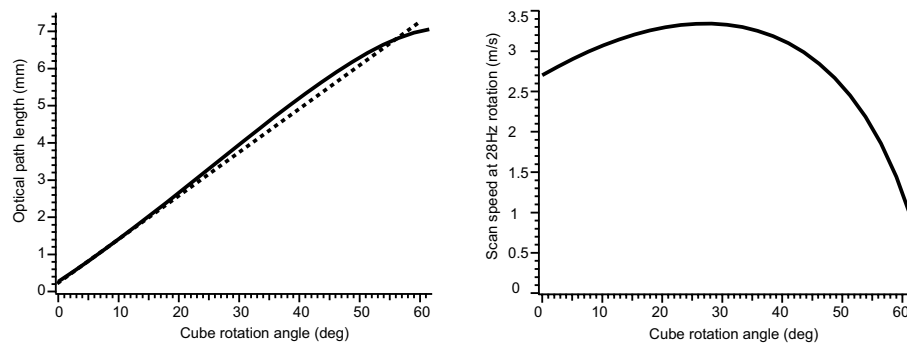


Figure 4.3: OPD variation and scan speed as a function of relative angle between cube and beam based on interferometric measurements. Dashed line is a linear fit for reference.

### Rapid-scanning optical delay line

The currently most employed scanner type in OCT is the so-called rapid-scanning optical delay line (RSOD) [6, 7]. It consists of a diffraction grating, a lens and a mirror whose tilt angle is to be rapidly scanned (see figure 4.4). The grating realizes an optical time-frequency Fourier transformation and the inclined mirror located at the focal plane of the lens introduces a linear phase shift among the Fourier components. Upon back transformation by the grating, this phase shift becomes a constant time shift, i.e. a different scan position. By rapidly changing the mirror inclination, an entire scan is realized. Besides reaching high scan speeds, this scanning method also allows for the independent setting of group and phase velocities. However, scan non-linearities are still present also with this method, as can be seen on figure 4.4.

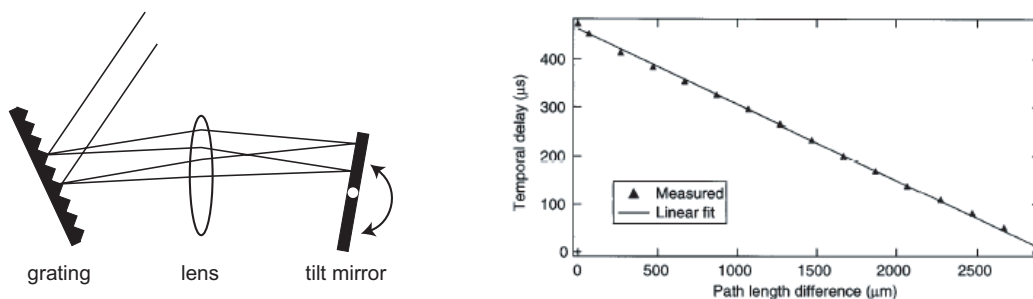


Figure 4.4: Schematic and temporal delay of grating-based RSOD (reproduced from [7]).

If the OPD variations are not perfectly linear, those non-linearities should at least be well-known, i.e. precisely measured. If they are not stable from one scan to the other, continuous monitoring is necessary. A very precise way of recording the OPD variation of the scan mechanism is by using a second interferometer with a high coherent light source and realizing an interferometric measurement. This is what can be called the double interferometer calibration method, discussed in the following section.

## 4.2 Double interferometer calibration method

In addition to the low coherence interferometer a second interferometer is employed that shares with one of its arms the OPD variation device of the primary interferometer. It uses a high coherence light source in order to measure the OPD variation introduced by the scan mechanism over its entire scan length by recording the interference fringes. Based on the simultaneous measurement of the standard OCT signal and the high-coherence signal, the OPD non-linearities can subsequently be corrected for. A possible correction algorithm is presented in section 4.4.1.

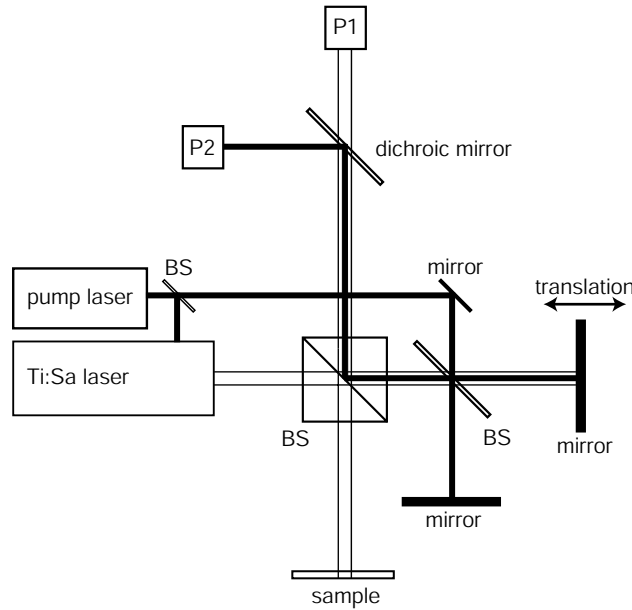


Figure 4.5: Optical setup for double interferometer calibration in free space Michelson interferometer. The pump laser serves as secondary high coherence source, BS stands for beam splitter and P1, P2 are photodiodes for the detection of the signal and the calibration measurement, respectively.

The setup shown in figure 4.5 was used to realize an OPD calibration based on the double interferometer method in a free space Michelson interferometer. As high coherence source was used a part of the pump laser radiation (532 nm) of the Ti:Sa mode-locked laser. The beams of both lasers were visually superimposed on the reference mirror that was mounted on the voice-coil translation stage.

The difficulty of this method lies in the relative alignment of the two interferometers. Only if the two beams of different coherence that probe the OPD variation device are completely superimposed can the measured calibration signal be applied to correct the scan non-linearities. Otherwise the two beams might experience different conditions and the calibration data is of no use. That is why this calibration method is very well adapted to fiber-based interferometers. If the two beams travel along the same optical fiber their superposition is automatically ensured. In a free-space interferometer this is not the case. Here the mutual alignment of the two beams is subject to experimental skill.

The following experiments illustrate how the apparently small non-linearities of the voice-coil scanner generate highly unstable and randomly varying Doppler frequencies in an autocorrelation measurement. Figures 4.6 to 4.8 show the Fourier spectra of autocorrelation measurements, uncorrected for scan non-linearities and corrected with the double interferometer calibration method for several consecutive scans. The abscissa are expressed in terms of the calculated wavelength given by the Fourier transformation. Please refer to section 4.4.1 for a detailed description of the calculations involved in the employed calibration algorithm.

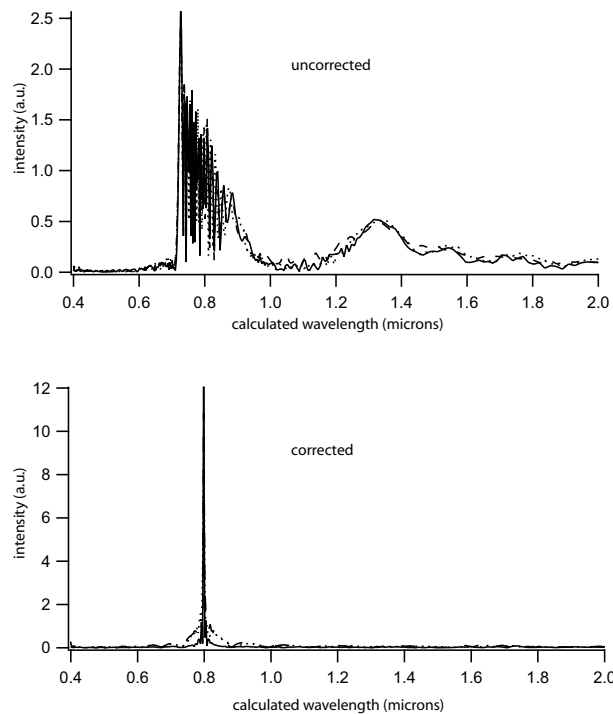


Figure 4.6: Fourier spectra of several autocorrelation measurements using a cw Ti:Sa laser. (top) uncorrected for scan non-linearities, (bottom) corrected based on the interferometric signal of the secondary high coherence source.

As a first example consider figure 4.6. It shows the Fourier transformation of an autocorrelation measurement using the laser in cw mode, i.e. monochromatic at 800 nm. The scan non-linearities completely deform the mono-line spectrum expected for this case, which is then fully recovered by correcting the scan.

In figure 4.7 the laser is mode-locked and delivers fs pulses that correspond to a large optical spectrum of approximately 100 nm (FWHM). The different measurements shown here were taken under identical experimental conditions, consecutively. It becomes clear that the scanner introduces random changes that vary noticeably from scan to scan. After taking into account those changes thanks to the high-coherence measurement, the calculated spectra are perfectly superimposed.

As a last example, figure 4.8 illustrates the differences introduced when the point of optical contact falls on different positions of the scan. The average Doppler frequency as well as the overall shape of the spectrum are heavily affected. Here again, the calibration permits to obtain reproducible measurements, unaffected from the imperfections of the scan mechanism.

The preceding measurement show that the double interferometer calibration method works well when correctly implemented. However, it comes at the price of a rather complicated experimental setup and very stringent alignment requirements. That's why a different method for OPD calibration was explored in this thesis that relies solely on the primary short coherence light source, as discussed in the next section.

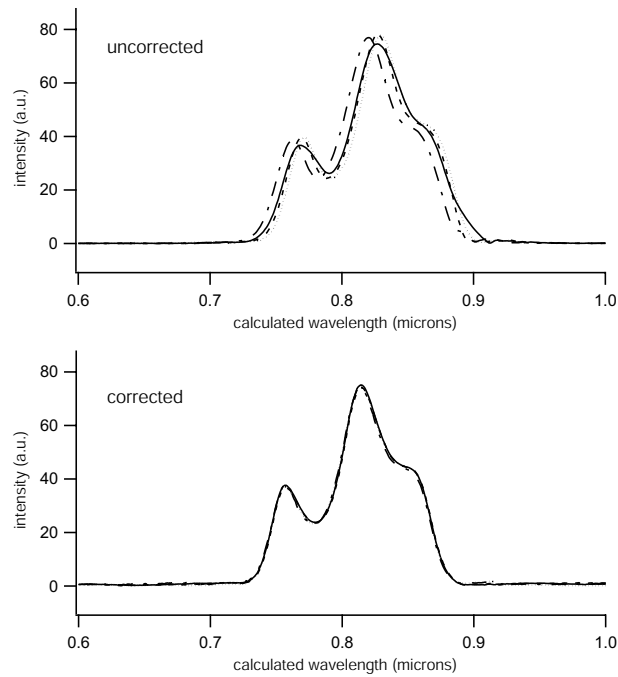


Figure 4.7: Fourier spectra of several autocorrelation measurements using a mode-locked Ti:Sa laser. The measurements were undertaken consecutively, under identical experimental conditions, (top) uncorrected for scan non-linearities, (bottom) corrected based on the interferometric signal of the secondary high coherence source.

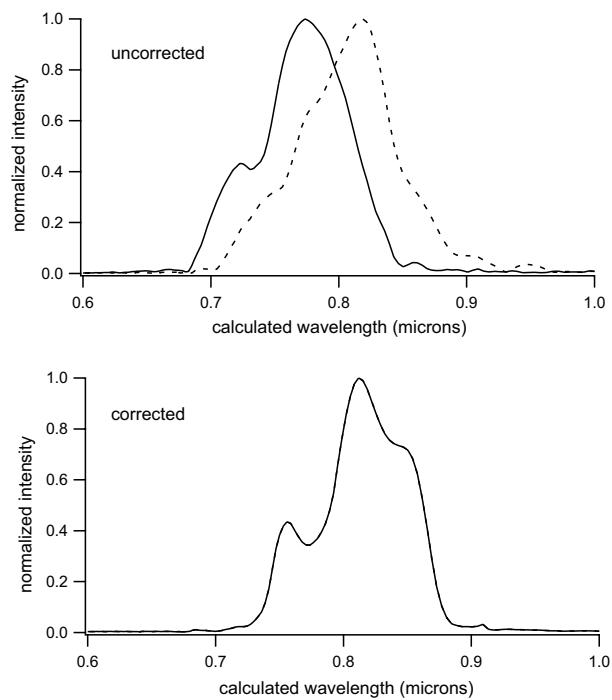


Figure 4.8: Fourier spectra of autocorrelation measurements using a mode-locked Ti:Sa laser. Two different positions of the scanner for the point of optical contact, (top) uncorrected for scan non-linearities, (bottom) corrected based on the interferometric signal of the secondary high coherence source.

### 4.3 Self-referenced method for optical path difference calibration in low coherence interferometry

(published in Optics Letters, 28, 2476-2478 (2003))

M. Laubscher, L. Froehly, B. Karamata, R.P. Salathé, T. Lasser

Institute of Biomedical Imaging, Optics and Engineering, Swiss Federal Institute of Technology,  
CH-1015 Lausanne, Switzerland

#### ABSTRACT

A simple method for the calibration of optical path difference modulation in low coherence interferometry is presented. By spectrally filtering a part of the detected interference signal a high coherence signal is obtained that encodes the scan imperfections and permits their correction. The method is self-referenced in the sense that no secondary high coherence light source is necessary. Its usefulness is demonstrated by combining it with a recently published digital spectral shaping technique for the thickness measurement of a pellicle beam splitter using a white light source.

Interferometric techniques such as white light interferometry or low coherence interferometry require a well known optical path difference (OPD) modulation of the two interfering beams. Because of the high precision requirements of optical interferometry and the random nature of scan imperfections it is rarely feasible to calibrate the OPD modulation once and apply corrections to subsequent measurements, but it is necessary to monitor it continuously. The most precise way of monitoring is by use of interferometry itself. However, if the temporal coherence length of the employed light source is shorter than the OPD introduced, a direct measurement of interference fringes over the whole modulation range becomes impossible. For this case it has become common practice to employ a secondary interferometer with a high temporal coherence source that shares with one of its beams the OPD modulation device of the primary interferometer, but has a separate detection system for simultaneous OPD modulation measurement. [3, 8, 9] Several authors have also pointed out the possibility of increasing the temporal coherence length of the primary short coherent light source by narrow-band spectral filtering, allowing for an OPD calibration over an increased scan range without employing a secondary high coherent light source. [3, 9] However, this possibility has to our knowledge not yet been experimentally verified and adequately exploited.

In this Letter we provide experimental proof of a calibration method for OPD modulation in low coherence interferometry that does not depend on a secondary light source and is therefore inherently more precise, more stable and simpler to realize than methods based on a secondary interferometer. As an example of application we use this method to show how a precise OPD calibration is a prerequisite for fully exploiting the potential of a recently published digital spectral shaping technique for optical coherence tomography when using light sources with highly non-Gaussian spectra. [10] This is demonstrated by measuring the thickness of a pellicle beam splitter with a white light source.

It is a well-known fact that the temporal coherence length  $l_c$  of light is inversely proportional to its spectral width  $\Delta\lambda$ :

$$l_c = k \frac{\lambda^2}{\Delta\lambda} \quad (4.1)$$

with  $\lambda$  the mean wavelength and  $k$  a factor of proportionality of the order of unity that depends on the form of the spectrum. It is thus possible to render low coherent light more coherent by limiting its spectrum. We make use of this fact in order to obtain both a high and a low temporal coherence signal from

a single low coherent light source. Optically filtering a small portion of the two interfering beams in the detection path of a modulated interferometer gives access to the high coherence interference signal, or calibration signal  $c$ , that encodes the OPD modulation over the range of its coherence length. The remaining unfiltered low coherence signal  $s$  that constitutes the actual measurement signal is acquired simultaneously via a second detection channel. The instantaneous phase of the sinusoidally modulated calibration signal is determined by use of a numerical Hilbert transformation. [11] Subsequent phase unwrapping gives access to the scanner position in terms of phase angle and as a function of time. Knowing the wavelength of the filtered calibration signal the phase angles can be expressed as relative OPDs. Because of the simultaneous acquisition of  $s$  and  $c$  each sampled signal value can then be associated with an OPD value and the signal  $s$  can be expressed directly in terms of OPD without any reference to time. However, the sampling intervals of consecutive values of  $s$  are then not necessarily constant and for certain data treatment operations such as Fourier transforms the signal has to be resampled with uniform interval spacing. In our case the resampled values were determined by linear interpolation.

Spectral filtering can be achieved by various means, the use of interference filters or color substrate filters being the most obvious. However, it can easily be deduced from relation 4.1 that the filter bandwidth necessary for practically useful scan ranges of a few hundred micrometers or more is of the order of a few nanometers in the visible and near infrared region of the spectrum, which is too narrow for commercially available filters. Much narrower bandwidths can be achieved with a spectrometer setup consisting of a dispersive optical element such as a prism or a diffraction grating, a lens and a pinhole. Because of its higher dispersive power we have chosen a grating in the experiments used to validate the proposed calibration method.

The optical setup can be seen in Figure 4.9. It will be discussed in more detail below. Using a grating offers the additional possibility of easily changing both the central wavelength and the filtered bandwidth simply by adjusting the position of the pinhole and the size of the beam originating from the grating. The spectral resolving power of a grating being directly given by the number of grooves illuminated, the useful scan range (the coherence length of the calibration signal) is

$$l_c = k\lambda GD \quad (4.2)$$

with  $G$  the grating constant and  $D$  the beam diameter. For this to hold true the aperture of the spectrometer subsystem has to be given by the diaphragm  $D$  and the pinhole being adapted to the spot size of the used focusing lens.

The advantage of this calibration method over a dual interferometer method lies mainly in its simplicity, flexibility and robustness. Only one light source and one interferometer are needed. The difficult and sometimes impossible task of precisely aligning two different light beams with different wavelengths and different divergences so that they share a common path in the OPD modulation device is no longer necessary. This method is self-referenced and insensitive to external influences that in the case of a dual interferometer method might introduce errors. Furthermore, it measures the real OPD between sample and reference beams, so should there be a displacement of the sample in addition to the OPD modulation, it is automatically taken into account.

The principal disadvantage of the method is that a portion of the light to be detected, which in general is already quite weak, has to be used for calibrating the OPD modulation device. The signal to noise ratio of the measurement will therefore decrease. Furthermore, the temporal response of the sample (and especially for scattering samples) introduces a spectral modulation that translates to a wavelength-dependent loss of fringe contrast of signal  $c$ . This problem can be attenuated for a given sample by either choosing a different calibration wavelength or by using a confocal depth-filtering scheme in order to reduce the spectral modulation.

The digital spectral shaping technique recently published by Tripahti et al. [10] is based on the calculation and application of a spectral correction curve in the Fourier domain of an acquired interference



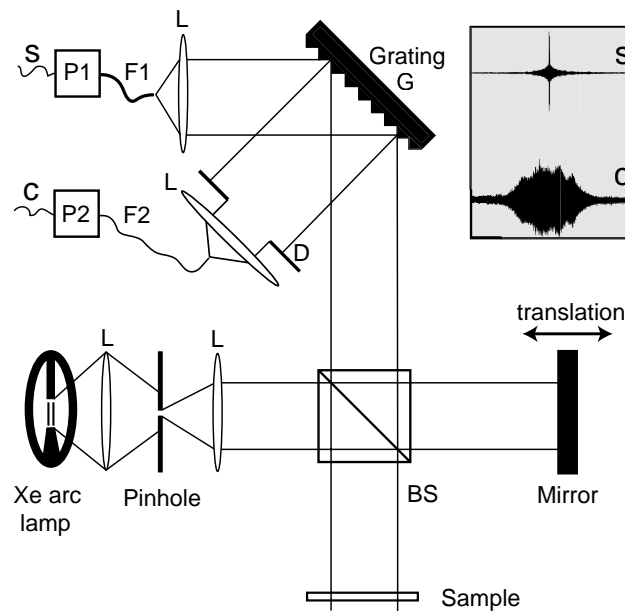


Figure 4.9: Optical setup: L lens, BS beam splitter, D diameter of beam limiting diaphragm, multimode fiber F1, monomode fiber F2 playing the role of a pinhole, photo detectors P1 and P2 for measurement signal *s* and calibration signal *c*.

signal that forces the original spectrum into a Gaussian shape. Upon back-transformation the sidelobes of the axial point-spread function are reduced with some penalty in the form of a decreased signal-to-noise ratio. For source spectra that are highly non-Gaussian with very marked and numerous emission lines the calculated spectral correction curve will also have very marked and fine features. If the OPD modulation from one scan to the next is not highly repeatable or well corrected, then the use of such a spectral correction curve will not improve the spectrum but to the contrary will introduce additional peaks and thus additional sidelobes. On the other hand if some averaged correction curve is used the spectral correction will only be marginal and the sidelobe suppression ineffective. The following measurements show how the precise calibration of OPD modulation based on our method makes it possible to apply this technique to highly non-Gaussian spectra.

The arc of a conventional Xe arc lamp is imaged onto a pinhole of  $100\ \mu\text{m}$  diameter and collimated into a free-space Michelson interferometer with a beam diameter of 1 cm. A non-polarizing large bandwidth beam splitter cube separates this beam into a sample and reference beam. The sample beam is reflected either from a  $2\ \mu\text{m}$  thick uncoated pellicle beam splitter for measurement or from a gold-plated mirror for calibration of the spectral shaping technique. The reference beam is reflected from a gold-plated mirror that is mounted on a voice-coil translation stage from Physik Instruments. The OPD is changed by scanning the translation stage in a triangle scan over a distance of 1 mm at a frequency of 1 Hz. A holographic grating with 1200 lines/mm is used at an incident angle of 45 degrees. The zero diffraction order is the unfiltered main signal *s* that is focused into a multimode optical fiber F1 of  $200\ \mu\text{m}$  core diameter and detected by the photodiode P1. The calibration signal *c* is obtained from a part of the first diffraction order that is focused into a monomode fiber F2 for spatial filtering and detected with a second photodiode P2. For this particular grating configuration some losses are introduced in the UV part of the spectrum due to the presence of higher diffraction orders. A higher diffracting grating could be used to eliminate these losses. The signals of both photodiodes are preamplified, digitized via a 12-bit acquisition card, digitally bandpass filtered for noise reduction and stored on a PC for post processing. The calibration algorithm is then applied a posteriori using Matlab routines. On a 2.4 GHz Pentium IV

processor the calibration of a  $2^{17}$ -point A-scan took 0.45 s.

Figure 4.10 shows the spectrum obtained by Fourier transformation of the interference signal of a mirror, with and without scan correction, compared to the original source spectrum. Note how the scan correction dramatically improves the resolution of spectral features like the Xe emission lines at 669 nm and 818 nm. Remaining differences to the original spectrum are attributed to the spectral response of the photodiode.

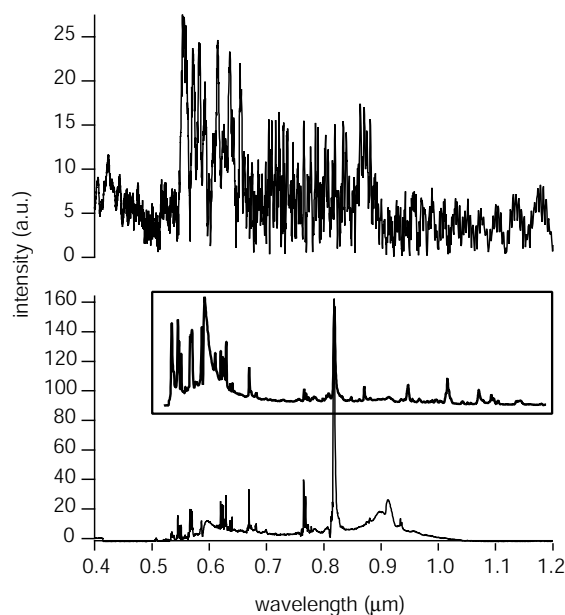


Figure 4.10: Spectra obtained by Fourier transformation of the interferogram of a mirror, (top) without scan correction, (bottom) with scan correction compared to the original source spectrum (middle insert).

Figure 4.11 shows the results of the spectral shaping technique applied to the pellicle beam splitter measurement. Figure 4.11a reproduces the measured interference signal  $s$ . The two interfaces of the membrane can be distinguished, but the coherent noise that is due to the non-Gaussian spectrum of the lamp extends far beyond the interfaces and masks the signal. In Figure 4.11b the spectral shaping technique has been applied without previously correcting the non-linearities of the scanner. In this case the technique introduces supplementary coherent noise and deteriorates the signal. The result of the spectral shaping technique when previously calibrating the OPD modulation can be seen in Figure 4.11c. The noise is markedly reduced and the two interfaces of the pellicle beam splitter are now clearly resolved. Note that due to the calibration the data in figure 4.11c can precisely be plotted as a function of OPD.

In conclusion, we have presented what we think to be the first experimental verification of a self-referenced calibration method of optical path difference modulation in low coherence interferometry. We have shown its feasibility and usefulness by applying it to the thickness measurement of a pellicle beam splitter using white light interferometry and a recently published digital spectral shaping technique. In its current post processing implementation the method imposes no limit on the maximum acquisition speed. However, for a real time implementation the use of a dedicated digital signal processor should be considered. The method's main drawback, a loss in signal to noise ratio, could be minimized by optical amplification of the calibration signal.

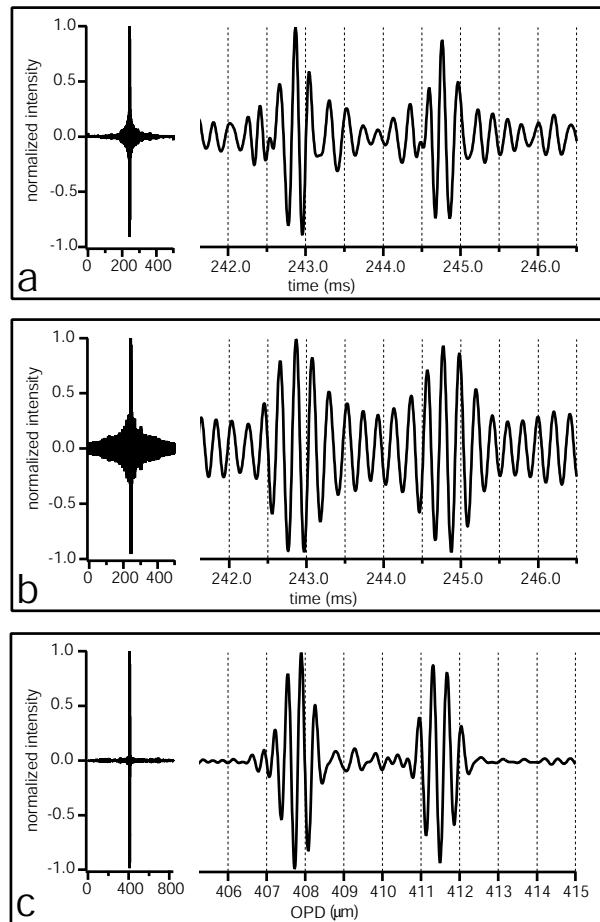


Figure 4.11: Application of spectral shaping technique to pellicle beam splitter measurement. (a) original signal  $s$ , (b) spectral shaping technique applied to uncalibrated measurement, (c) spectral shaping technique applied to calibrated measurement.

## 4.4 Details on calibration and spectral shaping algorithms

### 4.4.1 Calibration algorithm

The calibration algorithm used for both the double interferometer calibration method and the self-referenced method takes as input parameters the following two signals: the measurement signal  $s$  and the calibration signal  $c$ , each corresponding to a single A scan. It extracts the OPD variation from the calibration signal  $c$  by analyzing the signal's phase variation and uses this information to calibrate the measurement signal  $s$ . The calibration wavelength  $\lambda$  is assumed as known input parameter.

#### Phase extraction

The calibration signal  $c$  takes the following analytical form

$$c(t_i) = E(t_i) \cdot \cos\left(\frac{2\pi d(t_i)}{\lambda}\right) \quad (4.3)$$

where  $d$  is the OPD,  $\lambda$  the mean wavelength of the filtered spectrum and  $E$  the slowly varying envelope of the interference signal. The parameters' dependence on time is shown by  $(t_i)$  with index  $i$  indicating the discretely sampled acquisitions. In a first step, the complex analytic function  $\hat{c}$  of  $c$  is calculated in order to separate the envelope variations  $E(t_i)$  from the OPD variation  $2\pi d(t_i)/\lambda$

$$\hat{c} = c + H(c) \quad (4.4)$$

$$\hat{c} = E(t_i) \cdot \exp\left(\frac{j2\pi d(t_i)}{\lambda}\right) \quad (4.5)$$

with  $H$  symbolizing the Hilbert transform. The OPD variation is now easily accessible as the phase of the complex analytic function

$$\text{mod}_{2\pi}\left(\frac{2\pi d(t_i)}{\lambda}\right) = \tan^{-1}\left(\frac{\text{Im}(\hat{c})}{\text{Re}(\hat{c})}\right) \quad (4.6)$$

$$d(t_i) = \frac{\lambda}{2\pi} U\left[\tan^{-1}\left(\frac{\text{Im}(\hat{c})}{\text{Re}(\hat{c})}\right)\right] \quad (4.7)$$

$U$  is an operator that represents the phase unwrapping procedure. It removes the  $2\pi$ -discontinuities in the phase function by adding a multiple of  $2\pi$  whenever a discontinuity exceeds the value of  $\pi$ . A graphical representation of the phase extraction algorithm is shown in figure 4.12.

Because of the simultaneous acquisition of  $s$  and  $c$ , each signal value  $s(t_i)$  can be associated with the corresponding phase value  $2\pi d(t_i)/\lambda$ . The signal can then be expressed directly in terms of OPD without any reference to time. The scan non-linearities are thus corrected and the knowledge of  $\lambda$  permits to express OPD directly in microns. However, the sampling steps between different signal values are now not necessarily equally spaced anymore and if a subsequent Fourier analysis is intended, the data has to be resampled with even spacing.

#### Resampling

The task is to describe a certain functional relationship between a varying signal intensity for varying OPD values that is up to now expressed in the set of sampled values  $[d_j, s_j]$  that are unevenly spaced ( $d_j - d_{j+1} \neq cte$ ) by a different set of sampled values  $[z_i, r_i]$  that should be evenly spaced ( $z_i - z_{i+1} = cte$ ). The situation is illustrated in figure 4.13.

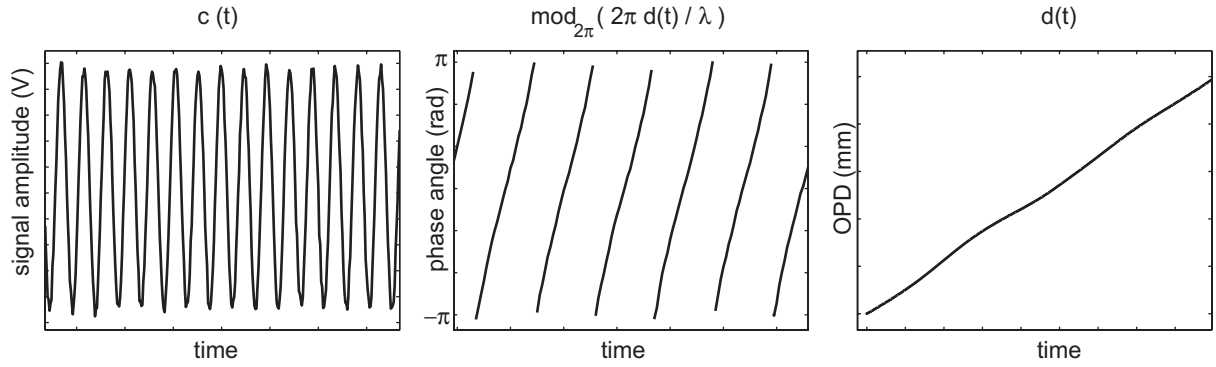


Figure 4.12: Illustration of phase extraction for OPD measurement. (left) Interferometric signal  $c(t)$ , (center) phase of complex analytic function, (right) unwrapped phase yielding OPD.

From one scan to another the total absolute scan length does not stay constant, but varies slightly by some tens of microns when using the Physik Instrument voice-coil scanner. For comparison between different scans the scan length has therefore first to be fixed to some common maximum OPD value before resampling. The number of sample points  $N$  is also fixed to a value on the order of the original number of points. The interval spacing  $\Delta$  is then calculated as the ratio of maximum OPD ( $OPD_{max}$ ) and  $N$

$$\Delta = \frac{OPD_{max}}{N} \quad (4.8)$$

and the series of new evenly spaced OPD sampling points  $z_i$  is calculated based on the knowledge of  $\Delta$  and an arbitrary starting value.

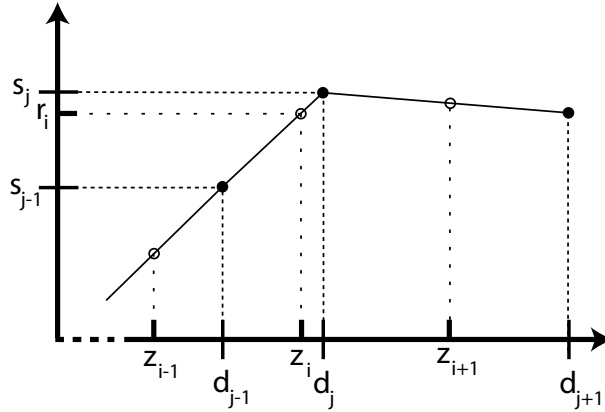


Figure 4.13: Illustration of resampling and interpolation procedure. Full dots correspond to original data points with uneven spacing, empty dots signify the resampled values that are evenly spaced.

What remains to be done is to associate to each  $z_i$  its corresponding intensity value  $r_i$ . Those values can be obtained by interpolation. For each couple of points  $d_j, d_{j-1}$  one finds the corresponding point  $z_i$  that falls into the interval. The value  $r_i$  is then calculated by linear interpolation as follows

$$r_i = s_{j-1} + (z_i - d_{j-1}) \frac{s_j - s_{j-1}}{d_j - d_{j-1}} \quad (4.9)$$

### 4.4.2 Spectral shaping algorithm

The spectral shaping algorithm used in section 4.3 has been inspired from [10]. It will now be described in detail. The input data for the algorithm are a scan-corrected autocorrelation measurement that is abbreviated as  $a(z_i)$  and the scan-corrected sample measurement called  $m(z_i)$ . Non-capital letters are used for functions in the space domain (variable  $z_i$ ) and capital letters for the complimentary function in the Fourier domain (variable  $\rho_j$ ). The five principal steps of the algorithm are the following (see also figure 4.14):

#### Fourier transformation

In the first step, the auto-correlation and the cross-correlation measurement,  $a$  and  $m$ , are Fourier transformed in order to obtain a representation of the source spectral density.

$$FT[a(z_i)] = A(\rho_j) = A_a(\rho_j) \cdot \exp[jA_p(\rho_j)] \quad (4.10)$$

$$FT[m(z_i)] = M(\rho_j) = M_a(\rho_j) \cdot \exp[jM_p(\rho_j)] \quad (4.11)$$

with the subscripts  $a$  and  $p$  representing the absolute value and the phase, respectively.  $A(\rho_j)$  and  $M(\rho_j)$  are symmetric complex functions with positive and negative Fourier components due to the real nature of  $a$  and  $m$ .

#### Gaussian fit

The non-Gaussian source spectrum  $A(\rho_j)$  is then developed into its first moments that yield the center and the width for an equivalent Gaussian spectral fit  $G(\rho_j)$  that represents the ideal source spectrum. Because of symmetry it is sufficient to use either the negative or the positive half of the total  $N$  Fourier components.

$$center = \frac{\sum_{j=1}^{N/2} A_a(\rho_j) \cdot \rho_j}{\sum_{j=1}^{N/2} A_a(\rho_j)} \quad (4.12)$$

$$width = 2\sqrt{\pi \ln 2} \frac{\sum_{j=1}^{N/2} A_a(\rho_j) \cdot |\rho_j - center|}{\sum_{j=1}^{N/2} A_a(\rho_j)} \quad (4.13)$$

$$G(\rho_j) = \exp \left[ \frac{-4 \ln 2 (k - center)^2}{width^2} \right] \quad (4.14)$$

#### Spectral amplitude correction

In the next step, the spectral correction curve  $S_c(j)$  is calculated that transforms the measured spectrum  $A_a(\rho_j)$  into the Gaussian fit by multiplication in the Fourier domain.

$$S_c(j) = \frac{G(\rho_j)}{A_a(\rho_j) + \epsilon} \quad (4.15)$$

A small positive value  $\epsilon$  is added to the spectral density in order to avoid a division by zero. This value is chosen small enough not to qualitatively change the reconstruction, on the order of 0.1% of the maximum value of  $G(\rho_j)$ . The so-obtained spectral correction curve can then be applied to the

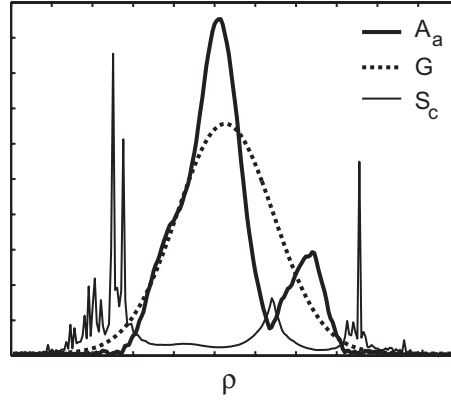


Figure 4.14: Illustration of spectral shaping.  $A_a$  corresponds to the original source spectrum,  $G$  to the fitted Gaussian spectrum and  $S_c$  to the spectral correction curve.

actual measurement in order to obtain the spectrally corrected Fourier components  $\tilde{M}_a(\rho_j)$  of the cross-correlation function  $m(z_i)$ .

$$\tilde{M}_a(\rho_j) = M_a(\rho_j) \cdot S_c(j) \quad (4.16)$$

#### Noise filtering

The Fourier components that lie outside the spectral density curve of the employed light source are noise contributions and their amplitude can easily be set to zero in the Fourier domain. This is equivalent to bandpass filtering.

#### Back transformation

The filtered and spectrally corrected amplitude values of the measurement signal in the Fourier domain,  $\tilde{M}_a(\rho_j)$ , is then again associated with its unchanged phase components  $M_p(\rho_j)$  and transformed by inverse Fourier transformation. The resulting function in the space domain,  $\tilde{m}(z_i)$ , is the spectrally corrected cross-correlation measurement.

$$\tilde{m}(z_i) = FT^{-1}[\tilde{M}_a(\rho_j) \cdot \exp(jM_p(\rho_j))] \quad (4.17)$$

#### 4.4.3 Phase correction and dispersion correction

The normally linear phases of the different Fourier components ( $A_p(\rho_j)$  or  $M_p(\rho_j)$ ) can be perturbed by a dispersion imbalance in the interferometer that can for example be due to different optics in the two interferometer arms and that results in a degradation of resolution. This is being used as an indicator for balancing high-resolution interferometers [12]. It has also been reported to be used for measuring the dispersion of samples introduced into perfectly balanced interferometers [13]. The numerical correction of this dispersion imbalance has been discussed in [2]. In the context of this section, the framework for such a numerical correction has already been laid and it shall therefore be briefly discussed. The dispersion correction can simply be realized by measuring the Fourier phases of the autocorrelation function and applying their complex conjugate to the Fourier components of the cross-correlation measurement.

$$\tilde{m}(z_i) = FT^{-1}[\tilde{M}_a(\rho_j) \cdot \exp(jM_p(\rho_j)) \cdot \exp(-jA_p(\rho_j))] \quad (4.18)$$

In this manner the phase terms introduced by the dispersion imbalance are annulled without affecting the phase terms that contain vital information about the sample. Upon back transformation the degradation in resolution due to dispersion is removed.

As an example, consider an autocorrelation measurement (mirror sample) in the white light interferometry discussed in the previous section. During experimentation it was found that the beam splitter cube used in this interferometer was slightly unsymmetrical. This created a dispersion imbalance and reduced the axial resolution. The interferometer was experimentally balanced by adding a 80  $\mu\text{m}$  microscope cover slide to one of the arms. The measurements with and without dispersion compensation could then be used to demonstrate the possibility of numerical dispersion compensation.

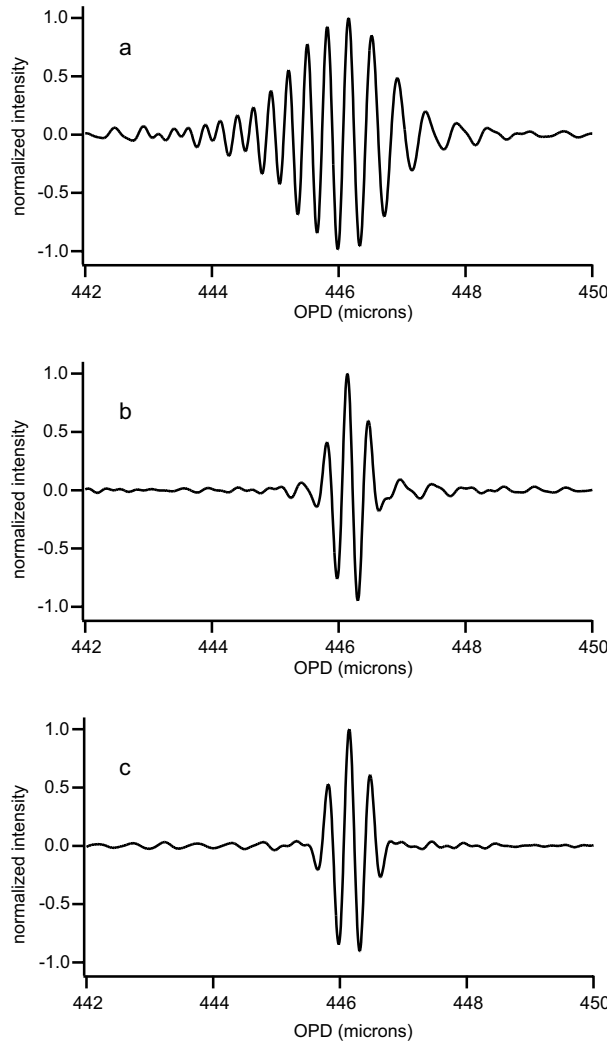


Figure 4.15: Autocorrelation with Xe arc lamp. All scans have been corrected by spectral shaping. (a) Interferometer with dispersion imbalance, chirp and resolution reduction is visible. (b) Interferometer is experimentally balanced, no chirp or reduction in resolution. (c) The measurement from a), but with spectral phase correction applied, numerical correction is comparable to experimental one in b).

The A scans in figure 4.15 are all corrected for the spectral shape of the white light source, according to the algorithm described in 4.4.2. Their spectral density amplitudes have been forced into a Gaussian shape. Figures 4.15a and b show the measurements for the unbalanced interferometer and the experimentally balanced case, respectively. The chirp and the degradation in resolution is clearly visible in a



and can be virtually eliminated by experimental means in b. The A scan in figure 4.15c was measured with the unbalanced interferometer and the spectral phase correction was applied in addition to the spectral amplitude correction. The result is hardly distinguishable from case b). The effect of dispersion is completely canceled with this numerical method.

## 4.5 Possible extensions of the self-referenced calibration method

### 4.5.1 Fiber-based implementation

The self-referenced calibration method could naturally also be realized using fiber-optic components in order to integrate it into the current, mostly fiber-based OCT systems. A straight-forward realization would consist of an additional fiber coupler in the detection arm of the interferometer, followed by a circulator and a fiber Bragg grating, as indicated in figure 4.16. Standard fiber Bragg gratings reflect light in a spectral window of less than 0.1 nm, which is well enough for the present purpose. The resulting two detection arms correspond to the main OCT signal and the calibration signal. They are acquired simultaneously and the calibration can be done *a posteriori* or in real-time on a PC.

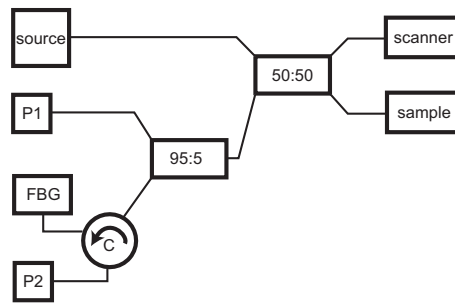


Figure 4.16: Possible fiber-optic realization of the self-referenced calibration method: C circulator, FBG fiber Bragg grating, P1 photodiode for detection of the main signal, P2 photodiode for detection of the calibration signal.

### 4.5.2 Optical amplification of calibration channel

Optical amplification of the calibration signal could be an interesting way for limiting the loss in signal to noise ratio of the measurement signal by permitting the deviation of less energy into the calibration channel. It would be sufficient to provide a low-energy seed radiation that is coherently amplified for easy detection, leaving the quasi-totality of the interference signal for principal signal detection. The amplification gain can be chosen as to further increase the coherence length of the calibration signal, allowing for longer calibrated depth scans. Two possible amplification schemes are proposed in figure 4.17, one for a free-space and one for a fiber-based implementation. Both are conventional single-pass amplifier types with counter-propagating pump beams that routinely supply gains of a factor of 1000.

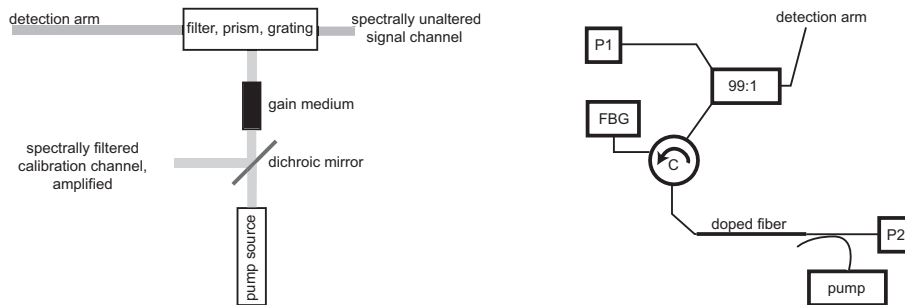


Figure 4.17: Single-pass amplification schemes for optical amplification of the calibration signal. (left) Free space realization, (right) fiber-based realization using a doped fiber as amplifier, C circulator, FBG fiber Bragg grating.

### 4.5.3 Real-time implementation

For a real-time implementation of the calibration method it seems necessary to develop a high speed signal processing circuit or program a digital signal processor (DSP) that is capable of rapidly extracting the OPD variation from the calibration signal and applying the necessary correction to the measurement signal. Expressed differently, the task at hand is to sample the measurement signal  $s$  at equal OPD intervals, based on the previously measured calibration signal  $c$ . This could be realized in the following manner, see figure 4.18.

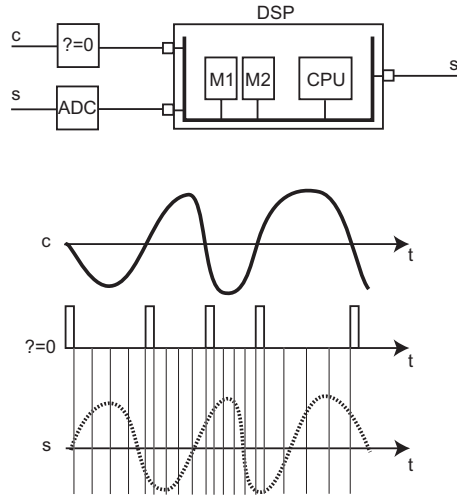


Figure 4.18: Schematic for a possible real-time implementation of the calibration method based on an analog-to-digital converter (ADC), a comparator ( $?=0$ ) and digital signal processor (DSP). M1 and M2 are internal buffer memories and CPU the central processing unit of the DSP.  $s$  and  $c$  are the analog signal and calibration channels, respectively and  $s'$  the correctly sampled signal values.

To a first approximation it seems sufficient to extract from  $c$  only the zero-crossings that correspond to OPD marks of a known spacing of a quarter of a calibration wavelength. This can easily be done by an analog zero comparator that delivers TTL pulses whenever the signal  $c$  crosses the zero line. Those zero marks are then used as a trigger input for a DSP. As a second input to the DSP there is of course the measurement signal  $s$  that is previously digitized at a high sampling frequency  $f \approx 40 \cdot \nu_{Doppler}$ , where  $\nu_{Doppler}$  corresponds to the Doppler frequency of the OCT signal. The DSP then realizes the following tasks:

- Using the zero crossing of  $c$  as start and stop triggers, it stores the highly sampled signal values of  $s$  into one of two buffer memories, alternating between the two from trigger to trigger. Thus there will always be one full memory that can be worked on, while the second one is being filled with the next values. Note that the number of values in each buffer is not constant due to the varying duration between triggers.
- Among the stored values in a buffer we want to pick a pre-determined number  $N$  (of the order of 3-6) of regularly spaced values that sufficiently sample the signal. Their spacing will depend on the total number of values in the buffer and has to be calculated by the DSP.
- The selected values represent the output of the DSP. They leave the device and the memory they previously occupied is overwritten with the next values. These values are to a first approximation regularly sampled with respect to OPD. The sampling precision increases with  $f/N$ .

With current standard DSPs that realize routinely 100 MFlops and high speed ADCs of 10 Msamples/s, it seems reasonably possible to realize this real-time correction for signal Doppler frequencies of up to 250 kHz.

## 4.6 Conclusion

The problems of precision and stability caused by non-linear and randomly varying depth scanning mechanisms have been highlighted and a new, self-referenced calibration technique has been introduced for their correction. The feasibility of the approach has been demonstrated. Its usefulness has been shown by combining it with a recently published spectral shaping technique for sidelobe suppression in OCT when using non-Gaussian source spectra. In order to be beneficial, such a technique requires highly repetitive measurements that can only be obtained with particularly stable scanning devices or well calibrated ones.

The principal limitation of the self-referenced calibration technique is a reduction in the measurement's signal-to-noise ratio due to the signal power lost to the calibration. Furthermore, in its current post-processing implementation, the method can not be used for real-time applications. Possible improvements are suggested that address both shortcomings. An optical amplification scheme of the quasi-monochromatic calibration beam is proposed in order to minimize the power loss and a fast implementation using digital signal processors can be envisioned that allows for real-time calibration.

## 4.7 References

- [1] K. M. Yung, S. L. Lee, and J. M. Schmitt. Phase-domain processing of optical coherence tomography images. *Journal of Biomedical Optics*, 4(1):125–136, 1999.
- [2] J. F. de Boer, C. E. Saxer, and J. S. Nelson. Stable carrier generation and phase-resolved digital data processing in optical coherence tomography. *Applied Optics*, 40(31):5787–5790, 2001.
- [3] G. F. Lindgren, R. P. Salathé, and R. Waelti. Measuring optical reflection profile of transparent or diffuse objects. *Patent WO9922198-A1*, 1999.
- [4] C. B. Su. Achieving variation of the optical path length by a few millimeters at millisecond rates for imaging of turbid media and optical interferometry: a new technique. *Optics Letters*, 22(10):665–667, 1997.
- [5] J. Szydlo, N. Delachenal, R. Gianotti, R. Walti, H. Bleuler, and R. P. Salathé. Air-turbine driven optical low-coherence reflectometry at 28.6-kHz scan repetition rate. *Optics Communications*, 154(1-3):1–4, 1998.
- [6] A. V. Zvyagin, E. D. J. Smith, and D. D. Sampson. Delay and dispersion characteristics of a frequency-domain optical delay line for scanning interferometry. *Journal of the Optical Society of America A-Optics Image Science and Vision*, 20(2):333–341, 2003.
- [7] G. J. Tearney, B. E. Bouma, and J. G. Fujimoto. High-speed phase- and group-delay scanning with a grating-based phase control delay line. *Optics Letters*, 22(23):1811–1813, 1997.
- [8] M. Kobayashi, H. F. Taylor, K. Takada, and J. Noda. Optical fiber component characterization by high-intensity and high-spatial-resolution interferometric optical-time-domain reflectometer. *IEEE Photonics Technology Letters*, 3(6):564–566, 1991.
- [9] J. Schmit and A. Olszak. High-precision shape measurement by white-light interferometry with real-time scanner error correction. *Applied Optics*, 41(28):5943–5950, 2002.
- [10] R. Tripathi, N. Nassif, J. S. Nelson, B. H. Park, and J. F. de Boer. Spectral shaping for non-Gaussian source spectra in optical coherence tomography. *Optics Letters*, 27(6):406–8, 2002.
- [11] L. Mandel and E. Wolf. *Optical Coherence and Quantum Optics*. Cambridge U. Press, Cambridge, 1995.
- [12] W. Drexler, U. Morgner, F. X. Kartner, C. Pitris, S. A. Boppart, X. D. Li, E. P. Ippen, and J. G. Fujimoto. *In vivo* ultrahigh-resolution optical coherence tomography. *Optics Letters*, 24:1221–3, 1999.
- [13] T. Hellmuth and M. Welle. Simultaneous measurement of dispersion, spectrum, and distance with a fourier transform spectrometer. *Journal of Biomedical Optics*, 3(1):7–11, 1998.

# Conclusion

The development of a customized CMOS detector array for OCT has initially been motivated by the goal of fast, parallel image acquisition. The feasibility of the approach had only been shown for the topographic measurement of reflective surfaces. The starting point of this thesis has been to apply the concept to scattering media and to identify other possible applications of this technology in the field of OCT. The first objective has been realized by demonstrating parallel OCT with the Smart Pixel Detector Array (SPDA) on reflective surfaces behind scattering solutions and of onion samples. Furthermore, the parallel imaging capability has allowed for fast three-dimensional OCT imaging of the thermal deformations of a human hair under laser irradiation at 25 volume acquisitions per second. Responding to the second objective, a new application has been developed for this detector technology in the form of the wavelength de-multiplexing concept for fast spectroscopic OCT. Its feasibility has been demonstrated experimentally and it is shown that this approach is inherently faster than the conventionally used numerical methods without suffering from other fundamental performance penalties. It has the additional advantage of being insensitive to false wavelength associations due to wrong Doppler frequency interpretation in the case of scan non-linearities or sample movements.

However, both the parallel detection scheme and the wavelength de-multiplexing approach are limited by the current SPDA design. For the time being, neither one can be competitive with the conventional point-scanning methods due to the low sensitivity achievable with the available detector array. Even with the high power delivered by a mode-locked Ti:Sa laser, the measured sensitivity did not exceed 76dB, well short of the required 90-100dB needed for clinical imaging in scattering tissues. Video-rate volumetric imaging has been demonstrated, but only on  $58 \times 58 \times 58$  voxel elements. The current number of parallel detectors and the maximum read-out rate of 5 Msamples/s limits the method to such a low number. In addition, the current detector suffers from sample dependant working parameters, stability problems and difficult and frequent re-calibration.

The device used in this thesis has been the first dedicated two-dimensional CMOS detector built for parallel OCT. The initial promising results have encouraged the development of improved designs for this application. In the meantime, a next generation device has been built, based on a novel circuit approach and a different sensor architecture. This detector array is currently being characterized by its designers. It is announced to be more stable in its working conditions and more power-efficient, permitting a faster read-out and the integration of a larger number of pixels. Furthermore, the new device has been designed to measure the signal's offset level and its temporal phase, allowing for phase-sensitive measurements.

In addition to the work realized with the SPDA, an idea unrelated to the detector array has been investigated, leading to an innovative calibration technique for optical path difference variations in low coherence interferometry. The problem addressed here has been the precise measurement of scan non-linearities and random variations due to mechanical limitations of scanning devices, allowing for their *a posteriori* correction. The proposed calibration concept has the advantage of being self-referenced, not requiring a secondary high coherence light source. The approach has been verified experimentally and its principal limitations, a loss in signal-to-noise ratio and the need for post-processing, have been discussed. Improvements and fiber-based implementations of the method have been suggested. This

depth scan calibration approach makes the use of low-cost scanning devices possible, even for high precision applications.

The scientific results obtained during this thesis encourage the further investigation of the presented experimental concepts in order to realize their proven potential for improving OCT imaging. As we all know, research is a never-ending story and the current results are but a starting point for future work.



# Curriculum Vitae

born May 7, 1974 in Neustadt an der Weinstrasse (Germany), German nationality, single

## Education

2000-2004	Ph.D.-thesis at the Swiss Federal Institute of Technology, Lausanne
1994-2000	University studies in physics: Physik-Diplom, Diplôme d'ingénieur, DEA 3 years in France (INP Grenoble) 5 semesters in Germany (Mainz, Karlsruhe) 1 semester in Spain (Zaragoza) 3 months in USA (Madison)
1993-1994	Military service
1993	German Abitur

## Professional experience

4/00-3/04	Ph.D. thesis (Lausanne) Innovative experimental concepts for Optical Coherence Tomography
4/99-3/00	Diploma work (Grenoble) Development of a laser master oscillator for polychromatic laser guide star generation
6/98-9/98	Internship (Madison) Self-assembly of nanostructures studied by STM, Band structure measurements of permalloy using synchrotron radiation
9/96-4/97	Erasmus exchange (Zaragoza) Heat capacity measurements of rare earth compounds

## Language skills

German	fluent (mother tongue)
French	fluent (7 years in French-speaking countries)
English	fluent (1 year US high school, TOEFL 677/680)
Spanish	advanced (DELE básico, 1 semester in Spain)
Bulgarian	intermediate
Chinese	elementary

## **Publications**

### **Peer-reviewed journals**

Laubscher, M., Bourquin, S., Froehly, L., Karamata, B. and Lasser, T., Spectroscopic optical coherence tomography based on wavelength de-multiplexing and smart pixel array detection, accepted for publication in Optics Communications, 2004.

Karamata, B., Lamblet, P., Laubscher, M. and Lasser, T., Spatially incoherent illumination as a mechanism for cross-talk suppression in wide-field optical coherence tomography, Optics Letters 29: p.736-738, 2004.

Laubscher, M., Froehly, L., Karamata, B., Salathé, R.P., and Lasser, T., Self-referenced method for optical path difference calibration in low-coherence interferometry. Optics Letters 28(24): p. 2476-2478, 2003.

Laubscher, M., Ducros, M., Karamata, B., Lasser, T., and Salathé, R.P., Video-rate three-dimensional optical coherence tomography. Optics Express 10(9): p. 429-435, 2002.

Ducros, M., Laubscher, M., Karamata, B., Bourquin, S., Lasser, T., and Salathe, R.P., Parallel optical coherence tomography in scattering samples using a two-dimensional smart-pixel detector array. Optics Communications 202(1-3): p. 29-35, 2002.

Laubscher, M., Segonds, P., and Pique, J.P., High resolution cw laser beam preamplified in a multipass cavity pumped by a CuHBr (HyBrID) laser. Optics Communications 184(5-6): p. 425-435, 2000.

Petrovykh, D.Y., Altmann, K.N., Hochst, H., Laubscher, M., Maat, S., Mankey, G.J., and Himpsel, F.J., Spin-dependent band structure, Fermi surface, and carrier lifetime of permalloy. Applied Physics Letters 73(23): p. 3459-3461, 1998.

### **Conference proceedings**

Karamata, B., Laubscher, M., Lamblet, P., Anhut, T. and Lasser, T., Sources for optical cross-talk suppression in wide-field optical coherence tomography, SPIE vol. 5316, 2004.

Laubscher, M., Ducros, M., Karamata, B., and Lasser, T., Video-rate high-resolution parallel optical coherence tomography. Coherence Domain Optical Methods in Biomedical Science and Clinical Applications VI 3(11): p. 107-110, 2002.

Laubscher, M., Ducros, M., Karamata, B., Bourquin, S., and Lasser, T., High resolution parallel optical coherence tomography in scattering samples. Photon Migration, Optical Coherence Tomography, and Microscopy 2(31): p. 335-340, 2001.

Schock, M., Foy, R., Pique, J.P., Chevrou, P., Ageorges, N., Petit, A., Bellanger, V., Fews, H., Foy, F.C., Hogemann, C., Laubscher, M., Peillet, O., Segonds, P., Tallon, M., and Weulersse, J.M., PASS-2: Quantitative photometric measurements of the polychromatic laser guide star. Adaptive Optical Systems

Technology, Pts 1 and 2, 4007: p. 296-307, 2000.

Schock, M., Pique, J.P., Petit, A., Chevrou, P., Michau, V., Grynberg, G., Migus, A., Ageorges, N., Bellanger, V., Biraben, F., Deron, R., Fewes, H., Foy, F., Hogemann, C., Laubscher, M., Muller, D., d'Orgeville, C., Peillet, O., Redfern, M., Foy, R., Segonds, P., Soden, R., Tallon, M., Thiebaut, E., Tokovinin, A., Vaillant, J., and Weulersse, J.M., ELP-OA: Measuring the wave front tilt without a natural guide star. *Propagation and Imaging through the Atmosphere Iv*, 4125: p. 41-52, 2000.

Foy, R., Pique, J.P., Petit, A., Chevrou, P., Michau, V., Grynberg, G., Migus, A., Ageorges, N., Bellanger, V., Biraben, F., Deron, R., Fewes, H., Foy, F., Hogemann, C., Laubscher, M., Muller, D., d'Orgeville, C., Peillet, O., Redfern, M., Schock, M., Segonds, P., Soden, R., Tallon, M., Thiebaut, E., Tokovinin, A., Vaillant, J., and Weulersse, J.M., ELPOA: Toward the tilt measurement from a polychromatic laser guide star. *Adaptive Optical Systems Technology, Pts 1 and 2*, 4007: p. 284-295, 2000.

Foy, R., Pique, J.P., Petit, A., Chevrou, P., Michau, V., Grynberg, G., Migus, A., Ageorges, N., Bellanger, V., Biraben, F., Deron, R., Fewes, H., Foy, F., Hogemann, C., Laubscher, M., Muller, D., d'Orgeville, C., Peillet, O., Redfern, M., Schock, M., Segonds, P., Soden, R., Tallon, M., Thiebaut, E., Tokovinin, A., Vaillant, J., and Weulersse, J.M., Polychromatic guide star: Feasibility study. *High-Power Laser Ablation Iii*, 4065: p. 312-323, 2000.

Schock, M., Foy, R., Pique, J.P., Tallon, M., Segonds, P., Laubscher, M., and Peillet, O., PASS-2: Photometry of the polychromatic laser guide star. *Adaptive Optics Systems and Technology*, 3762: p. 321-329, 1999.